University of Zurich[UZH]

Glacier dynamics: influence of precursor crevasses and supraglacial lakes on calving at Sermeq Kujalleq in Kangia (Jakobshavn Isbræ), Greenland

GEO 511 Master's Thesis

Author
Doriano Hautle
10-726-834

Supervised by
Dr. Andrea Kneib-Walter
Dr. Martin Lüthi

Faculty representative
Prof. Dr. Andreas Vieli

30.01.2024
Department of Geography, University of Zurich

Abstract

Tidewater outlet glaciers, crucial in draining the Greenland Ice Sheet (GrIS), significantly contribute to global sea-level rise. However, the primary mechanism of their mass loss, calving, remains insufficiently understood. This study delves into the influence of crevasses and supraglacial lakes on the calving dynamics of the Sermeq Kujalleq in Kangia (Jakobshavn Isbræ), one of the fastest-flowing and most studied glaciers in the world. Utilizing optical remote sensing data from 2016 to 2022, 29 calving events are analyzed, of which 23 feature sections that coincide with pre-existing crevasses. These precursor crevasses predominantly appear in the southern and central sections of the glacier terminus, where there is a rise in glacier bed elevation, which is thought to contribute to the formation of deep crevasses. Conversely, supraglacial lakes are distributed across the glacier and their fill-and-drain cycles are irregular. Using a semi-automatic lake area detection algorithm to analyze 12 supraglacial lakes, 63 drainage events are identified, with 22 completing within four days or less. In 13 of these events, the drained lake area is 80% or more. Drainage events often occur in clusters and are believed to accelerate ice flow via basal lubrication, potentially influencing or triggering calving events. These lakes typically reach their maximum size before the end of summer, suggesting that the subglacial drainage system becomes efficient enough to handle surface meltwater, which reaches the bedrock through englacial routes like moulins. Additionally, this research identifies three instances where increases in glacier velocity coincide with calving events, and seven instances where the drainage of supraglacial lakes is followed by large calving events.

This study accentuates the connection between precursor crevasses and calving events, and underscores the relationship between supraglacial lake drainage and the ensuing acceleration of glacier movement, which is likely to promote further calving. These findings offer valuable insights for improving our knowledge about calving dynamics and informing glacier calving models, enhancing our ability to predict future sea-level rise in a changing climate. Incorporating higher-resolution imagery in future studies could enable more accurate tracking of crevasses and calculations of lake areas, including assessments of depth. This enhanced precision may reveal new correlations between crevasse formation, lake drainage patterns, and calving events, further improving our understanding of tidewater glacier dynamics.

Table of Contents

List of Figures

List of Tables

List of Abbreviations

a.m.s.l.	above mean sea level
DEM	Digital Elevation Model
DLR	German Aerospace Center
ESA	European Space Agency
EW	Extra Wide
GC-Net	Greenland Climate Network
GDEM	Global Digital Elevation Model
GEE	Google Earth Engine
GIS	Geographic Information System
GPS	Global Positioning System
GRD	Ground Range Detected
IW	Interferometric Wide
LiDAR	Light Detection and Ranging
MSI	MultiSpectral Instrument
NDWI	Normalized Difference Water Index
NIR	Near-Infrared
NSIDC	National Snow and Ice Data Center
PDD	Positive Degree Days
RMSE	Root Mean Square Error
SAR	Synthetic Aperture Radar
SCL	Scene Classification
SKK	Sermeq Kujalleq in Kangia
SMA	Simple Moving Average
SM	Stripmap
TOA	Top of Atmosphere
TLS	Terrestrial Laser Scanner
UAV	Unmanned Aerial Vehicle
WV	Wave

1 Introduction

1.1 Outlet Glaciers in Greenland

Outlet glaciers, key components of the Greenland Ice Sheet (GrIS), have been the subject of intensified study in glaciology, largely due to their substantial impact on global sea-level rise and climate dynamics (Straneo & Heimbach 2013). Over the last three decades, these glaciers have been undergoing an accelerated rate of ice loss, raising significant concerns about their future stability and the consequent global implications (Rignot et al. 2011; Shepherd et al. 2012). Outlet glaciers are important because they act as conduits for ice to move from the interior of ice sheets to the ocean. In Greenland, the ice sheet lies on a characteristic topography, which features a concave central part surrounded by higher elevations, as seen in Fig. 1a (Morlighem et al. 2017). The edges of the ice sheet feed into outlet glaciers, which are essentially channels or streams of ice that flow from the higher, central areas of the ice sheet toward the coast, often terminating in the ocean (Thomas et al. 2011).

When a glacier flows directly into the sea, ending in a cliff-like ice front where icebergs calve off, it is called a tidewater glacier (Meier 2024). These glaciers are influenced by both internal glacial dynamics and interactions with ocean water, making their behavior complex and important in understanding glacier-ocean interactions and their impact on sea level rise. Tidewater outlet glaciers in Greenland play a crucial role in global sea-level rise, mainly due to their contribution to mass loss from the GrIS (Lampkin et al. 2018). This loss is primarily driven by two factors: the runoff of surface meltwater and the calving of icebergs. Yang & Smith (2013) estimated that about 40% of the GrIS's mass loss can be attributed to the surface meltwater runoff, underscoring the significant impact of melting. The remaining majority of mass loss is attributed to iceberg calving, which is especially prominent in tidewater outlet glaciers. This process, which is integral to the behavior of tidewater glaciers, is governed by an intricate interplay of factors, making it a pivotal yet enigmatic aspect of glaciology (Benn et al. 2017). These include the glacier's inherent structural properties, variations in water temperature, and the dynamics of ice-ocean interactions. The complexity of these factors, coupled with their interdependencies, renders the prediction of calving events a challenge. Calving is not merely a mechanical process but also involves thermal dynamics within the glacier's system (Benn, Warren & Mottram 2007; Amundson et al. 2010).

The role of the fjord in which a tidewater glacier terminates and the presence of ice mélange – a mixture of sea ice and calved icebergs – at the glacier front are crucial. The ice mélange acts as a mechanical buffer against calving, but its presence and thickness are subject to seasonal variations and environmental conditions, adding another layer of complexity to the calving process (Amundson et al. 2010). The fjord's topography and depth influence the manner and extent to which warm ocean waters interact with the glacier's terminus. This interaction can affect the rate of underwater melting and, consequently, the stability of the glacier front (Benn et al. 2007). These elements – the glacier's structural integrity, the water properties within the fjord, and the dynamic nature of the ice mélange – collectively contribute to the complexity of calving phenomena in tidewater glaciers.

Moreover, the surface water draining system of the GrIS is notably complex, encompassing streams, lakes, crevasses, fractures, and moulins (Yang & Smith 2013). These surface features are not only indicative of melting but also play a role in the dynamics of the ice sheet. The majority of studies have focused on supraglacial lakes, largely due to the limitations of publicly available satellite data, which often cannot adequately resolve narrower features such as streams and crevasses (Studinger et al. 2022; Yang & Smith 2013). However, small surface features can play key roles in the development of the hydrological system of a glacier, influencing its dynamics (Yang & Smith 2013). Understanding the future behavior of outlet glaciers in Greenland requires an in-depth comprehension of the ice-dynamic responses to these hydrological processes (Moussavi et al. 2016). The importance of tidewater outlet glaciers is underscored by their role as indicators of climate change. Their responses to atmospheric and oceanic variations offer vital insights into the broader environmental health of subpolar regions (Straneo & Heimbach 2013). The calving rates and ice flow velocities of these glaciers are responsive to both oceanic warming and atmospheric temperature shifts, rendering them

crucial for understanding climate dynamics (Moon et al. 2012). Understanding the nuances of the calving processes is crucial for predicting the future impacts of climate change, especially in terms of sea-level rise and its implications for coastal communities and ecosystems (Nick et al. 2009; Straneo & Heimbach 2013).
To enhance our understanding of how calving rates and ice flow velocities in glaciers respond to environmental changes, a focused study on specific glacial features is required. One such feature is the crevasse, frequently found on tidewater outlet glaciers, which plays a significant role in the calving process. Crevasses are fractures within the glacier's ice, acting as lines of weakness along which icebergs may separate (Colgan et al. 2016). Concurrently, the flow velocity of the glacier, another key factor in calving dynamics, is influenced by the presence and drainage of supraglacial lakes. These lakes can modify the glacier's dynamics, potentially leading to an acceleration of ice flow (Stevens et al. 2022). However, the precise impact of these lakes on the calving process has not yet been studied. Therefore, a cautious and thorough analysis of these features is not only beneficial but necessary for a deeper, more detailed understanding of glacier behavior, particularly in predicting changes in mass and the subsequent implications for sea-level rise and global climate.

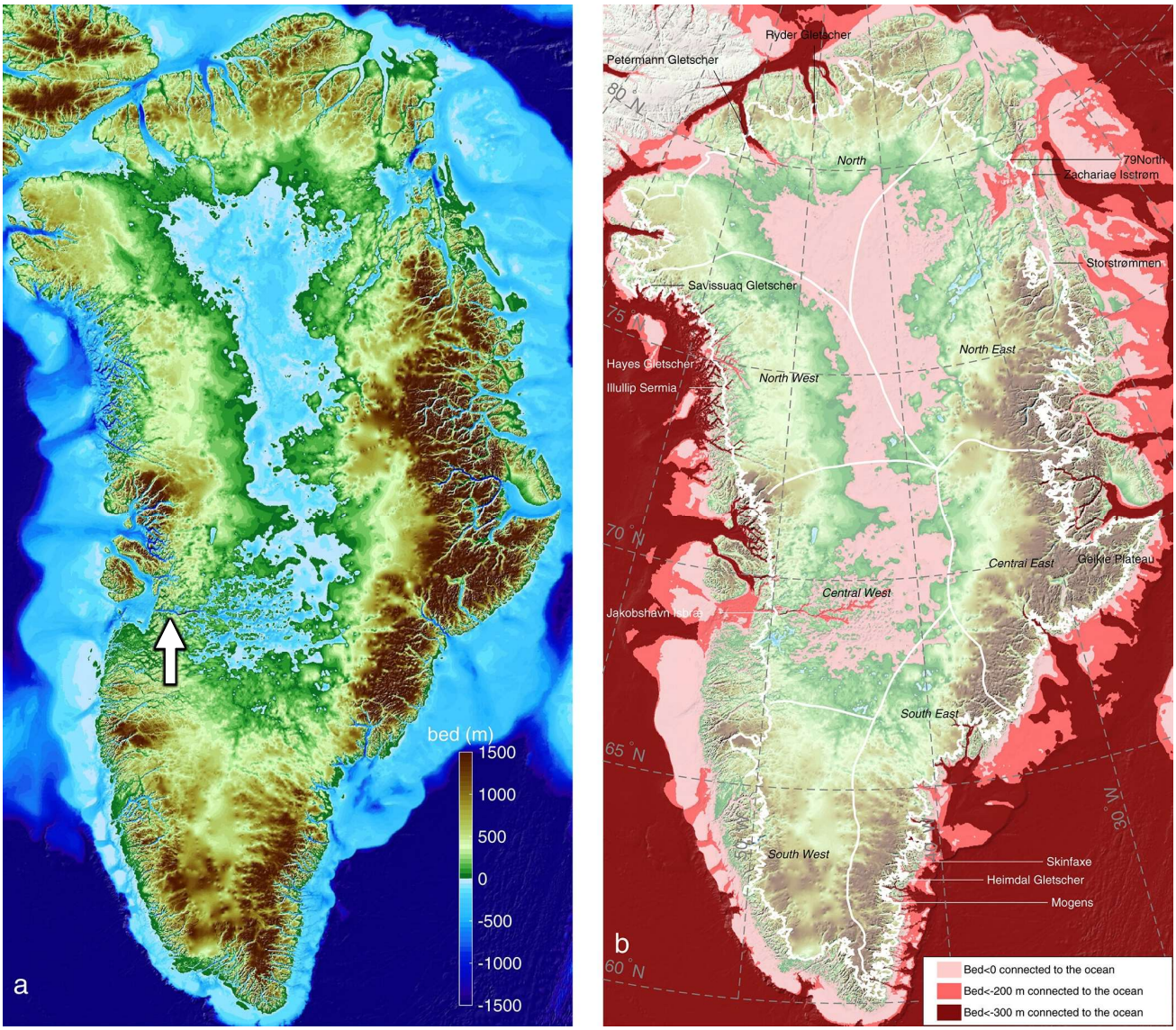

Fig. 1: (a) Bed topography of Greenland (BedMachine v3) with elevation with respect to mean sea level. The central part of the island is characterized by low elevations of the bedrock, surrounded by coastal mountains. The white arrow shows the location of the Sermeq Kujalleq in Kangia (SKK, Jakobshavn Isbrae). (b) Regions below sea level that are connected to the ocean, as well as the 2017 ice extent (thin white line) (Morlighem et al. 2017).

1.2 Crevasses

Crevasses are longitudinal features that form on glaciers due to variations in ice velocity and the resultant stresses that crack the ice. These features, which range from a few meters to tens of meters in width, can extend for several hundred meters in length and reach depths of about 50 meters (Colgan et al. 2016). They pose significant hazards to mountaineers, skiers, and researchers, particularly when concealed by snow. The orientation of crevasses is closely related to the surface strain rate of the glacier, providing valuable insights into its ice dynamics. Different types of crevasses form in response to varying strain rates in the ice. For instance, splaying crevasses typically develop in areas of compressional flow, often found where the glacier bed is concave or narrowing. In contrast, transverse crevasses are indicative of extensional flow, which can occur in convex bed profiles or where the glacier is widening. A schematic overview of these different crevasse types is depicted in Fig. 2, and a real crevasse on the Sermeq Kujalleq in Kangia (SKK) is shown in Fig. 3. Colder ice, being more brittle, responds to a given strain rate with more pronounced crevasse formation. Additionally, the orientation of crevasses undergoes cyclic annual variations. During summer, when ice velocity typically increases, shear stresses exerted on transverse crevasses can cause them to gradually turn in a more longitudinal direction (Bhardwaj et al. 2016).

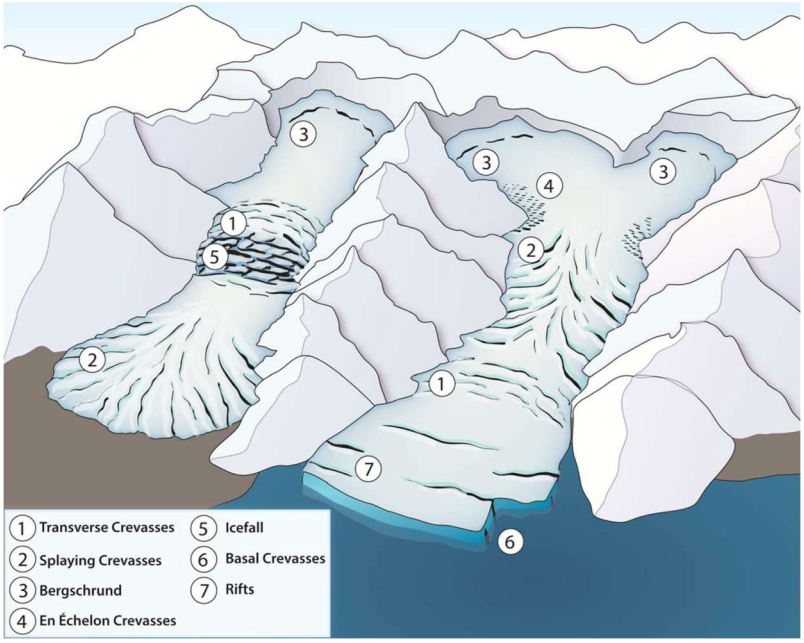

Fig. 2: Schematic of various types of crevasses on a land-terminating glacier (left) and on a tidewater glacier (right) (Colgan et al. 2016).

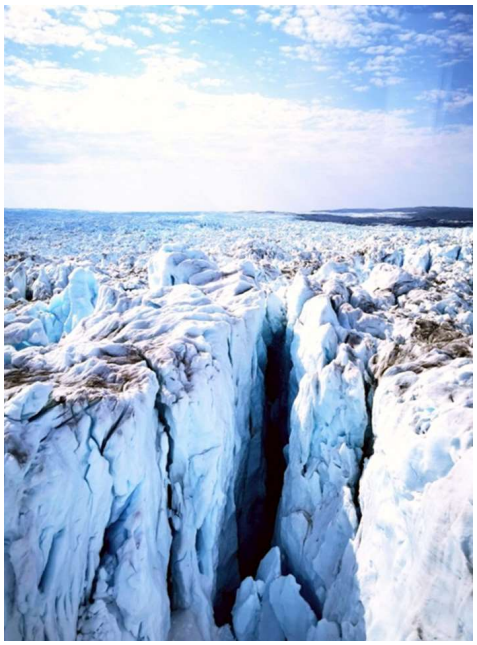

Fig. 3: A crevasse on the Sermeq Kujalleq in Kangia in Western Greenland (Photo: Ana Nap).

In their research on the dynamics of calving glaciers, Benn et al. (2007) identify the significant role of crevasses in calving processes. They find that the primary determinant of calving events is the strain rate, which arises from spatial variations in glacier velocity and influences both the depth and location of crevasses. These crevasses are crucial in initiating and advancing calving events. The study underscores that certain pre-existing crevasses, particularly those aligned with areas of heightened stress, are more likely to lead to calving. Similarly, Colgan et al. (2016) suggest that glacier crevasses are a fundamental control mechanism for calving, as they establish the necessary conditions for icebergs to detach from the glacier terminus. Investigating and mapping these crevasses and their relationship to calving events can offer valuable insights. However, the research does not provide specific methodologies to predict calving events based on these observations.

Crevasses also play a pivotal role in supraglacial lake dynamics by serving as channels for meltwater. This interaction significantly affects glacier behavior, as the increased drainage from these lakes leads to enhanced ice deformation. During summer, meltwater fills these crevasses, resulting in hydrofracture and ice deformation, promoting calving. In contrast, the drainage of water from crevasses during winter stabilizes the ice and tends to reduce calving events. This seasonal dynamic underscores the critical role of crevasses in influencing the impact of supraglacial lakes on glacier behavior (Chudley et al. 2021; Colgan et al. 2016).

1.3 Supraglacial Lakes

During the summer months, the increase in solar shortwave radiation and precipitation leads to the melting of firn and ice, initiating surface runoff and the formation of supraglacial streams. These streams converge in topographic depressions on the glacier's surface, giving rise to supraglacial lakes that become the primary units of surface water storage (Jiang et al. 2022; Lampkin et al. 2020). Fig. 4 shows a schematic representation of the basic hydrological system of a glacier, including supraglacial meltwater and lakes, the englacial connection (moulin), and the subglacial water flow. Fig. 5 is an aerial photograph of a supraglacial lake in Western Greenland. Supraglacial lakes are not limited to any specific area of a glacier but can develop wherever conditions are favorable. This includes areas along the central flow line, where the ice movement is often faster and the ice tends to be thicker, as well as along the margins or edges of the glacier, characterized by slower ice movement. The formation of these lakes is largely influenced by the presence of topographic lows on the glacier's surface, which can be a result of the glacier's natural dynamics, the underlying topography, or melting processes. Understanding when, where, and how supraglacial lakes form is important for improving our knowledge of the glacier and its response to changing environmental conditions.

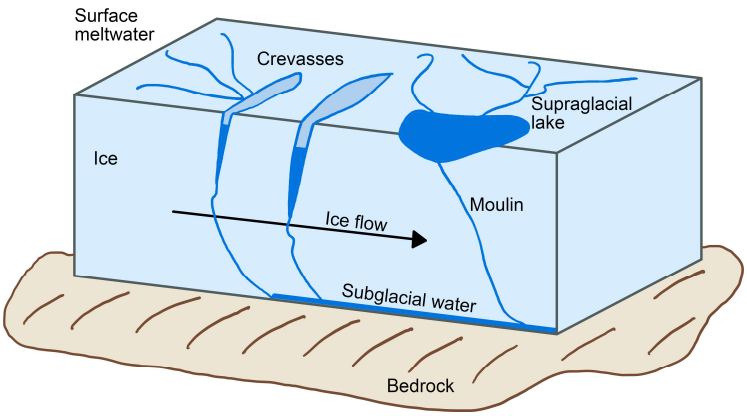

Fig. 4: Schematic representation of a part of a glacier, with meltwater flowing in streams on the ice surface, water-filled crevasses, a supraglacial lake, as well as the englacial connection (moulin), and the subglacial water flow at the glacier bed.

Fig. 5: Aerial image of a supraglacial lake in western Greenland (Photo: Laura A. Stevens).

During the melt season, supraglacial lakes significantly influence glacier mass loss in two distinct ways. Firstly, their lower albedo compared to ice enhances heat absorption from the sun, storing energy in the form of (relatively) warm water (Lüthje et al. 2006). Secondly, the dynamics of these lakes, particularly their drainage, impact glacier dynamics. Lake drainage can occur slowly through overtopping, leading to the incision of streams on the glacier surface over days to weeks, or rapidly through hydrofracture within hours to days (Williamson et al. 2018). Rapid drainage through hydrofracture occurs when the accumulated water in the lake exerts enough pressure to crack open a crevasse beneath it (Stevens et al. 2015). This process deepens the crevasse as water continues to fill it. Conversely, slow drainage, or overtopping, takes place when a lake overflows its topographical low, with the excess water flowing over the glacier surface and carving streams into the ice. This water can potentially enlarge existing connections to the subglacial system, such as moulins, influencing the glacier's surface and subglacial hydrology (Miles et al. 2017).

The triggers for lake drainage events are not fully understood. It is speculated that nearby meltwater reaching the glacier bed alters the local ice dynamics (stress, velocity), potentially creating temporary fractures under the lake which are subsequently enlarged by hydrofracture, enabling rapid drainage (Hoffman et al. 2018; Joseph & Lampkin 2017; Poinar & Andrews 2020). Alternatively, lake expansion can reach a threshold where it encompasses existing moulins, leading to drainage (Hoffman et al. 2018). Furthermore, interactions between slowly and rapidly draining lakes are possible: for instance, overtopping water from one lake can reach the ice sheet bed, enhancing basal sliding and increasing the likelihood of rapid drainage in nearby lakes (Stevens et al. 2015; Tedesco et al. 2012). This interaction can trigger cascading lake drainage and hydrofracture events across several kilometers through newly formed moulins and supraglacial streams.

Hoffmann et al. (2018) suggest that the majority of lakes tend to drain in clusters within a single day, indicating that such cascading drainage might be a common phenomenon.

Lake drainage events play a crucial role in the dynamics of glaciers, particularly through their impact on the subglacial hydrological system. When lake water reaches the glacier bed, it increases water pressure and hence basal sliding, a process that is particularly significant in areas where sediment underlies the glacier (Doyle et al. 2018; Kulessa et al. 2017). This influx of water can cause local or regional acceleration of ice flow, leading to both short-term and long-term effects (Jiang et al. 2022; Lampkin et al. 2020; Liang et al. 2012). Long-term effects include the formation of moulins within lake basins or further afield (Hoffman et al. 2018), which then channel surface meltwater to the ice-sheet bed, increasing ice-sheet velocity over monthly and seasonal timescales (Koziol & Arnold 2018). Additionally, the fractures that are created during lake drainage facilitate the movement of surface meltwater to the cold ice underneath, potentially leading to increased ice deformation (Lüthi et al. 2015). Hoffmann et al. (2018) note that the long-term impact of lake drainage, through the formation of persistent moulins, is more consequential than the short-term speedup during the drainage itself.

The resistance at the base of a glacier is significantly influenced by the water pressure and distribution within the subglacial drainage system, which is, in turn, controlled by the input of surface meltwater to the bed (Cassotto et al. 2019; Chandler et al. 2021). While inland areas of the Greenland Ice Sheet (GrIS) are known to be sensitive to surface melt inputs on both hourly and seasonal scales, the dynamics of these processes in tidewater glaciers are less understood (Stevens et al. 2022). The binary classification of drainage systems into efficient or inefficient types, while applicable to inland glaciers, may not be as straightforward for tidewater glaciers, particularly in relation to their flow response to subglacial hydrological processes, which have only been measured for slow-flowing glaciers (Stevens et al. 2022).

The connection between the supraglacial hydrological system and the subglacial drainage system through englacial routes remains an area of active research. Most of the surface melt on the GrIS enters the ice sheet, with a significant portion channeled through supraglacial streams that terminate in moulins, leading directly to the bed (Hoffman et al. 2018; Koziol & Arnold 2018). Most moulins are formed when crevasses fill with water, causing hydrofracture in the cold ice and subsequently opening a channel (Hoffman et al. 2018). However, many moulins are also found away from crevasse fields due to the cold ice preventing the formation of an extensive englacial system. Lake drainages are a primary factor in forming most moulins and have lasting impacts on ice dynamics, sometimes for years, especially if there is a regular water supply. This influence eventually ceases when the moulin is advected away from the water source. Hoffmann et al. (2018) highlight that lake drainage is the primary control of the number and distribution of moulins. Interestingly, since moulins predominantly form due to lake drainage rather than ice stresses, they could also develop at higher altitudes, influencing areas of the glacier with lower ice velocities. As runoff and lake drainage events are expected to increase in magnitude and elevation range in the future, this will likely lead to the formation of more moulins at higher elevations (Hoffman et al. 2018).

Consequently, the influence of supraglacial lakes extends beyond their immediate vicinity, significantly impacting the broader dynamics of glaciers. By modulating the timing, location, rate, and volume of meltwater input to the glacier bed, these lakes markedly affect the flow velocity and, thereby, the calving rate of the glacier (Moussavi et al. 2016). This complex interplay of factors highlights the intricate nature of glacier systems and emphasizes the critical role of supraglacial lakes in understanding glacier behavior in the face of climate change.

1.4 Relevance and Objectives

The primary aim of this research is to enhance our understanding of mass loss through calving processes at outlet glaciers in Greenland. These glaciers, which drain the Greenland Ice Sheet (GrIS) at an unprecedented rate, play a pivotal role in the global climate system (Rignot et al. 2011). With the ongoing progression of climate change, their study becomes increasingly urgent. The accelerated glacier mass loss contributes significantly to rising sea levels, a matter of global concern. Calving, the process by which icebergs break off from glaciers, is a complex phenomenon and less understood compared to mass loss through melting. Existing models for predicting mass loss due to calving need refinement (Van Dongen et al. 2019). This study aims to

explore new methodologies to analyze calving events, focusing on the role of crevasses and supraglacial lakes. These features, commonly found on Greenland's outlet glaciers, are believed to significantly influence glacier dynamics, including calving processes. While pinpointing the exact triggers of calving events remains a challenging endeavor, gaining an understanding of the contributing factors is a crucial step.

The glacier chosen for detailed analysis in this thesis is Sermeq Kujalleq in Kangia (SKK, also known as Jakobshavn Isbræ). This glacier is not only one of the fastest-flowing glaciers in the world (Thomas et al. 2011) but also a key component of the GrIS, making it an ideal subject for in-depth study. The research presented here is part of the COEBELI project ("Comprehensive Observations of episodic Basal, Englacial and Lateral Influences on Ice Stream Dynamics"), a collaborative research effort of several institutions, among which the Department of Geography of the University of Zürich. COEBELI aims to investigate the short-term dynamics of the SKK glacier using a variety of high-resolution datasets. This study utilizes long-term satellite data to analyze two glacier features – crevasses and supraglacial lakes – on Sermeq Kujalleq. By examining these features over an extended period, the research seeks to improve our understanding of their evolution, interaction with glacier dynamics, and their potential role in calving processes. The ultimate goal is to contribute to the broader understanding of glacier behavior in response to climatic changes and to aid in the development of more accurate models for predicting future mass loss and its implications for sea-level rise. This work, therefore, aims not to be just a study of a singular glacier but a piece in the puzzle of understanding global climate dynamics and their impact on our planet.

The study sets out with specific objectives to thoroughly investigate crevasses and supraglacial lakes on the SKK glacier, with a focus on discerning which crevasses directly contribute to calving events, and understanding the intricate relationship between lake drainage and glacier dynamics, including how such drainage events are affected by environmental factors like temperature. This research aims to explore the potential connections between lake drainage events and calving events, potentially through an indirect pathway such as the acceleration of ice flow. The addressed key research questions are: (1) Which specific crevasses contribute to calving events on the SKK glacier, and what are the patterns of their formation in terms of timing and location? (2) What factors determine the formation of these crevasses in particular areas of the SKK glacier? (3) When and in which locations do supraglacial lakes develop on the SKK glacier? (4) How and when do supraglacial lakes on the SKK glacier undergo drainage, and what impact do these events have on the dynamics of the glacier? Jakobshavn Isbræ is one of the most studied glaciers, especially in the context of its rapid changes. By offering a comprehensive analysis, the findings from this work aim to contribute to or complement other studies, also on other glaciers.

1.5 Study Site

The Greenland Ice Sheet (GrIS), encompassing 80% of Greenland, is the Northern Hemisphere's largest ice mass and is globally second only to Antarctica. Stretching 2'220 kilometers north-south, with its widest point near the northern margin at 1'094 kilometers, it has an average ice thickness of 1'500 meters. Located approximately between a latitude of 60° N and 80° N, Greenland lies outside the polar zone, as seen in Fig. 6, which shows the island's position in the World. The ice mass has a total area of 1.8 million square kilometers and is contained by coastal mountains located around a central area of depression (see Fig. 1). The GrIS principally moves from the crest of the ice divide (see Fig. 7) towards the sea. Holding 12% of the world's glacier ice, its full melt would raise sea levels by approximately 7.4 meters. Since the 1990s, the GrIS has added 10.6 mm to global sea-level rise, a trend that continues upward (Raikar 2023).

The GrIS is drained by numerous outlet glaciers, located all around the edges of the island. Sermeq Kujalleq in Kangia (SKK), which is also known as Jakobshavn Isbræ, is a large tidewater outlet glacier located in Western Greenland near the town of Ilulissat. It is situated in a deep bedrock channel, extending over 50 kilometers in length and reaching depths of up to 1600 meters, boasting ice thicknesses exceeding 2000 meters (An et al. 2017; Gogineni et al. 2014). The significance of the SKK Glacier is underscored by its connection to and ability to drain a substantial portion of the GrIS' inland ice. Estimates of this area range from 3.7 to 6.5% of the inland ice, equivalent to about 63'000 to 110'000 square kilometers (Weidick & Bennike 2007).

Fig. 6: Location of Greenland (in red) in the World. Extending to a latitude of about 80°N, the Greenland Ice Sheet (GrIS) lies outside of the polar zone.

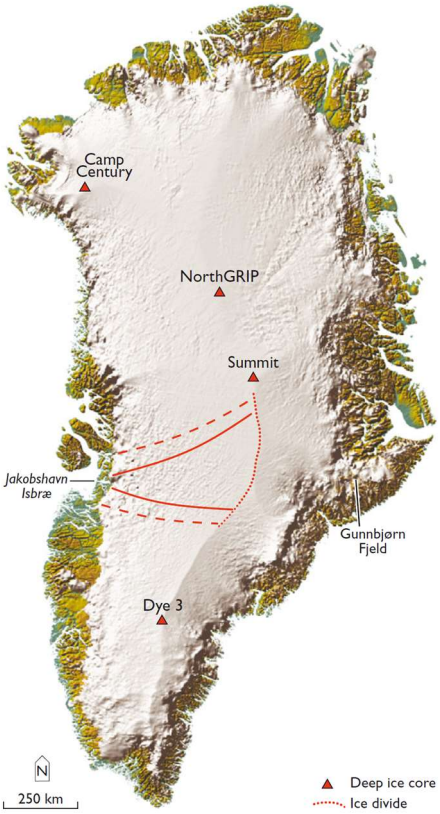

Fig. 7: Location of the SKK (Jakobshavn Isbræ) glacier and the ice divide in Greenland. The solid red line shows the approximate ice drainage area of the glacier, and the dotted red line the ice drainage area of the entire Disko Bugt region (Weidick & Bennike 2007).

Fig. 7 illustrates the ice drainage area of the SKK Glacier as well as the broader catchment area encompassing the entire Disko Bugt region, the bay where the glacier reaches the ocean. The glacier's calving front is located at the end of a 55 kilometers long fjord, as shown in Fig. 8. Fig. 9 illustrates the significant retreat of the SKK's calving front, which has retracted over 35 kilometers since 1850 (Steiger et al. 2018). Notably, between 2002 and 2003, the glacier underwent a dramatic change when its 15-kilometer-long floating tongue, previously wedged between the fjord walls and thinning at a rate of 80 meters per year, disintegrated (An et al. 2017; Joughin et al. 2010; Thomas et al. 2011). Due to the reduced back stress and the inflow of warm Atlantic waters, this event led to a rapid retreat of the glacier's front by several kilometers, marking a notable shift in its evolution (An et al. 2017). The retreat of the glacier is significantly influenced by the slope of the bed topography at the terminus. Areas with retrograde bed topography lead to rapid retreat due to marine-ice sheet instability (An et al. 2017). In these regions, the increased thickness of the ice allows for higher spreading rates. Conversely, protrusions or 'bumps' in the bed topography act as barriers, slowing down the retreat of the glacier's tongue. While the rate at which the glacier is retreating has slightly slowed down in the last decade, the ice flow velocity is increasing, reaching up to 45 meters per day at the calving front (Joughin et al. 2021), making SKK one of the fastest flowing glaciers in the world with a very active calving front (Thomas et al. 2011). Characterized by its high velocity, the SKK glacier is a prime site for observing dynamic ice processes such as calving. This fast ice movement results in a dense network of crevasses, particularly near the margins (Mayer & Herzfeld 2000), and a notable presence of frequently draining supraglacial lakes, both directly on the fast-moving ice stream and in surrounding areas (Liang et al. 2012). SKK's significant and rapid changes, coupled with its substantial contribution to sea-level rise, render it a critical location for glaciological research. The abundance of data available, extensive historical records, and the numerous studies conducted on SKK further enhance its value as a focal point for understanding glacier dynamics and environmental interactions.

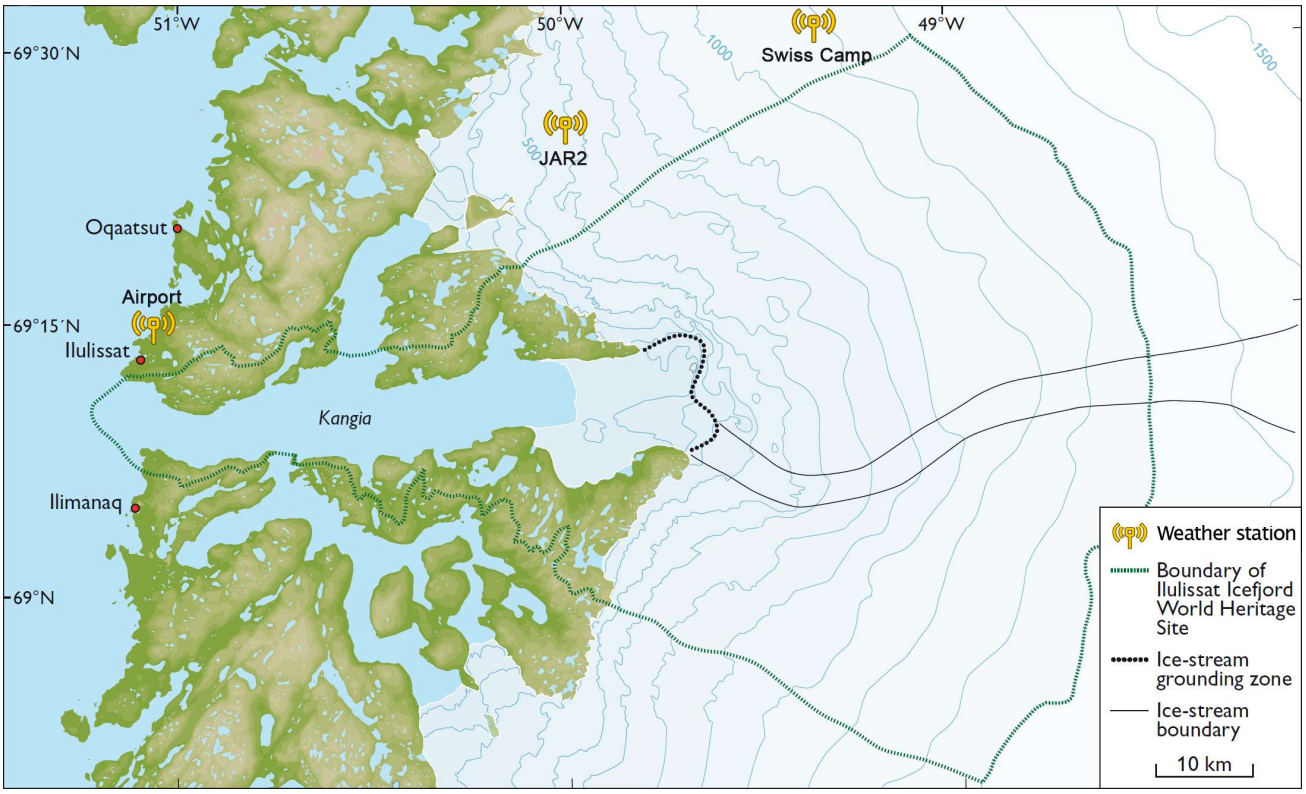

Fig. 8: Map of the area surrounding the lower end of the SKK glacier, as well as the Disko Bugt bay. The outline of the fast-moving ice is delineated by the solid black line. Nearby weather stations are marked with yellow antennas. The shown ice extent is based on data from 1994, and the grounding zone is from 1985. The map is a modified version based on the one found in Weidick & Bennike (2007).

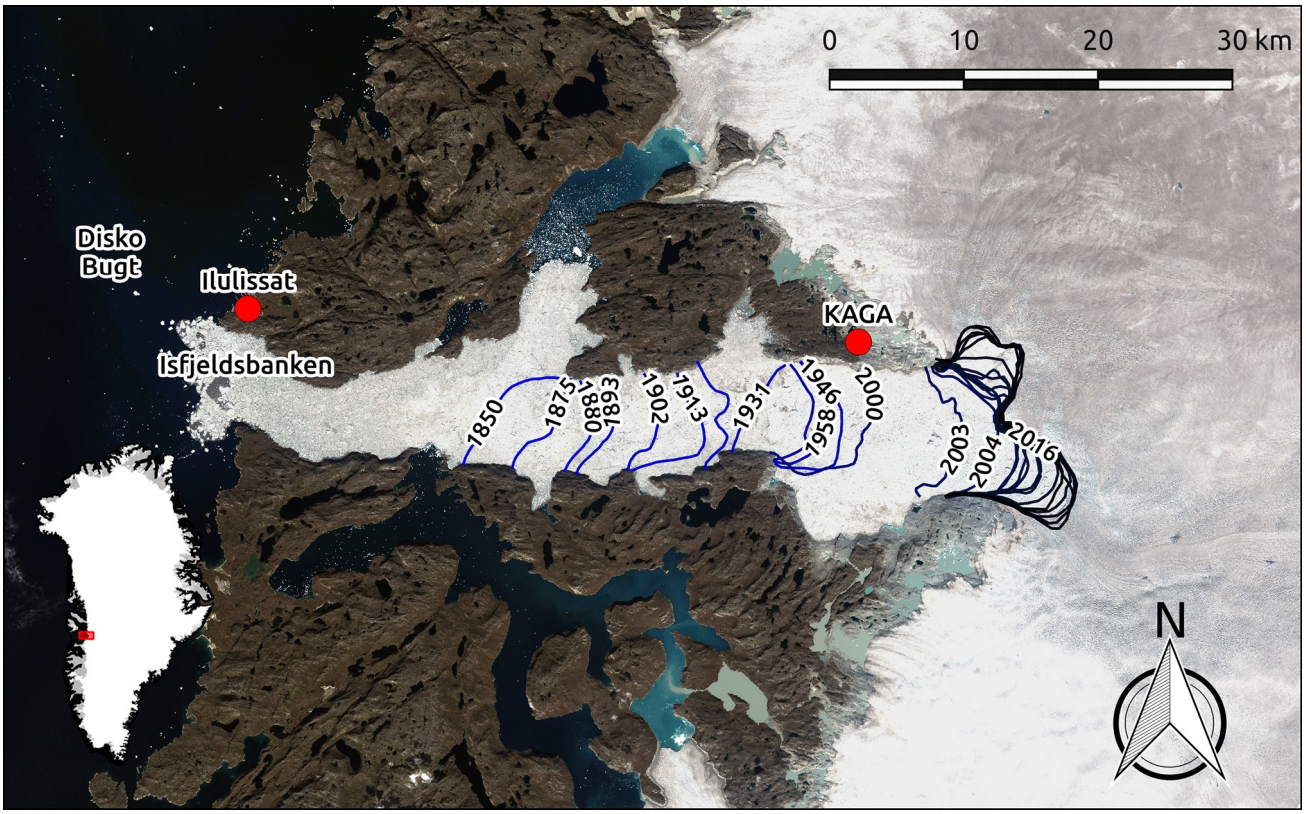

Fig. 9: Position of the calving front of Sermeq Kujalleq in Kangia from 1850 to 2016 (Steiger et al. 2018).

2 Methods

2.1 Data

Optical Sentinel-2 data

For this research, the main data was derived from the Sentinel-2 satellite mission, which is part of the European Space Agency's program Copernicus (ESA 2015). The MultiSpectral Instruments (MSI) onboard each of the two satellites Sentinel-2A and Sentinel-2B record multispectral images at a combined time interval of 5 days. At far northern latitudes, more frequent images are available due to overlapping orbits (see Fig. 10). However, the capabilities of Sentinel-2's instruments are limited to passive remote sensing, which makes them susceptible to obstruction by cloud cover. This often results in a significant reduction in the number of usable images obtained from space. Furthermore, the collection of Sentinel-2 data at high latitudes faces challenges during the winter months. The low angle of the sun, or its complete absence, impedes image acquisition, leading to a lack of data availability in these regions during this period. Since its inception with the launch of Sentinel-2A in 2015, all data from the Sentinel-2 mission has been openly accessible online. The MSI samples 13 bands with wavelengths in the visible and near-infrared spectra, at spatial resolutions between 10 and 60 meters (see Table 1).

Table 1: Bands recorded by the MultiSpectral Instrument (MSI) on the Sentinel-2 satellites (ESA 2015).

Band	Central Wavelength (nm)	Bandwidth (nm)	Spatial Resolution (m)	Primary Use
B1	443	20	60	Coastal aerosol
B2	490	65	10	Blue
B3	560	35	10	Green
B4	665	30	10	Red
B5	705	15	20	Red edge 1
B6	740	15	20	Red edge 2
B7	783	20	20	Red edge 3
B8	842	115	10	Near-infrared (NIR)
B8A	865	20	20	Red edge 4
B9	945	20	60	Water vapor
B10	1375	30	60	Cirrus
B11	1610	90	20	Shortwave infrared (SWIR) 1
B12	2190	180	20	Shortwave infrared (SWIR) 2

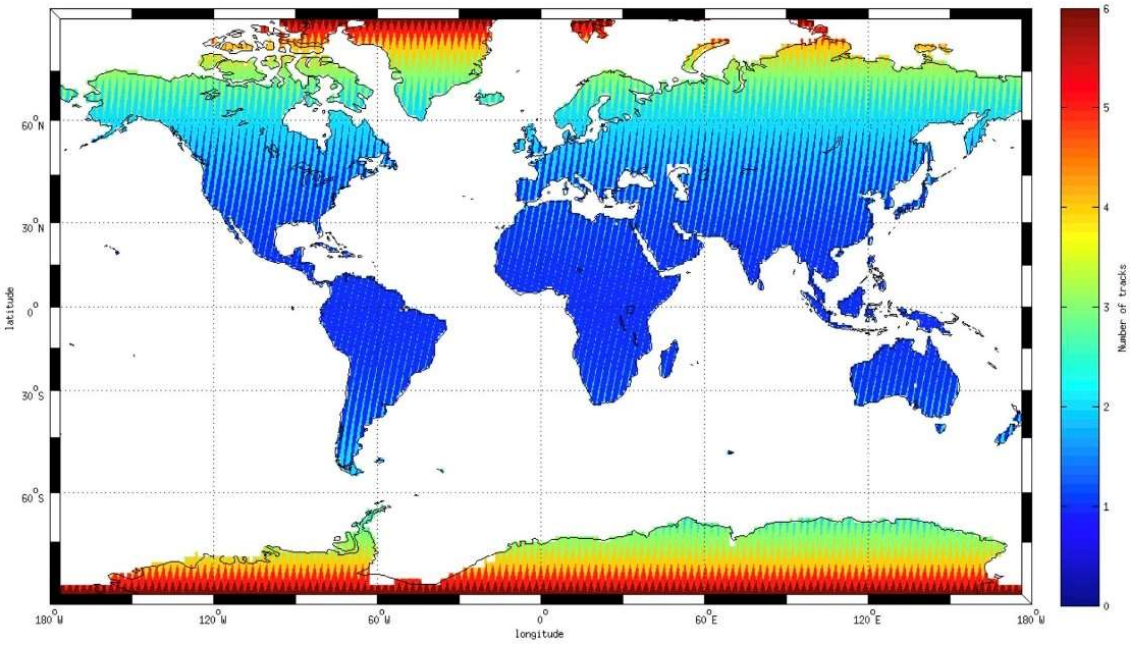

Fig. 10: Geometric revisit frequency of the Sentinel-2 satellite pair (tracks per 5 days) due to the overlap between adjacent orbits (Credits: Pascal Lacroix) (ESA 2015).

The raw data recorded by the MSI is processed by the ESA according to various steps before releasing them to the end user (see Fig. 11). Important steps in the data processing are the radiometric corrections and the geometric corrections (orthorectification and spatial registration). Since April 2022, all data has been processed up to Level-2A, which enhances Top-of-Atmosphere (TOA) Level-1C images with an Atmospheric Correction and a Scene Classification (SCL). The SCL algorithm allows the detection of clouds, cloud shadows, snow, water, and vegetation, providing useful additional information for image analysis (ESA 2015).

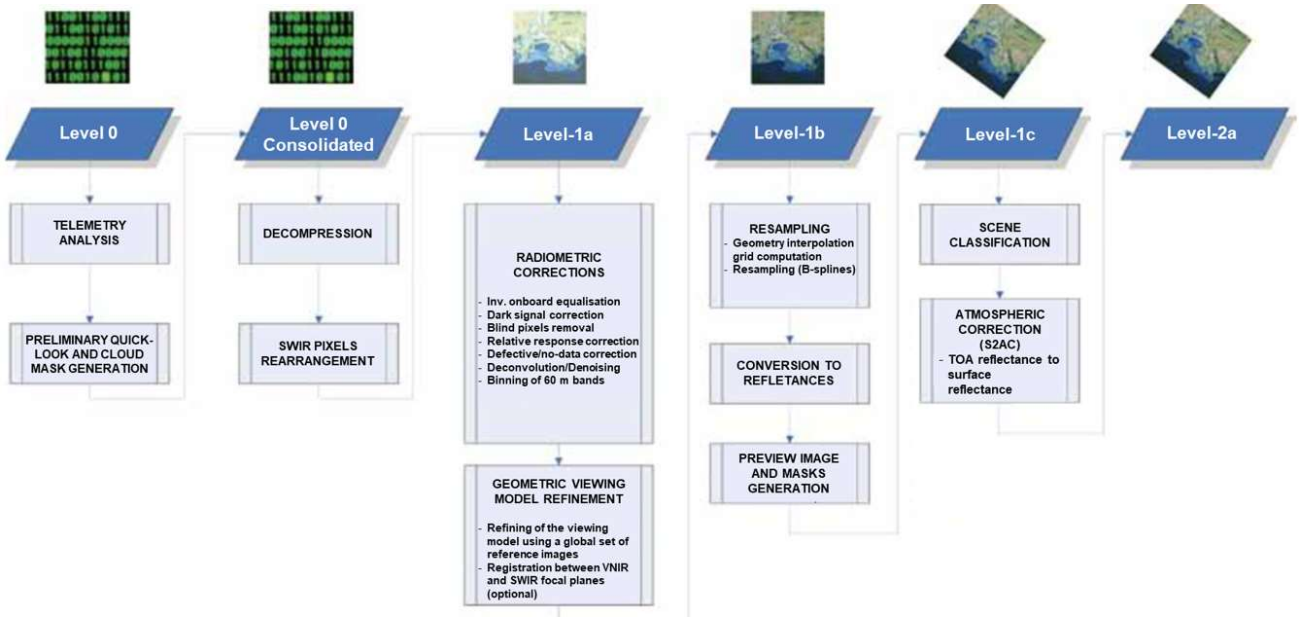

Fig. 11: Processing levels of Sentinel-2 data, from Level-0 (raw data), to Level-1C (with radiometric and geometric corrections), to Level-2A (with scene classification and atmospheric correction) (ESA 2015).

SAR Sentinel-1 data

Data from Sentinel-1 satellites, an integral part of the European Space Agency's (ESA) Copernicus program, was utilized to complement the information gathered from the optical Sentinel-2 imagery. Operating with a Synthetic Aperture Radar (SAR) at a frequency of 5.405GHz (C band), Sentinel-1 captures high-resolution images under all weather conditions and irrespective of daylight, a feature that greatly enhances its utility in a wide range of applications. The instruments on Sentinel-1 are capable of recording images in various modes, each tailored for different applications and offering distinct spatial and temporal resolutions. In the Interferometric Wide (IW) swath mode, tailored for land and coastal monitoring, the resolution is approximately 5x20 meters, covering a swath width of about 250 kilometers. This mode is useful for conducting detailed surface deformation studies and in disaster monitoring scenarios, as it allows for the detection of subtle surface changes via interferometry. The Extra Wide (EW) mode, on the other hand, is designed for maritime and polar applications, offering a wider swath of around 400 kilometers at a spatial resolution of about 20x40 meters. This makes it particularly suitable for large-area monitoring tasks, such as sea-ice mapping and tracking oceanic phenomena, where broad coverage is paramount. In addition to these, two other acquisition modes are available: Stripmap (SM) and Wave (WV). SM mode is employed for targeted observations, such as small islands or emergency events, while WV is the standard mode over open oceans. Both SM and WV modes provide a spatial resolution of 5x5 meters. Fig. 12 illustrates these various acquisition modes (European Space Agency (ESA) 2023).

In terms of temporal resolution, the Sentinel-1 satellites offer a revisiting frequency of 6 to 12 days at the equator, varying based on the number of operational satellites and their orbit configurations. An even more frequent revisit rate is experienced at higher latitudes, attributable to the same orbital overlap effect observed with the Sentinel-2 satellites. Furthermore, Synthetic Aperture Radar (SAR) data from Sentinel-1 can be captured in different polarizations, allowing for a more diverse and detailed perspective of the Earth's surface. This feature enhances the detection and classification of various surface features and changes. Four polarization combinations are available: VV (single co-polarization, vertical transmit/vertical receive), HH

(single co-polarization, horizontal transmit/horizontal receive), VV + VH (dual-band cross-polarization, vertical transmit/horizontal receive), and HH + HV (dual-band cross-polarization, horizontal transmit/vertical receive) (European Space Agency (ESA) 2023). Each polarization caters to different observational needs.
In our study area, the available Sentinel-1 Synthetic Aperture Radar (SAR) data is limited to HH and HH + HV polarizations. Moreover, limitations are observed in the type of acquired images for the years 2016 and 2017. Specifically, in 2016, there was a notable shortage of Interferometric Wide (IW) images, which offer higher resolution compared to EW images. The availability improved in 2017, with high-resolution images obtainable approximately every 12 days. This frequency increases in the following years, allowing access to high-resolution images every 3-5 days. For this research, Level-1 Ground Range Detected (GRD) data is utilized, which is available pre-processed in the Google Earth Engine catalog (Gorelick et al. 2017). This pre-processing involves the removal of thermal noise, radiometric calibration, and terrain correction utilizing the ASTER Global Digital Elevation Model (GDEM) (NASA/METI/AIST/Japan Spacesystems & U.S./Japan ASTER Science Team 2019).

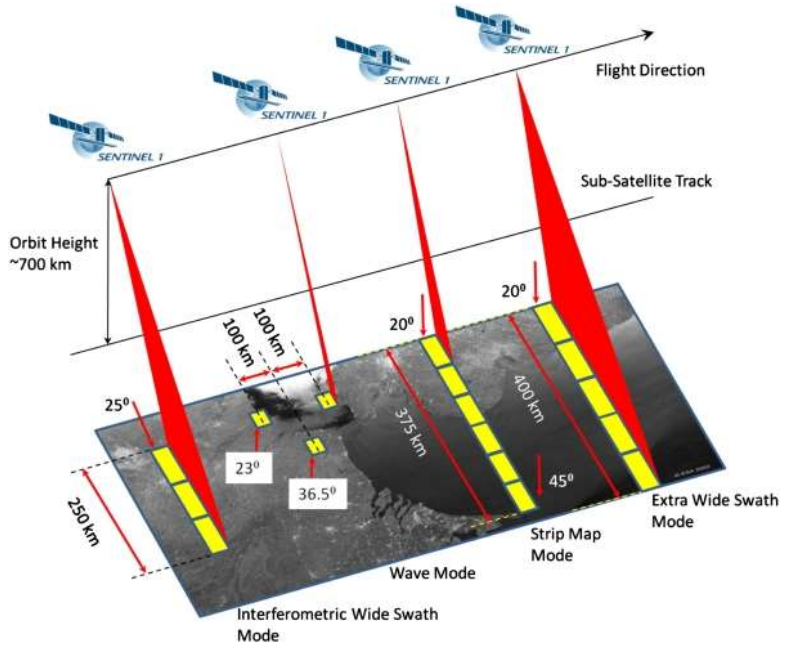

Fig. 12: Acquisition modes supported by the Sentinel-1 C-band Synthetic Aperture Radar (SAR) instrument (European Space Agency (ESA) 2023).

Ice velocity data

Information regarding the ice flow velocity of the SKK glacier is obtained from the National Snow and Ice Data Center (NSIDC). This center offers a comprehensive dataset encompassing ice velocities across Greenland, as detailed by Joughin et al. (2021). The velocity measurements are derived from image pairs captured by the TerraSAR-X and TanDEM-X satellites, operated by the German Aerospace Center (DLR). This dataset has been continuously available since June 2008 and offers an impressive temporal resolution of 11 days. In terms of spatial resolution, the data is detailed at 100x100 meter intervals, providing a fine-grained understanding of ice dynamics across the Greenland ice sheet.

Climate data

Climate data for this study is sourced from Ilulissat Airport's weather station, situated approximately 60 kilometers from the terminus of the glacier (refer to Fig. 8 of the study site). This data is provided by the Danish Meteorological Institute (Drost Jensen 2023). While not the ideal proximity, Ilulissat Airport's station is the nearest facility offering continuous weather data, particularly temperature records, for the entire duration from 2016 to 2022. Other proximal automatic weather stations, such as 'Swiss Camp' or 'JAR2', part of the Greenland Climate Network (GC-Net) (Vandecrux et al. 2023), are situated at a more suitable location to represent weather conditions at the SKK glacier. However, these stations' data records either contain substantial gaps or do not encompass the complete study period. To enhance the relevance of the

temperature data to our specific research needs, an altitude correction is applied. For analyses concerning supraglacial lakes, the temperature data is adjusted to reflect the mean altitude of the lakes under study, which is 780 meters above mean sea level (a.m.s.l.). This correction is performed using the standard temperature lapse rate of 0.65°C per 100 meters elevation gain. In contrast, for calving event analysis, the temperature data is not adjusted, as the altitude of the weather station (29 m a.m.s.l.) closely aligns with the sea level, rendering a correction unnecessary for this aspect of the study.

For this study, the Positive Degree Days (PDD) accumulated from the beginning of the year are the sole metric extracted from meteorological data. To test comparability, PDD calculations are derived from two sources: data from Swiss Camp and data from Ilulissat airport weather station, both adjusted to an altitude of 780 meters above sea level by using the standard temperature lapse rate. Fig. 13 presents a comparison of the PDD values obtained from these two locations. It is apparent that, with the exception of 2021, the onset of melt season typically aligns closely between the two stations. Data is completely missing in 2019 and 2020. In 2021, a notable discrepancy arises from the absence of data at Swiss Camp, which only became available after May 27th, 2021. By this date, the melt season has already commenced at the airport station. Furthermore, the count of days recording above-zero temperatures shows a significant discrepancy between the two weather stations and lacks a consistent pattern across the years. While this disparity should not be overlooked, the alignment of the melt season's onset between the two datasets suggests that the airport data is sufficiently accurate for the objectives of this study.

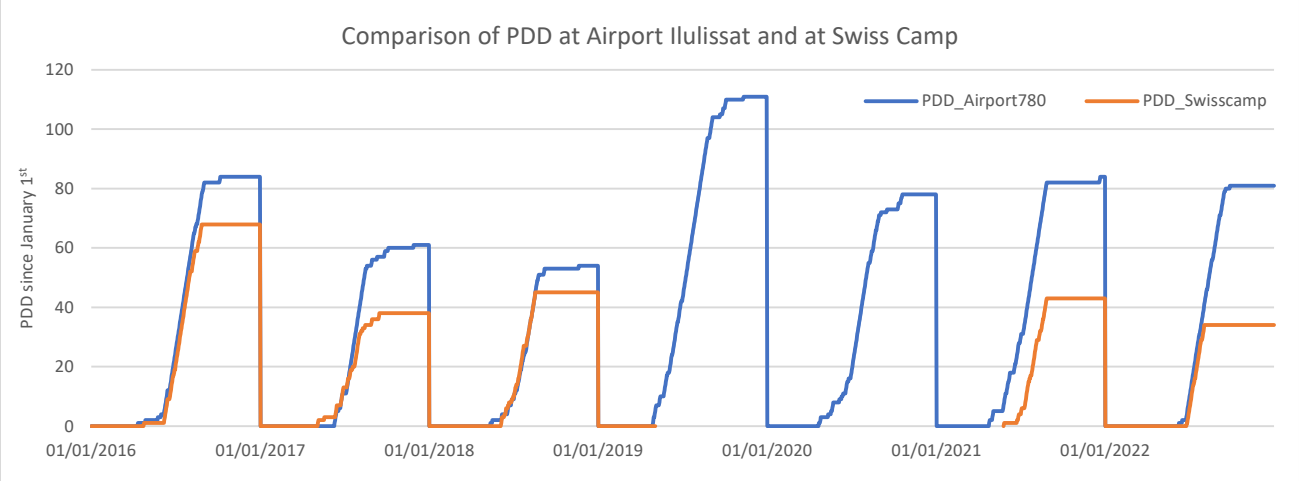

Fig. 13: Comparison of Positive Degree Days (PDD) since January 1st of each year, with temperature data from Ilulissat Airport and from Swiss Camp, both corrected to an altitude of 780 m above mean sea level by using the standard temperature lapse rate.

Digital Elevation Model (DEM)

For general information about the elevation of the glacier surface and its surroundings, a Digital Elevation Model (DEM) is required. The ArcticDEM (Porter et al. 2018), which was produced by the University of Minnesota Polar Geospatial Center by using optical stereo imagery and open-source photogrammetry software on high-performance computers, serves this purpose. It is a digital surface model of the Arctic with a precision of 2 meters and includes vegetation and man-made structures. Due to projection differences, it is first recorded in strips which are then compiled and blended into a mosaic and verified by IceSAT altimetry data.

Bed elevation data

The bed elevation data used in this study is based on airborne gravity data gathered in August 2012 as part of a scientific research project by An et al. (2017). The data collection involved flying a helicopter over a 500-meter grid at a lower speed and closer ground clearance than previous surveys, such as those conducted by NASA's Operation IceBridge (Cochran & Bell 2010; MacGregor & Harbeck 2023). Thereafter, the reconstruction of the bed elevation of the SKK glacier was achieved through a three-dimensional inversion that was constrained by offshore fjord bathymetry data and guided inland by a mass conservation algorithm (An et al.

2017). This approach resulted in a final dataset with a spatial resolution of 750 meters and a precision of 60 meters, offering a significant improvement over the 4700-meter resolution of the Operation IceBridge data.

Subglacial water flow paths

The findings from MacKie et al. (2021) are employed in this study to examine subglacial water flow paths connecting various supraglacial lakes, as well as the paths between these lakes and the glacier terminus. MacKie et al. (2021) utilized a bed elevation Digital Elevation Model (DEM) combined with mass conservation algorithms to conduct 250 simulations, mapping out potential subglacial water flow paths. Their results are presented as a heatmap, highlighting the most frequent and probable subglacial water streams.

Data availability chart

This study integrates various types of data from multiple sources. For a comprehensive analysis, data availability across the entire observation period is essential. The most significant data gap is in the Sentinel-2 L2A data, which is used for crevasse detection and tracking. Fig. 14 illustrates a timeline detailing the availability of this data, highlighting periods of data absence.

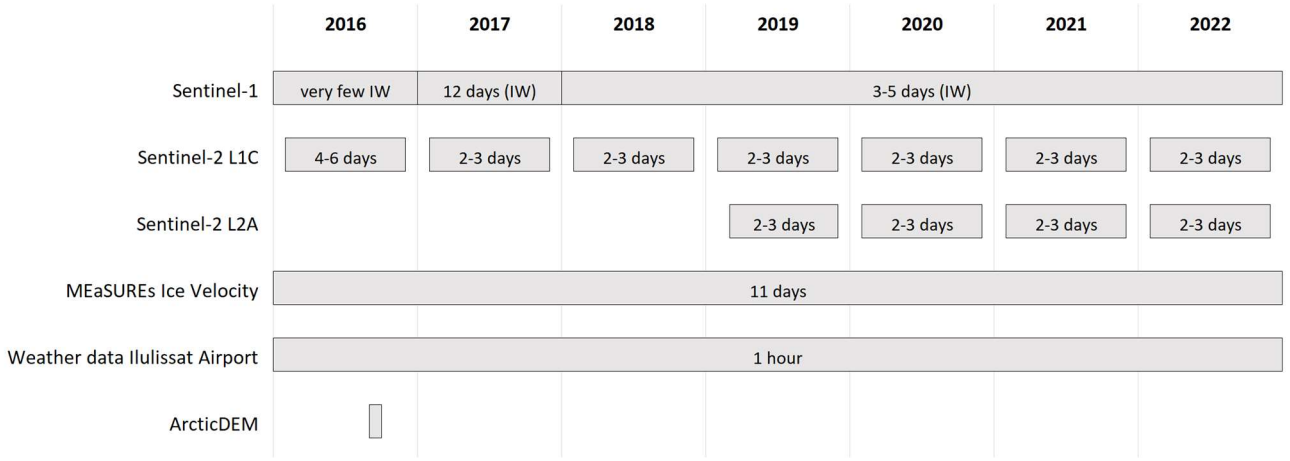

Fig. 14: Timeline of the availability of the data used in this study, and temporal resolution (in the boxes). For Sentinel-1 data the temporal resolution refers to Interferometric Wide (IW) images only.

2.2 Image processing tools

All spatial data in this study is processed and analyzed using Google Earth Engine (GEE) (Gorelick et al. 2017), a powerful cloud-based Geographic Information System (GIS) platform with an integrated JavaScript script editor. GEE's capability for on-the-fly data processing eliminates the need for preliminary data downloads, which is advantageous for time-series analyses where accumulating individual images can result in substantial data volumes and storage challenges. In GEE, images are automatically rendered in the correct coordinate system, streamlining the analysis process. GEE provides access to a vast archive of historical and contemporary geospatial datasets, facilitating detailed temporal comparisons and analyses. Users can also upload datasets that are not already in the GEE collection. The platform's server-side processing capacity allows for efficient handling of complex computations, reducing the demand for local computing resources. The integrated JavaScript editor supports the creation, testing, and refinement of custom scripts tailored to specific research needs, enhancing the platform's versatility as an analytical tool (Gorelick et al. 2017).

2.3 Detecting and mapping precursor crevasses

Finding calving events

To investigate calving events at the terminus of the SKK glacier, a comprehensive time series of satellite images is constructed using the Google Earth Engine (GEE) platform. The selected observational window spans over four years, from 2019 to 2022. To facilitate the rapid identification of calving events, animated sequences are generated, incorporating only images that exhibit a cloud cover of less than 20%, to avoid the occlusion of the calving front. To ensure the precise documentation and temporal correlation of each observed event, a

timestamp is superimposed on each image, allowing us to quickly deduce the approximate date of the calving events.

Detecting and mapping precursor crevasses

In this study, a systematic assessment of the impact of crevasses on calving processes is conducted using a fully manual approach. While automatic crevasse mapping algorithms have been explored in previous research (Bhardwaj et al. 2016), their capabilities do not yet support fully reliable and automatic detection. Additionally, this study requires mapping and tracking of specific crevasses along which calving events occur, a task not previously attempted. Given these requirements and the specific objectives of this research, a manual approach is deemed more suitable, ensuring precise delineation of the particular crevasses of interest.

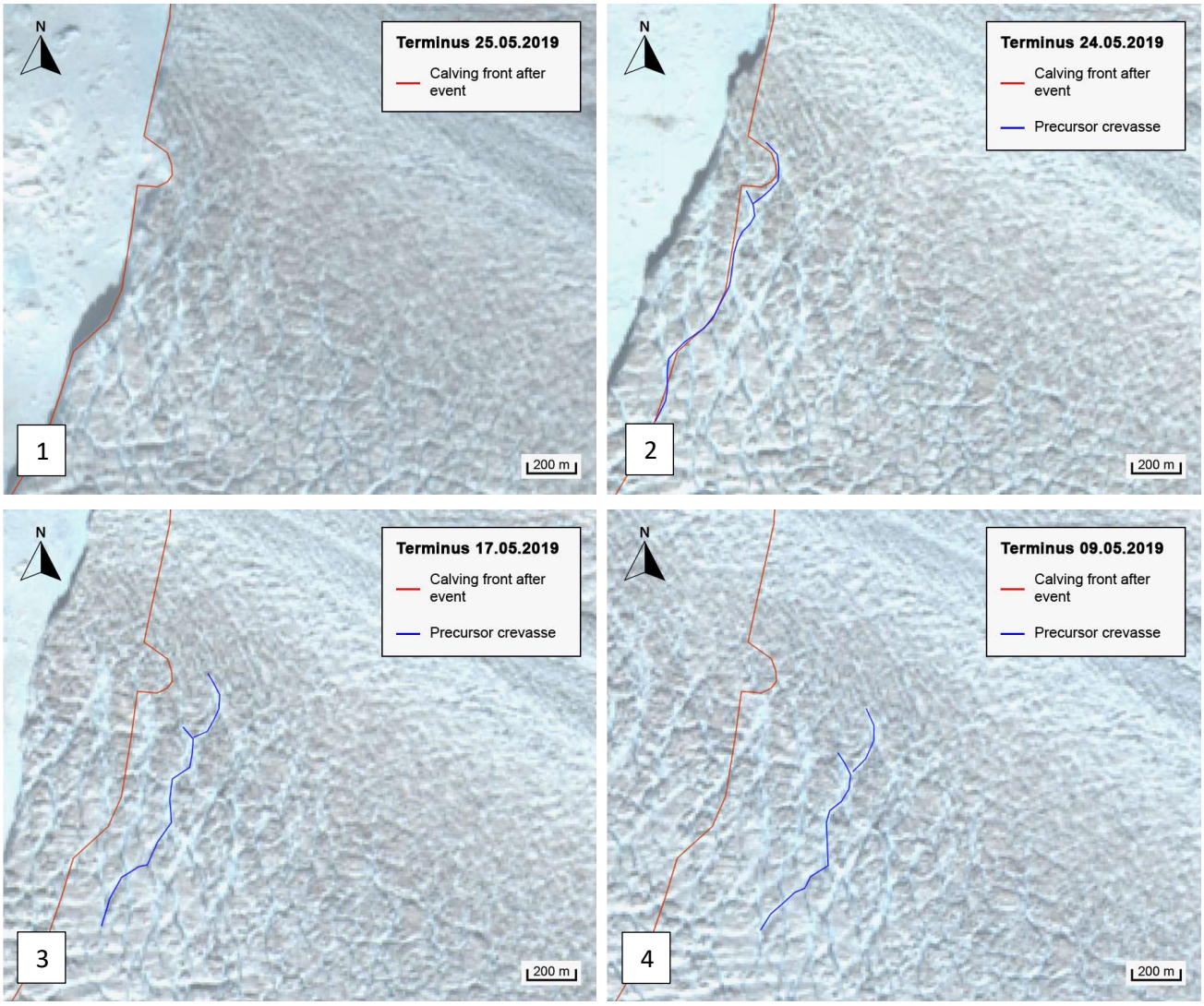

Fig. 15: Steps of the manual approach to find a precursor crevasse of the calving event on May 25th, 2019. In (1), the newly formed calving front is manually delineated by the red line. In (2), the position, orientation, and shape of the calving front are compared to crevasses in the area. The identified precursor crevasse is marked in blue. In steps (3) and (4) the precursor crevasse is tracked backward in time using available imagery. Note: the images only show part of the calving front, which has a total width of more than 6 kilometers.

To find out whether the rupture of a calving event propagated along preexisting crevasses in the ice, available optical imagery both before and succeeding the event is carefully analyzed. In the first step, the immediate post-event image is used to delineate the newly formed calving front, which is annotated with a red line (see an example in Fig. 15-1). Subsequently, the last image before the calving is reviewed, to ascertain any correspondence between the fresh calving front's morphology and the contours of previously observable crevasses. In cases where the emergent calving front appears to be congruent, in form, location, and spatial orientation, with a crevasse visible in previous imagery, that crevasse is classified as a 'precursor crevasse' for that particular calving event (see Fig. 15-2). To correctly identify and locate the crevasse in the imagery before

the calving event, it is imperative to account for ice flow and crevasse propagation. Notably, at the glacier's terminus, the flow velocity approximates 25-45 meters per day, as specified by previous studies (Hogg et al. 2015; Lemos et al. 2018). In the following steps, the precursor crevasse's historical progression is tracked backward by analyzing images from the preceding days (Fig. 15-3 and Fig. 15-4), until finding the date where it is first identifiable on the optical imagery. This systematic procedure is consistently applied to each investigated calving event and its associated precursor crevasses.

Collecting additional data

During a subsequent stage of the analytical process, comprehensive data about each calving event and their associated precursor crevasses are collected. The dates of the events are initially approximated as the mean of the dates of the nearest preceding and succeeding images. In a subsequent step, the dates are refined using Sentinel-1 SAR data, as described in section 2.5. The approximate calved area is measured through a comparative analysis of the Sentinel-2 imagery before and after the event. The accumulated Positive Degree Days (PDD) up to each calving event are calculated by using temperature data from the Ilulissat airport's meteorological station. Additionally, measurements are automatically conducted in GEE concerning the distance of the post-event calving front from a predefined zero point along a line representing the approximate ice flow direction (see Fig. 16). For each event the associated precursor crevasses are categorized by location on the glacier terminal zone, and the distance from their initially discernible location to the calving front are calculated. Furthermore, the lengths of the precursor crevasses as they first appear and shortly before the calving event are calculated, as well as the duration of their visibility.

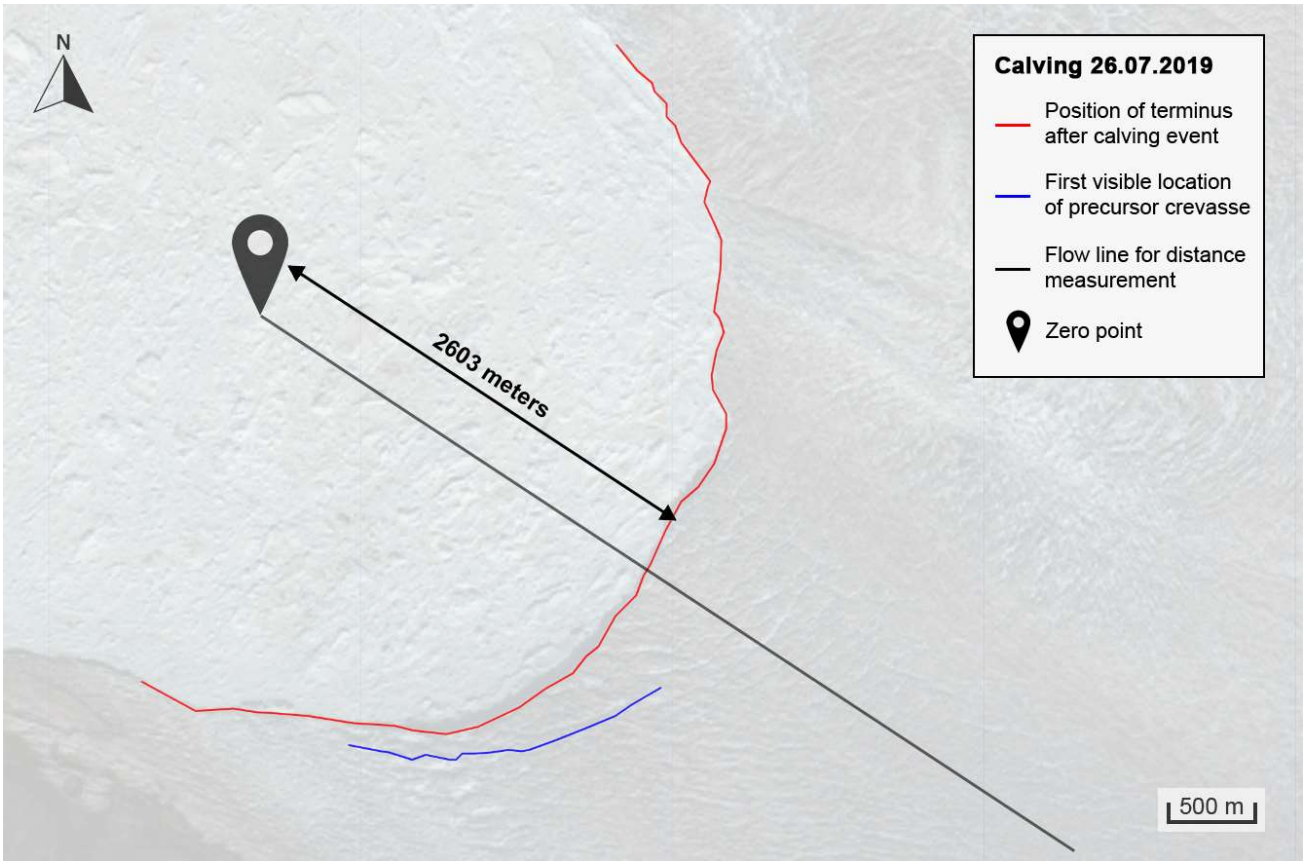

Fig. 16: Example measurement of the distance of the post-event calving front (red line) from the pre-defined zero point (black marker point), along the approximate glacier flow line (black line), for a calving event on July 26th, 2019. The blue line is a precursor crevasse corresponding to the calving event. The background image is for orientation purposes and does not correspond to the calving event.

To accurately determine the distance between a precursor crevasse and the calving front, it is crucial to smooth the line representing the crevasse. This step is necessary due to the frequent presence of abrupt edges or protruding sections in the crevasses' geometries, which could lead to wrong distance calculations, as GEE inherently calculates the minimum distance between two geometries. To overcome this challenge, a Simple Moving Average (SMA) smoothing algorithm is utilized. This method averages a set of data points over a

defined window size, producing a series of averaged values. For each vertex along the crevasse line, the SMA algorithm calculates the average based on its position and the positions of adjacent points within the window size. The algorithm generates a smoother, more generalized crevasse line, mitigating erratic fluctuations, as shown in Fig. 17. Selecting the optimal window size is a key aspect of this procedure. Various trials with different window sizes are conducted to achieve a smoothed line that accurately reflects an average of the original data points while minimizing distortions. A window size of 5 is ultimately chosen for the most satisfactory results. This approach allows for a more precise estimation of the average distance from the crevasse to the calving front, enhancing the accuracy of calculated propagation velocities of the crevasses, which are based on the distance and time difference between images.

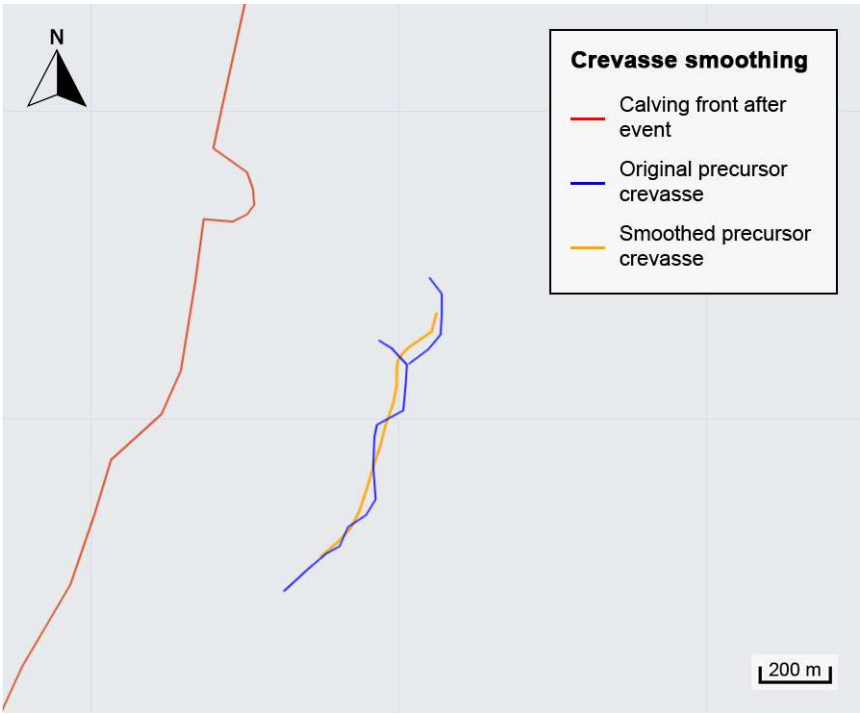

Fig. 17: A smoothing algorithm is applied to calculate an average line (in orange) representing the precursor crevasse (blue line). The result allows for a better distance calculation to the calving front (red line).

2.4 Supraglacial lakes

To gain more insights into calving dynamics and their influencing factors at the SKK glacier, supraglacial lakes surrounding the main ice stream are analyzed using optical images, with calculations conducted through a semi-automatic script in Google Earth Engine (GEE). This analysis utilizes Sentinel-2 Level-1C data from 2016 to 2022. Diverging from previous studies that employ automated techniques for lake detection (Miles et al. 2017; Moussavi et al. 2016; Williamson et al. 2018), this study is based on a manual lake selection process. The analytical approach concentrates on calculating the water areas of these selected lakes over time, with the lakes chosen based on their size and proximity to the SKK glacier. Williamson et al. (2018) indicate a strong correlation between the volume and the area of supraglacial lakes, suggesting that changes in lake area mirror changes in volume. Therefore, analyzing the lake area alone provides ample information to infer about the total lake size. Fig. 18 provides an overview of the lakes analyzed in this study. Lakes 'lk1', 'lk2', 'lk3', and 'lk11' are situated on the faster-moving part of the glacier, while the others are located along the sides. All these lakes fall within the SKK glacier's watershed, potentially influencing glacier dynamics. It is important to note that the red polygons outlining the selected lakes are not indicative of their actual sizes or shapes. Instead, these perimeters are chosen to encompass the maximum potential water area extension, including a margin for uncertainties.

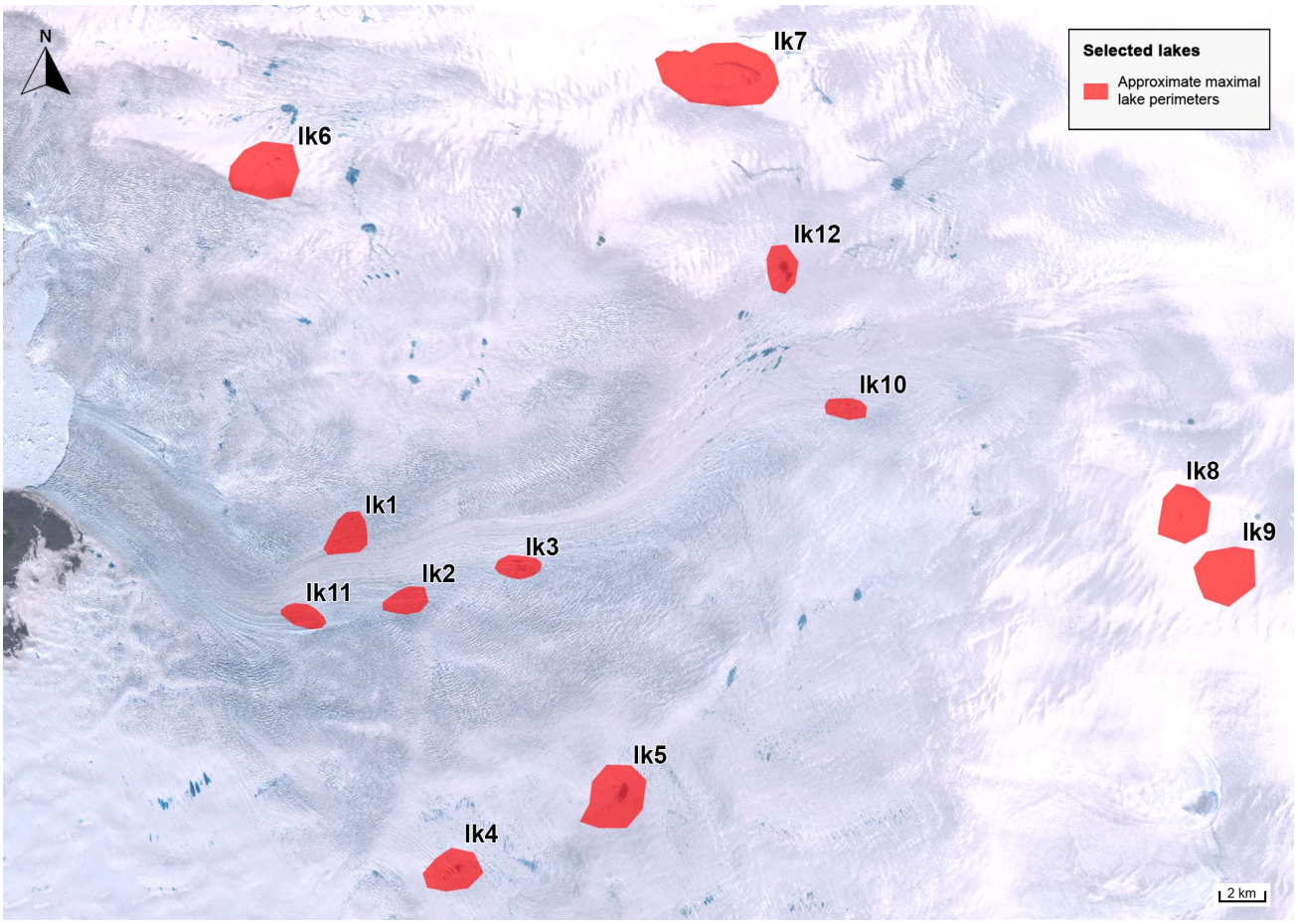

Fig. 18: Locations and approximate perimeters of the 12 selected lakes in the proximity of the SKK glacier. The red polygons are shaped in a way to encompass the lakes in their maximal areal extent (including a buffer) and thus do not represent the actual shapes of the lakes. The background is an RGB Sentinel-2 image recorded on May 12th, 2019.

Automatic lake area calculation

To calculate lake areas, the Normalized Difference Water Index (NDWI), a widely used metric for water detection, is computed based on Sentinel-2 data. NDWI traditionally contrasts the reflectance values of the green and near-infrared (NIR) bands (Condeça et al. 2022; McFeeters 1996; Singh et al. 2021), exploiting the fact that the reflectance of soil and terrestrial vegetation is much higher than the reflectance of water in the NIR band. However, in glaciological environments, this conventional method is not suitable due to the low NIR reflectances of snow, firn, and melting ice. Consequently, the modified $NDWI_{ice}$, proposed by Yang & Smith (2013), is employed. This adapted index utilizes the normalized ratio between the blue and red bands, which is more effective for discriminating water in glaciological settings. This adjusted index has been successfully applied and validated in several studies for identifying supraglacial lakes on the Greenland Ice Sheet (Miles et al. 2017; Moussavi et al. 2016; Williamson et al. 2018). For Sentinel-2 data, the $NDWI_{ice}$ formula is expressed as follows:

$$NDWI_{ice} = \frac{B2 - B4}{B2 + B4}$$

where B2 corresponds to the blue band (490 nm) and B4 to the red band (665 nm) of a Sentinel-2 image. The NDWI is computed for the entire study area, serving as a robust indicator of liquid water presence (see Fig. 19-2). Elevated NDWI values suggest a heightened likelihood of the presence of liquid water. Based on the research by Williamson et al. (2018), pixels manifesting NDWI values greater than 0.25 are categorized as aqueous regions (see Fig. 11-3). This threshold value is empirically confirmed by comparing the results of different values with the underlying true color image. Values of 0.23 or 0.27 vary the result only slightly. Employing a threshold of 0.25 demonstrates optimal precision and efficiency in differentiating between aqueous and non-aqueous areas on the glacier.

To retain only significant water bodies and to eliminate potential noise or minuscule water fragments, a spatial threshold of 100 pixels, equivalent to 10'000 m^2, is applied. Only water formations with an area exceeding this threshold are considered for the area calculation. Subsequently, to include any missing pixels located in the middle of the lake, within narrower sections, or along the edges – where the NDWI occasionally registers values beneath the 0.25 threshold – the lake mask is systematically expanded by one pixel (equivalent to 10 meters) in all directions. As delineated in Fig. 19-4, the refined image displays smoother and more continuous detected lake areas, whilst marginal water patches are successfully omitted. Considering that the lake mask encompasses all water bodies within the study area, the selected regions of interest around individual lakes, as illustrated in Fig. 19-5, are then applied. It is crucial to emphasize that each polygon is created to include an ample buffer zone around its respective lake. This design strategy ensures that each lake remains within the analytical boundary, even at its maximum spatial extent. Employing this methodology, the water areas of the 12 specifically chosen lakes are calculated individually, while excluding any other water bodies not encompassed within the predefined polygons. For every image in the dataset spanning from 2016 to 2022, and for each of the selected lakes, the water area is computed and subsequently exported to a table, along with the estimated cloud cover.

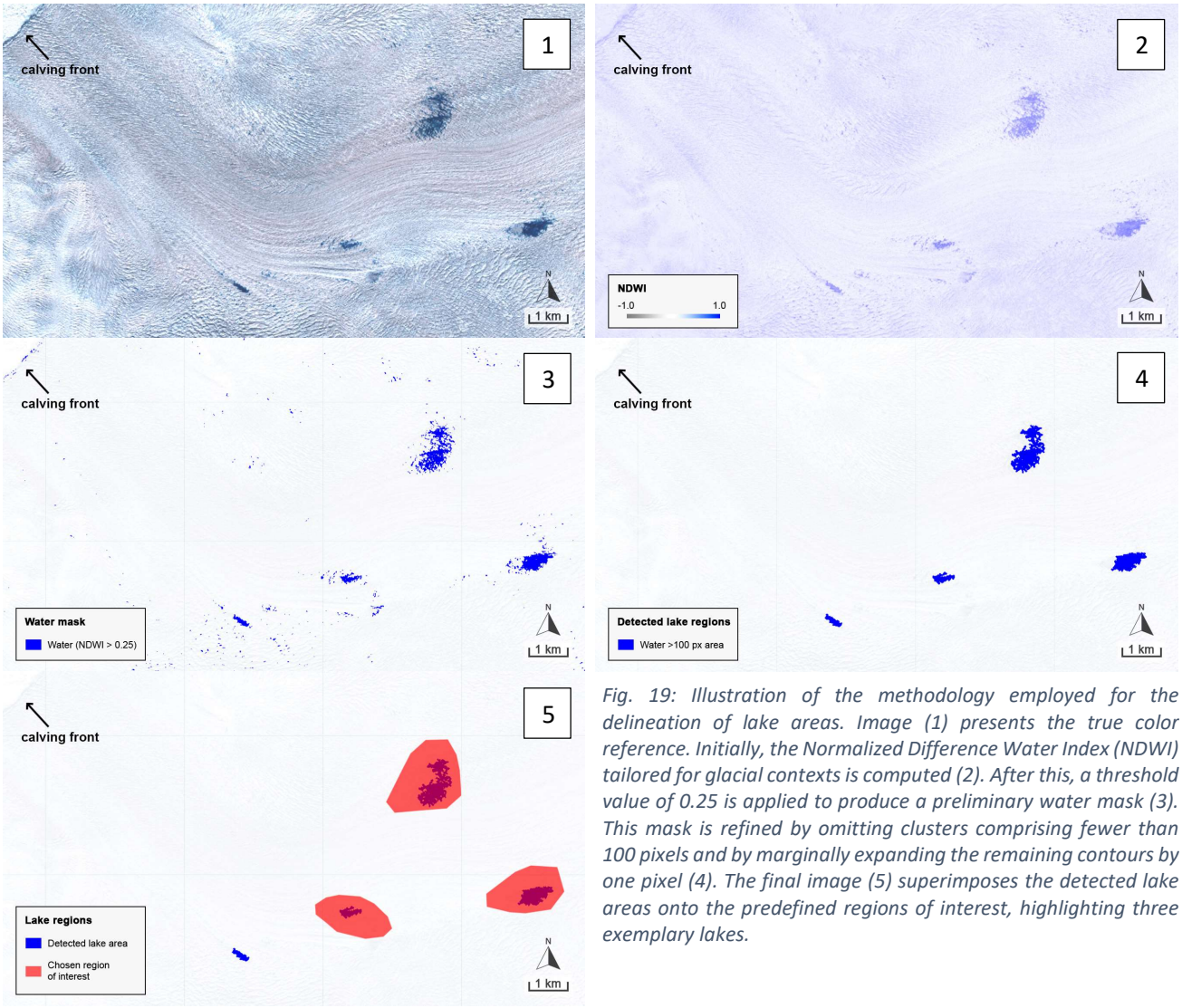

Fig. 19: Illustration of the methodology employed for the delineation of lake areas. Image (1) presents the true color reference. Initially, the Normalized Difference Water Index (NDWI) tailored for glacial contexts is computed (2). After this, a threshold value of 0.25 is applied to produce a preliminary water mask (3). This mask is refined by omitting clusters comprising fewer than 100 pixels and by marginally expanding the remaining contours by one pixel (4). The final image (5) superimposes the detected lake areas onto the predefined regions of interest, highlighting three exemplary lakes.

Manual data improvement

To enhance data quality, outliers and rows containing no data are manually removed. Initially, all rows with lake area values of zero are filtered out. This step is important for excluding images where clouds obscure a specific lake, resulting in a false zero water detection. However, it also removes instances where a lake has no visible water and isn't cloud-covered. Although this might exclude genuine cases of empty lakes, such scenarios are not critical for this analysis since preceding and subsequent area measurements can be utilized

to identify potential drainage events. To further improve the data and remove the remaining outliers, a closer look at the individual images on the days with outlying values was required. This is done manually, by analyzing each image in which the calculated area differs excessively from the surrounding values. In most cases, the difference is due to a thin or partial cloud cover, which falsifies the results. Outliers can also be identified by area values with decimal positions, as the script performs the calculation only to an accuracy of 100 m^2. Decimal positions are caused when the detected lake area intersects the pre-defined polygon that restricts the maximum possible lake area. In most cases, the intersection is due to a thin cloud layer falsifying the water mask and thus extending it beyond the foreseen perimeter (see Fig. 20), in some cases, the selected polygon was simply too small and had to be adjusted (see Fig. 21).

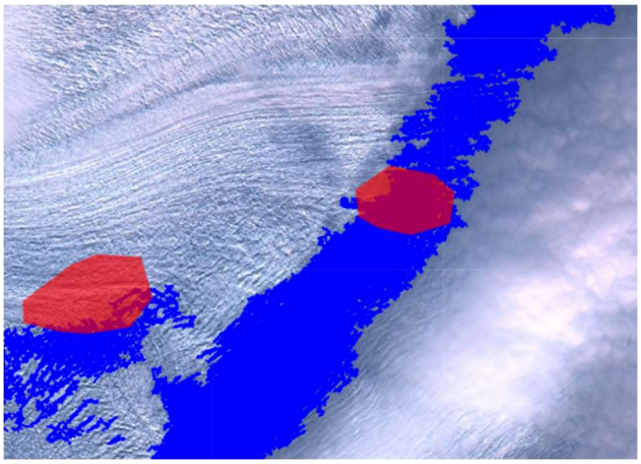

Fig. 20: In this example, clouds falsify the water mask and thus the detected lake surface (blue), extending beyond the selected maximum lake areas (red polygons) and yielding area values with decimal positions.

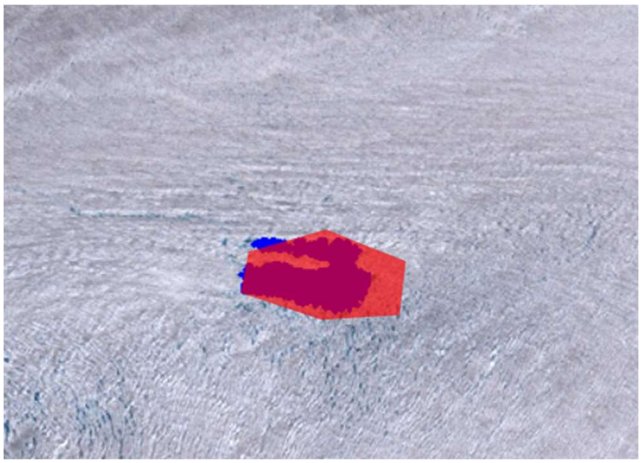

Fig. 21: The detected lake area (blue) extends beyond the selected maximum area for the given lake (red polygon), yielding a value with decimal positions. The polygon was subsequently enlarged.

Finding drainage events

The process of detecting potential drainage events is carried out manually by analyzing graphs depicting the evolution of lake areas over time. A meticulous examination of these area graphs over time is imperative to detect significant fluctuations that could be indicative of drainage events. Notably, in instances where a single data point exhibits an area significantly larger or smaller than its adjacent points, cautious interpretation is applied. A drainage event is only considered as such if at least two consecutive data points confirm an increase or decrease in lake area (see Fig. 22). This criterion is established to mitigate the risk of false positives, acknowledging the potential for miscalculations in the manually filtered, automatically generated data.

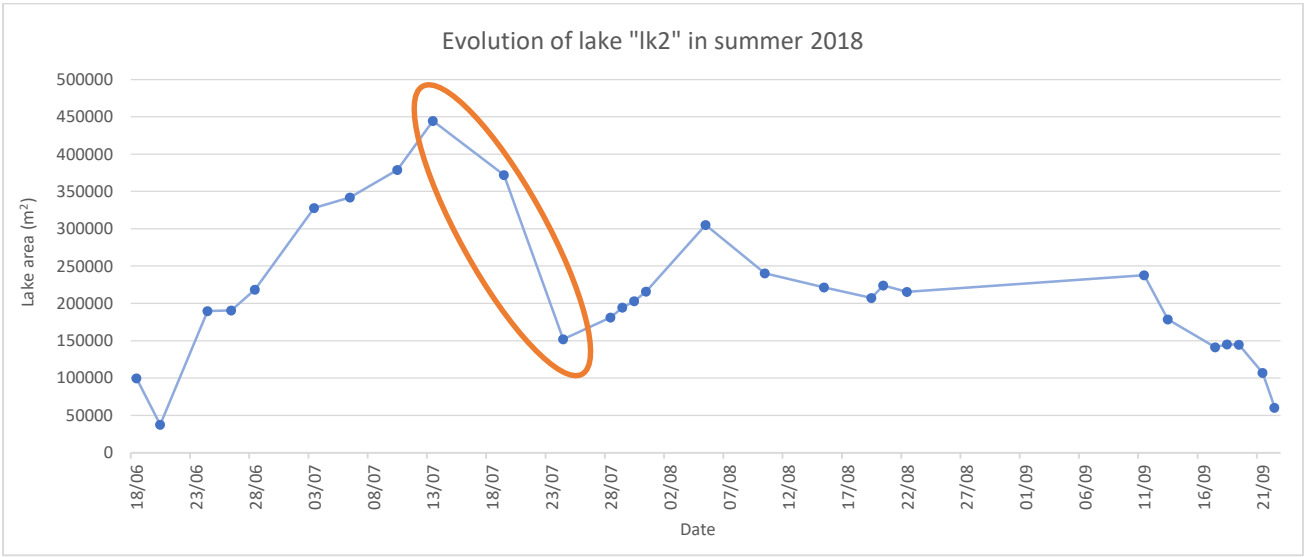

Fig. 22: Exemplary detection of a drainage event (marked in orange). The blue graph shows the temporal evolution of the lake area of 'lk2' in 2018. After July 12th, the lake area decreases and reaches a low on July 24th. The drainage event is confirmed by several data points on the graph and does not take place at the end of the season, as the lake slowly refills afterward.

To refine the detection of genuine drainage events, a distinction is made between those occurring within the melt season and those at the season's end. This differentiation is important as end-of-season events might be falsely identified due to the onset of ice coverage over the lake, which reduces the apparent lake area. To address this, a manual verification process is employed for all events initially marked as end-of-season drainages, using satellite imagery. This involves determining whether the event is an actual drainage or if ice is covering the lake's surface. Drainage events are often distinguishable by the altered color of the empty lake basin, as illustrated in Fig. 23 for lake 'lk4'. Events identified as ice coverage, as well as those where confirmation is inconclusive, are excluded from the drainage dataset.

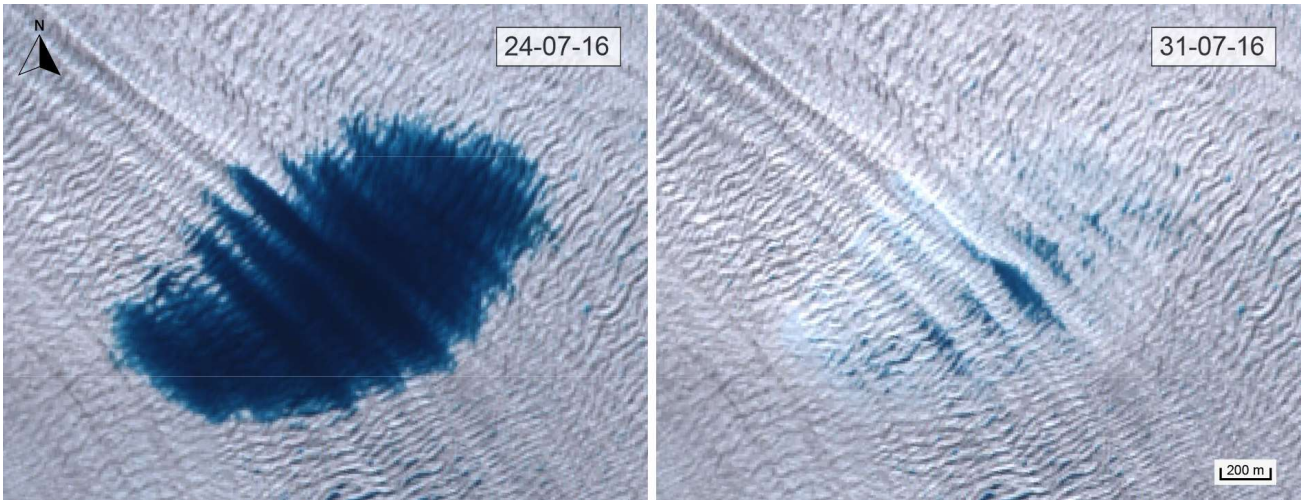

Fig. 23: Sentinel-2 RGB images capturing the drainage event of lake 'lk4' from July 24th to July 31st, 2016. In the post-drainage image, the outline of the former lake basin remains distinguishable due to the slightly brighter color of the ice.

Subsequently, a final manual review of the remaining drainage events is conducted to confirm their authenticity and, where possible, refine their dates. This includes manual corrections for instances where cloud cover covers the lake skewing the results, but the lake's boundaries are still clearly visible. This approach ensures a more accurate and reliable identification of lake drainage events and is instrumental in enhancing the quality of the dataset. To estimate the date of each drainage event, its duration, the loss in lake area, and the Positive Degree Days (PDD) immediately before and after the event, the last data point before the event and the first data point after the event are employed. Drainage events are then categorized based on their temporal characteristics. While definitions of a rapid drainage event differ, Miles et al. (2017) noted that several authors categorize it as a lake losing a minimum of 80% of its area within a period ranging from 2 to 6 days, depending on the specific study. For this research, an average duration of 4 days is selected as the criterion for rapid drainage events.

Cascading drainage events

To investigate potential cascading drainage events — where one lake drains and subsequently creates new pathways for water to flow from a lake at a lower altitude — a specific analysis is conducted. This involves date matching between the detected drainage events and establishing a possible sequence based on the lake elevation. Subsequently, the most probable water flow paths from the upper lakes to the lower lakes potentially part of a cascading event, are verified by using the subglacial flow map by MacKie et al. (2021). This step is crucial to determine whether water from the higher-altitude lake can flow toward the lake situated at a lower elevation.

Relation to calving events

To explore a potential link between the drainage of supraglacial lakes and large calving events, a search for coinciding events is conducted. The criteria established for this analysis stipulate that the calving event must occur within one week following the initiation of a lake drainage event. Subsequently, approximate water flow speeds are calculated, considering the time elapsed between the events and the estimated subglacial flow paths outlined by MacKie et al. (2021). Additionally, the subglacial water flow paths are cross-referenced with the locations of calving events on the terminus. Any instances where the ice calved off in areas distinctly

different from the predicted arrival points of subglacial water are excluded from consideration, ensuring a focused analysis on relevant and spatially correlated drainage and calving events.

2.5 Dating through SAR images

To enhance the accuracy in pinpointing the dates of calving and drainage events, Sentinel-1 Synthetic Aperture Radar (SAR) imagery (HH polarization) is employed. This data is particularly useful on days with extensive cloud cover that impedes optical imaging from Sentinel-2. However, the limited availability of high-resolution Interferometric Wide (IW) images in the years 2016 and 2017 restricts precise dating capabilities to the period from 2018 onwards. Fig. 24 illustrates an example of lake 'lk4' captured by SAR imagery, both before and after a drainage event. In the post-event image, the now-empty lake basin is visible, demonstrating the effectiveness of SAR imagery in detecting such changes.

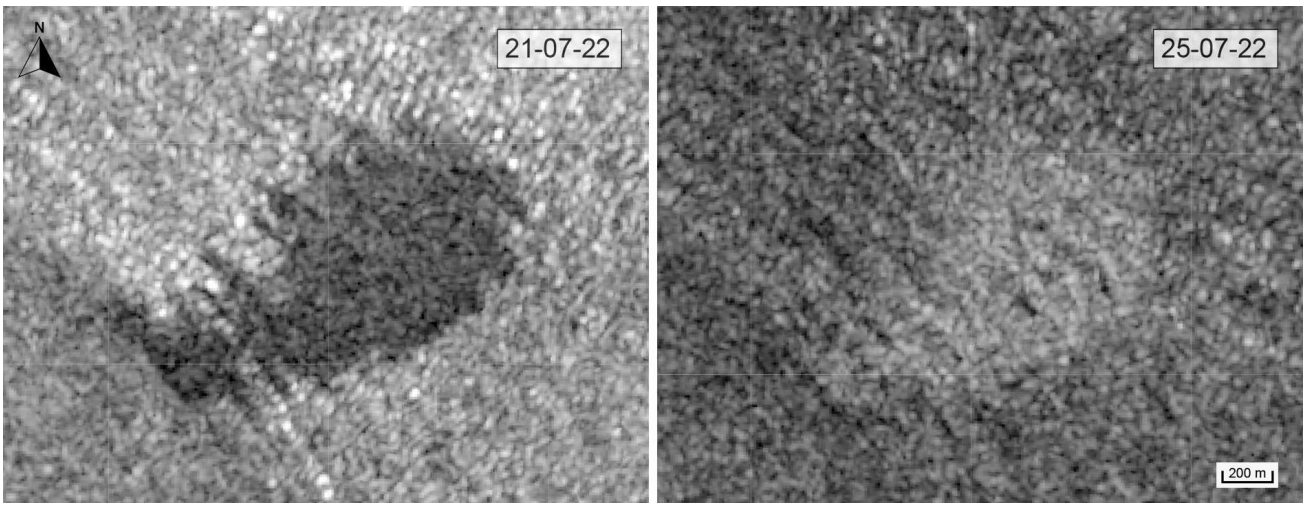

Fig. 24: Lake 'lk4' before (left) and after (right) a rapid drainage event, as seen on Sentinel-1 SAR IW image, HH polarisation.

2.6 Digital Elevation Model (DEM) and bed elevation

To analyze the ice surface elevation, including the altitudes of supraglacial lakes, the ArcticDEM digital elevation model (Porter et al. 2018) is employed. To visually better discern elevation changes, a version of the DEM with a reduced spatial resolution of 200 meters is calculated. This coarser resolution helps in highlighting broader altitudinal shifts across the glacier. The DEM analysis is complemented by the calculation of hillshade and slope angles, which facilitate the interpretation of the topographic data. Furthermore, bed elevation data from An et al. (2017) is used to understand glacier dynamics and explain zones prone to precursor crevasse formation. Three elevation profiles are constructed — two longitudinal and one lateral, relative to the glacier flow direction. These elevation profiles are specifically plotted through the area where the majority of precursor crevasses are observed, providing a focused analysis of potential precursor crevasse development sites.

2.7 Ice velocity

To examine the seasonality of glacier movement, as well as possible connections to calving or drainage events, a time series analysis of velocities is conducted using ice velocity data sourced from MEaSUREs (Joughin et al. 2021). Three fixed points on the glacier are strategically chosen based on their locations. Point 1 is positioned near the calving front, providing insights into the glacier's terminus dynamics. Point 2, situated approximately 8.2 kilometers from the calving front, marks the location just before the ice stream's northern turn. Finally, Point 3 is located further upglacier, about 5.6 kilometers from Point 2, offering a perspective on the dynamics of the upper part of the glacier's ablation zone. Additionally, to measure the ice flow velocity immediately behind the calving front, an algorithm is implemented to calculate a longitudinal velocity profile intersecting the calving front at the center of the fjord. Subsequently, a point between 200 and 300 meters behind the terminus is selected to represent the velocity at the calving front.

3 Results

3.1 Calving events and precursor crevasses

Analyzed calving events

The constructed animations based on Sentinel-2 imagery contain a variable frame count for each year due to frequent occlusion by cloud cover: 75 frames for 2019, 61 for 2020, 73 for 2021, and 19 for 2022. The criterion for image selection is a cloud cover below 20%. Across this period, 29 significant calving events are identified, with a higher detection frequency in 2019 and 2021. These higher numbers correlate with the greater availability of cloud-free images in these years.

Table 2: Summarized data of the analyzed calving events, ordered by date. In all except 6 events part of the rupture line follows one or more precursor crevasses (PC). The Positive Degree days (PDD) are calculated for the day of the calving event.

Date	PDD	Area (km²)	Dist from zero point (m)	Precursor crevasse PC	PC first visible (days before)	PC length (m)	Dist PC-terminus (m)
24/05/2019	32	0.47	699	middle	22	1201	591
				south	5	637	99
26/05/2019	34	1.26	1061	middle	29	457	740
				south	29	894	421
28/05/2019	36	1.53	1377	middle	1	1938	0
29/05/2019	37	0.4	1295	-			
23/06/2019	60	0.42	2061	south	12	1729	148
24/07/2019	92	0.51	2603	south	15	1859	129
04/08/2019	103	1.47	2910	south	8	1566	42
26/08/2019	126	0.67	2705	north	8	594	114
				middle	9	368	84
				south	9	735	158
21/05/2020	18	2.11	1638	-			
12/06/2020	38	0.62	2638	middle	1	1566	0
29/06/2020	55	1.32	3185	middle	9	618	187
				south	9	577	137
04/03/2021	0	2.88	2918	middle	15	506	497
				south	17	931	163
29/04/2021	9	4.22	2550	south	8	585	2
03/05/2021	13	0.65	2751	south	5	269	14
07/05/2021	15	1.21	2980	middle	32	765	1017
13/05/2021	20	1.33	3460	-			
15/05/2021	23	0.95	3798	-			
19/05/2021	27	0.57	3950	middle	8	1273	300
30/05/2021	36	1.79	4260	north	3	597	0
				middle	3	800	17
				south	26	410	386
02/06/2021	39	0.66	4423	north	5	782	179
04/06/2021	41	1.42	4609	north	1	509	43
				south	1	1796	0
28/06/2021	64	0.6	3490	north	23	1242	820
04/07/2021	72	2.67	4482	-			
22/07/2021	88	1.71	4589	-			
16/09/2021	139	6.95	3405	-			
07/06/2022	20	0.54	1956	south	12	1746	97
27/06/2022	40	1.65	2579	middle	7	562	155
				south	12	1699	118
09/07/2022	53	1.47	2680	far north	6	1526	0
				north	1	615	0
				middle	6	1886	57
03/08/2022	77	1.69	3774	far north	2	1257	0
				middle	2	2687	0

Key variables of the calving events are summarized in Table 2. Positive Degree Days (PDD) preceding these events range from 0 to 139, averaging at 49 days. The sizes of the calving events vary considerably, from 0.4 square kilometers to 6.95 square kilometers, with an overall average size of 1.51 square kilometers. Fig. 25 highlights 2021 as the year with both the most frequent and the largest calving events, and 2019 as the year

with the highest total number of PDD. Most events occur early in the melt season, but the largest event is observed towards the end of summer 2021.
Fig. 26 shows the post-calving morphologies of the glacier terminus colored by PDD, as well as the simplified flow line and the pre-defined zero point. A pattern emerges, showing certain areas along the glacier's flow line as more prone to calving. For quantification, a 'zero point' reference is established. Measurements from this point to the calving fronts yield an average distance of 2925 meters, within a range of 699 to 4609 meters. This distance demonstrates a slight increase from 2019 (average 1839 meters) to 2022 (average 2747 meters).

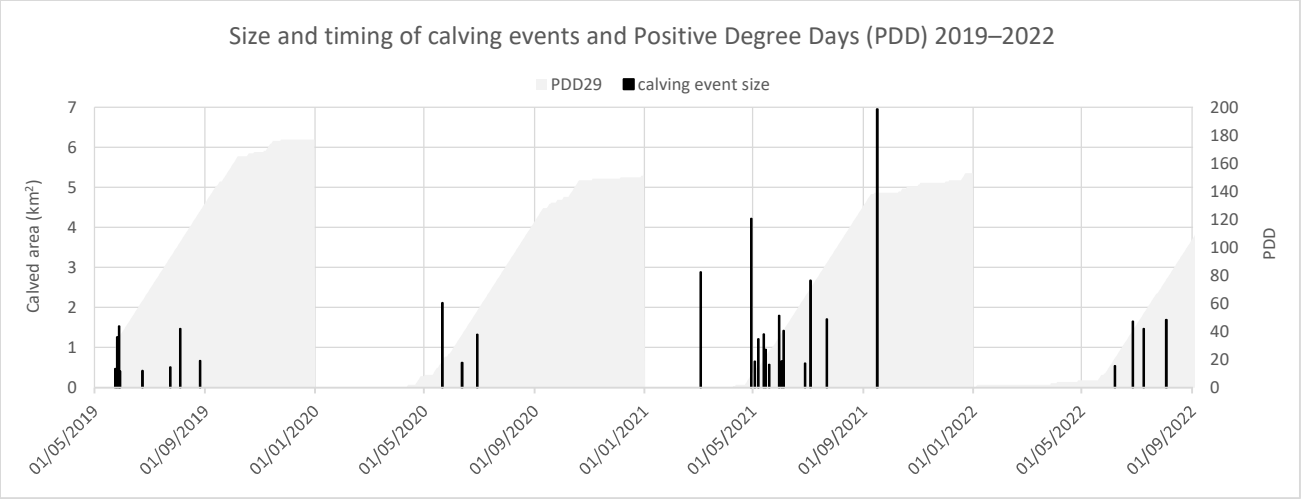

Fig. 25: Timeline from May 2019 to September 2022, showing all analyzed calving events and their sizes (black bars), as well as the Positive Degree Days (PDD) (grey). Since the study is based on optical imagery subject to cloud occlusion, the number of analyzed calving events per year is not representative of the actual number of calving events.

Identified precursor crevasses

In 6 of the 29 calving events, no part of the rupture coincides with a visible surface crevasse. For the remaining 23 events, at least one section of the rupture line follows a precursor crevasse identifiable in earlier images. These crevasses are scattered from the northernmost to the southernmost parts of the glacier terminus. No event involves a rupture line that completely traces a pre-existing crevasse. Precursor crevasses typically become first discernible on satellite imagery an average of 10.3 days before the calving events, ranging from 1 to 32 days. Initially visible at distances up to 1017 meters from the impending calving front (average 192 meters), these crevasses extended to lengths of up to 2.7 kilometers (average 1.1 kilometers). Their length changes by -455 to +1155 meters as they propagate towards the calving front.
The geometries of the precursor crevasses are visually represented in Fig. 27, which shows the initial appearance and orientation, colored by PDD. These crevasses are observed to emerge in a variety of locations across the glacier terminus, each displaying distinct orientations. However, within specific locations, the orientations of these crevasses exhibit a degree of consistency. A noteworthy concentration of these crevasses is found in the southern and central regions of the glacier terminus. It is also important to note the heterogeneity in the lengths of these crevasses and accumulated PDD, as they vary significantly across different calving events.
In this analysis, the calving events are categorized into four distinct groups, based on the distance of the calving front from the pre-defined zero point. Among these, 'Group 2', which encompasses calving fronts positioned near the average distance, exhibits a particularly interesting pattern. As shown in Fig. 28, this group reveals that all the precursor crevasses associated with these calving events consistently originate from the same region in the southern part of the glacier terminal zone. These calving fronts are observed to lie within a distance range of 2550 to 3185 meters from our established zero-point reference. Despite the precursor crevasses emerging from a similar geographical region, the resulting calving fronts exhibit variation in their shapes.

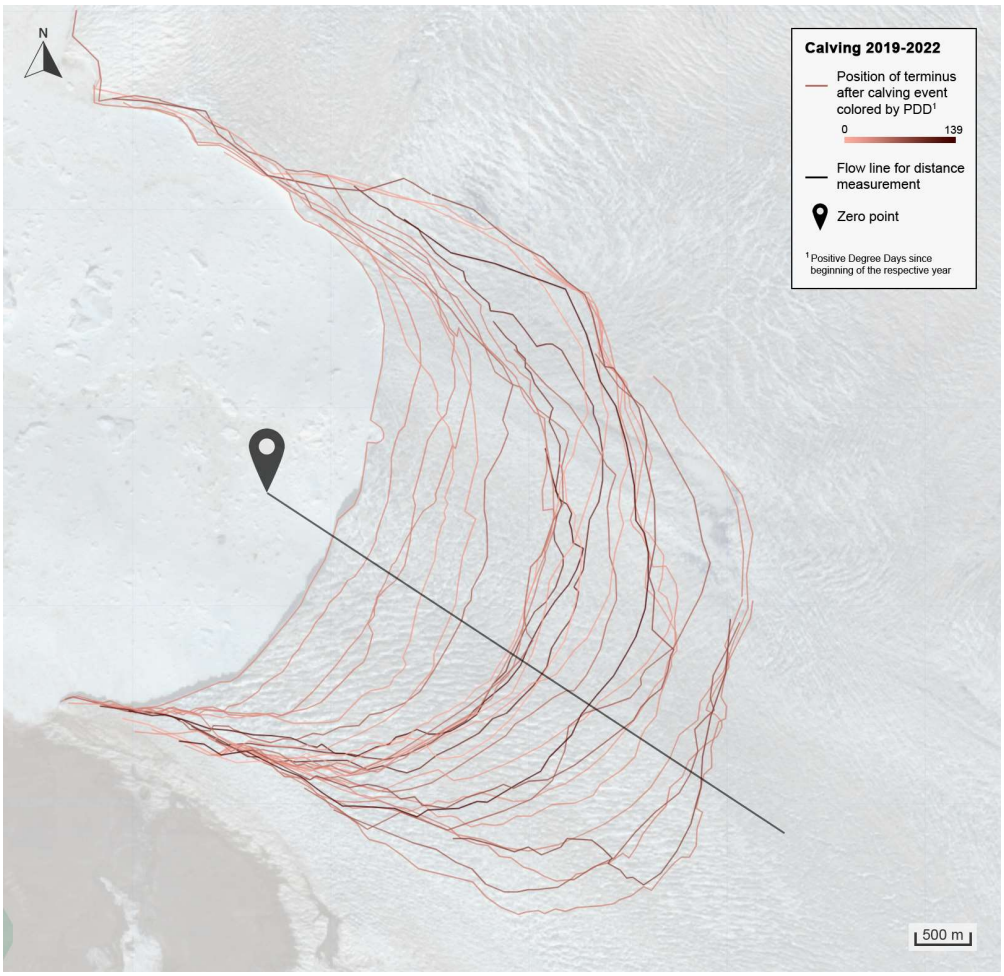

Fig. 26: Positions of the calving front following the analyzed calving events at the SKK glacier between 2019 and 2022. The lines are colored according to the sum of positive degree days (PDD) at the date of the respective event (darker = more PDD). The distance of the calving front from the zero point (black pin) is measured along the black line. In the background is a Sentinel-2 RGB image with 20% opacity, recorded on May 25th, 2019.

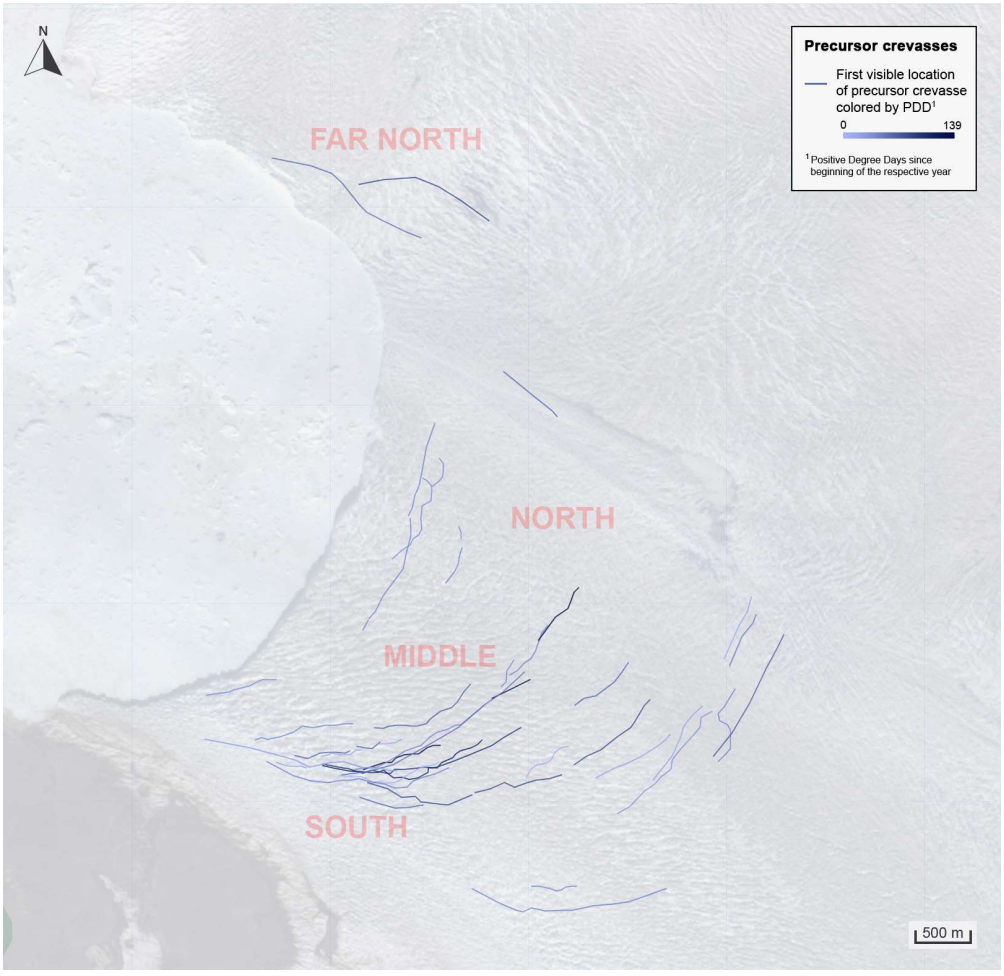

Fig. 27: First visible location of the precursor crevasses along which part of a calving event happened at the SKK glacier between 2019 and 2022. The lines are colored according to the sum of positive degree days (PDD) at the date of the respective event (darker = more PDD). In red font, the approximate location of the defined regions on the glacier terminal zone. More precursor crevasses seem to emerge in the southern and middle parts of the terminus. In the background is a Sentinel-2 RGB image with 20% opacity, recorded on May 25th, 2019.

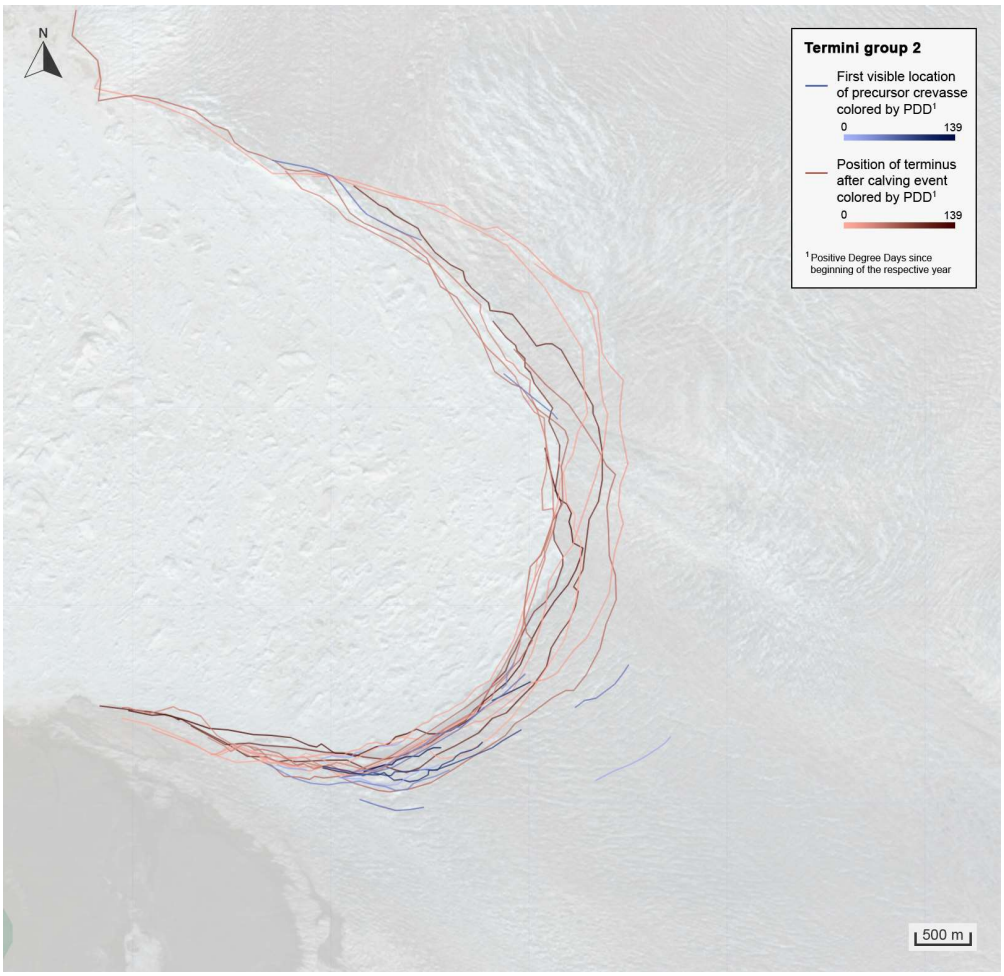

Fig. 28: Calving events at the SKK glacier between 2019 and 2022, filtered by front position between a distance of 2550 m and 3185 m from the pre-defined zero point. The lines in red tones delineate the calving fronts, while the lines in blue tones represent the associated main precursor crevasses at their first appearance on optical imagery. Both are graded based on their Positive Degree Days (PDD) since January 1st. Notably, the majority of these precursor crevasses originate from the southern part of the glacier terminus. In the background is a Sentinel-2 RGB image with 20% opacity, recorded on July 27th, 2019.

Statistical analysis

In the comprehensive analysis of the various collected variables, there is a predominantly weak correlation across most parameters. One exception, however, is observed in the correlation between the number of days a crevasse was visible in satellite imagery before a calving event and its distance from the glacier's terminus at first appearance. This relationship exhibits a significant positive correlation, with a Pearson correlation coefficient of 0.79, meaning that crevasses detectable earlier tend to be situated further from the terminus when they initially become visible. All other variables exhibit very low correlation coefficients.

Despite this overall trend, categorizing the precursor crevasses based on their geographical location on the glacier terminal zone reveals certain discernible patterns. As illustrated in Fig. 29, a comparison of precursor crevasse numbers in different regions of the terminus reveals a higher incidence in the southern (14 crevasses) and middle (13 crevasses) sections, compared to the lower numbers in the northern (6 crevasses) and far northern (2 crevasses) areas. Analyzing the average size of calving events reveals no considerable variation when correlated with the geographical locations of the crevasses. The analysis further extends to the average distance at which these precursor crevasses are first discernible. Here, a variation is noted based on their location along the terminal zone of the glacier: crevasses in the middle section appear at an average distance of 280 meters, while those in the northern and southern parts are identified at average distances of 193 meters and 137 meters respectively, as detailed in Fig. 30. This finding highlights a spatial variability in the initial visibility of crevasses.

The length of the precursor crevasses maintains a relative consistency across different locations, with average lengths ranging from 1102 meters to 1391 meters. This aspect of the data suggests that while the point of initiation for these crevasses varies depending on their geographical location on the terminus, their eventual size, once they become visible, remains comparatively similar across different areas.

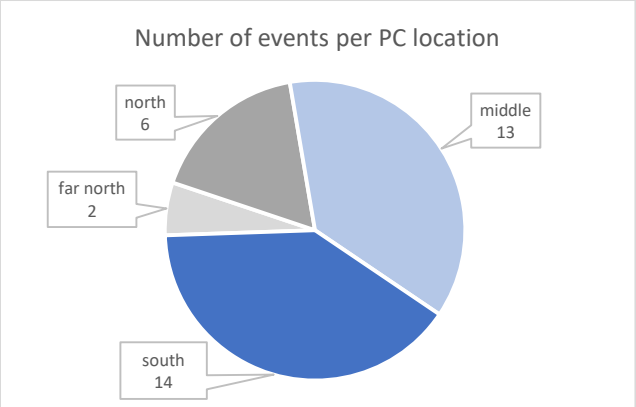

Fig. 29: Number of calving events associated with precursor crevasses at different locations on the glacier terminal zone.

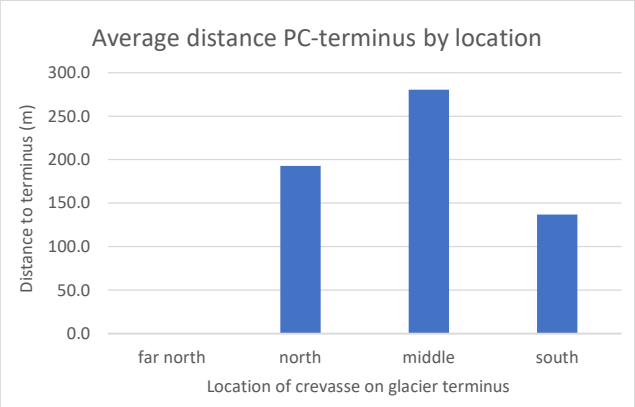

Fig. 30: Average calculated distance of the identified precursor crevasses, grouped by geographical location on the glacier terminal zone. In the far north part, the precursor crevasses were too close to the calving front to yield a result.

Distinct variations are noted in the velocities at which precursor crevasses traverse the glacier surface, as depicted in Fig. 31. This variation is particularly evident when comparing different geographical regions of the glacier terminal zone. Precursor crevasses located in the northern and middle sections are observed to move at a faster pace, averaging velocities of 16.4 meters per day and 14.1 meters per day, respectively. In contrast, the precursor crevasses in the southern region of the glacier terminal zone exhibit a notably slower propagation speed, advancing at an average rate of 7.6 meters per day. In the far north, velocity measurements for precursor crevasses are not feasible, as these crevasses are already positioned at the location of the future calving front upon their initial detection.

Additionally, our analysis uncovers a clear pattern in the temporal visibility of the precursor crevasses, which varies according to their location on the glacier. Precursor crevasses emerging from the middle and southern regions tend to become visible earlier before a calving event. On average, crevasses from the middle and southern regions are first observed 11.1 respectively 12 days before the calving event, while those in the north and far north appear on average 6.8 and 4 days in advance. This pattern is illustrated in Fig. 32.

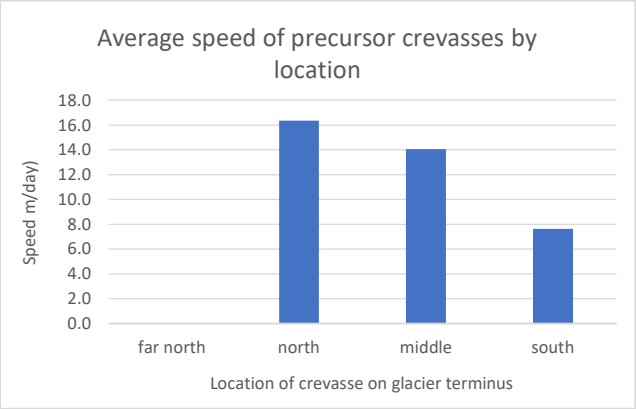

Fig. 31: Average calculated speed in meters per day of the identified precursor crevasses, grouped by geographical location on the glacier terminal zone. In the far north the precursor crevasses were too close to the calving front to calculate a speed.

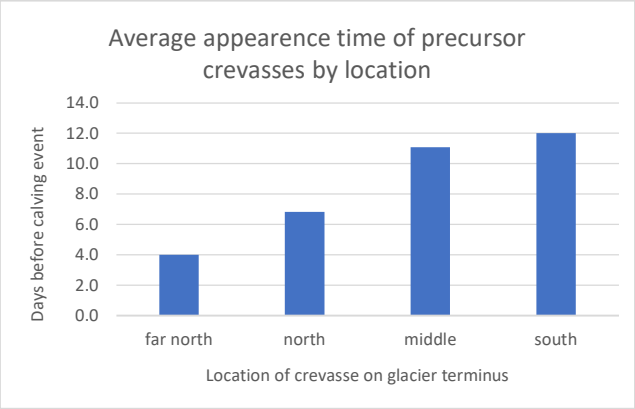

Fig. 32: Average appearance time in days before the calving event of the identified precursor crevasses, grouped by their geographical location on the glacier terminal zone.

The variation in the length changes of precursor crevasses, from the moment they first become discernible on satellite imagery to shortly before the calving event, is documented across different locations on the glacier terminal zone, as detailed in Fig. 33. A notable observation is that precursor crevasses in the middle section of the terminal zone show the most consistent pattern, exhibiting lengthening exclusively, with changes ranging from 0 to 489 meters. In contrast, crevasses in the far northern part of the terminus demonstrate a contrasting behavior, with observed shortenings up to -237 meters. The precursor crevasses situated in the northern and southern regions of the terminus exhibit a broader spectrum of length changes, experiencing both shortenings and lengthenings, and spanning a wide range of values.

An additional aspect involves the comparison between the number of Positive Degree Days (PDD) and the size of the resulting calving events, as depicted in Fig. 34. This comparison reveals that there is no apparent dependence of the calved area on the PDD, indicating that calving events of similar sizes can occur at various points throughout the melt season. However, the data again emphasizes that the majority of calving events tend to occur in the initial third of the melt season. Notably, the largest calving event in our study, which involved an area of 6.95 km², coincides with the highest recorded PDD value of 139.

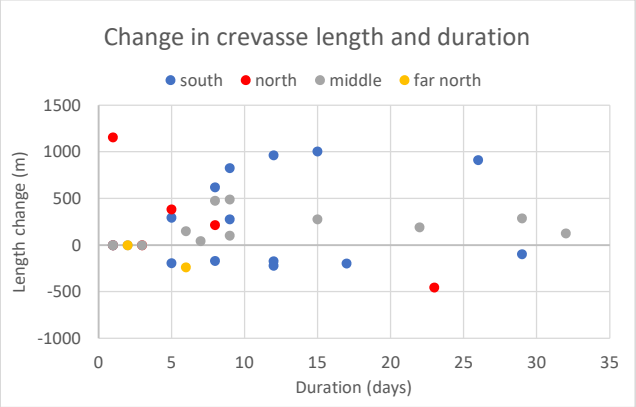

Fig. 33: Change in length of precursor crevasses from the image it became first visible until the last image before the calving event, and the elapsed time between these two images.

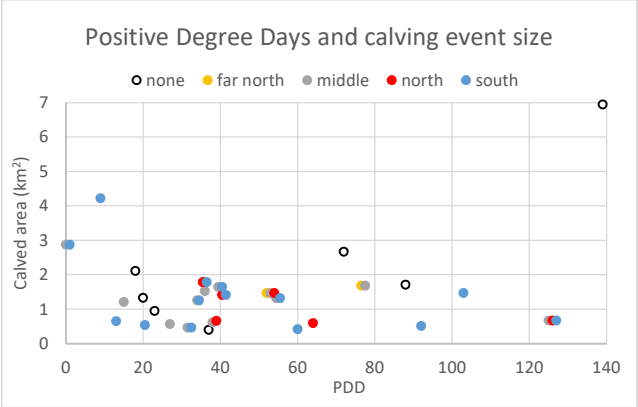

Fig. 34: Cumulative Positive Degree Days (PDD) at the time of calving, and estimated total area calved.

Calving events and ice velocity

The collected data reveals that during the study period, certain larger calving events appear to coincide with a slight increase in glacier velocity. Out of the 29 calving events analyzed, 3 are observed to occur almost simultaneously with the commencement of an increase in the glacier's flow speed. The calved areas of two of these events are approximately 1.47 square kilometers each, while the third event is significantly larger, involving an area of 6.95 square kilometers. Concurrent with these calving events, the glacier experiences a speedup ranging from 3.1% to 7.5%. The peak velocity is recorded between 4 and 28 days post-calving. These specific events, along with their associated glacier speed-ups, are summarized in Table 3.

Table 3: Calving events for which an increase in ice velocity is detected on similar dates. Before these events, the trend of the ice velocity is decreasing. The ice speedup is calculated using the velocity before the event and the associated peak velocity.

Calving event	Area (km²)	Velocity (before event, m/day)	Time until peak velocity (days)	Ice speedup
04/08/2019	1.47	27.9	28	7.5%
16/09/2021	6.95	35.7	8	3.1%
09/07/2022	1.47	27.6	4	4.3%

3.2 Supraglacial Lakes

Evolution of lake areas

The analysis of the temporal evolutions of 12 supraglacial lakes on the SKK glacier, spanning from 2016 to 2022, reveals substantial annual variability in their filling patterns. This variability is exemplified in the graph of lake 'lk7', as depicted in Fig. 35, with additional graphs of all lakes provided in Appendix II. Notably, these lakes do not exhibit a common pattern of filling over the years. For instance, in a given year, one lake might experience significant filling, while another may show no filling at all. This pattern of irregularity is particularly pronounced in lakes 'lk6' and 'lk7', both of which display the strongest year-to-year area fluctuations. Throughout the seven years, 'lk7' consistently alternates between years with a large water area and years with a smaller water area. Lakes located at lower altitudes on the glacier, such as 'lk1', 'lk2', 'lk3', and 'lk11', undergo frequent cycles of filling and draining within the seasons, and their areas change more subtly compared to other lakes.

The 12 lakes studied are distributed over a significant elevation gradient on the glacier, ranging from the lowest at 284 meters above sea level to the highest at 1216 meters, averaging approximately 779.7 meters in altitude. The maximum areas of these lakes vary widely, from as little as 0.2 square kilometers to as much as 3.59 square kilometers, with an average maximum size of around 1.29 square kilometers. It is observed that lakes situated at lower altitudes tend to be smaller, as shown in Fig. 36.

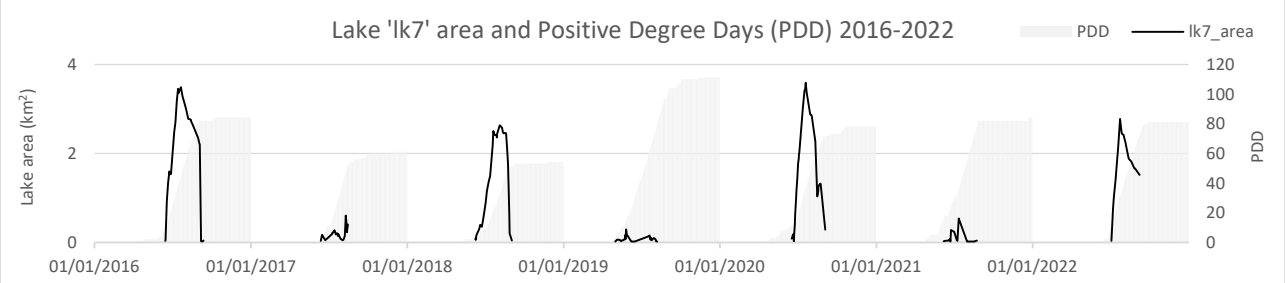

Fig. 35: Temporal evolution of the area of lake 'lk7' from 2016 to 2022 (black line). The grey-shaded areas are the cumulative Positive Degree Days (PDD).

The data collected on the supraglacial lakes reveals noticeable gaps outside the summer months, resulting in undetermined areas for the winter season. For lakes located on the fast-moving part of the glacier, the corresponding lines on the graph exhibit more erratic fluctuations. Nevertheless, the overall trend of area changes, encompassing multiple filling and draining cycles within a single season, is clearly discernible. In comparison, lakes situated directly on the ice stream show a slower rate of area change than those positioned on the peripheries of the main glacial flow. The graphs of lakes located more peripherally to the fast-moving ice display smoother and less erratic patterns. Despite these differences, a common trend is observed in all lakes, regardless of their location. Each begins to fill at the onset of the melt season, as indicated by the low Positive Degree Days (PDD) values, and does not exhibit a plateau phase where the lake area would stabilize. Instead, the graphical representations for all lakes consistently show an initial increase in water area, followed immediately by a decrease. Consequently, lake draining often occurs early in the melt season. Towards the end of the season, variations are noted among the lakes. Some, such as 'lk6', 'lk9', and 'lk12', are frequently almost empty, whereas others like 'lk4' in 2019, 'lk5' in 2021 and 2022, and 'lk8' in 2020, reach their maximum area for the season as the last recorded state before the onset of winter.

Drainage events

During the study period from 2016 to 2022, a total of 63 drainage events are identified across the 12 lakes under examination. As illustrated in Fig. 36, the frequency of drainage events shows a higher occurrence in the two lowest lakes, with each experiencing 11 drainage events. This frequency tends to diminish with increasing lake elevation. The accumulation of Positive Degree Days (PDD) from the start of the year to the onset of each drainage event ranges from 1 to 90 days, with an average of 27 days. This suggests a tendency for more drainage events to occur earlier in the year. Fig. 38 reinforces this observation, indicating that 56% of drainage events happen in the first third of the melt season, 35% in the second third, and a mere 9% in the final third.

The area reductions during these drainage events vary considerably, from a minimal 0.022 square kilometers to a substantial 1.48 square kilometers. These reductions correspond to losses ranging from 13% to an extensive 98.3% of the lake area before the event, with the average reduction being 73.1%. Notably, 33 events recorded area losses exceeding 80%, indicative of near-complete drainage. The distribution of these relative area losses is depicted in Fig. 39. The duration of the drainage events also varies considerably, ranging from as brief as a single day to as long as 36 days, averaging around 9.3 days. As shown in Fig. 40, most drainage events conclude in less than 10 days, with only 7 events extending beyond 20 days. Out of the total events, 41 are categorized as slow drainage, 22 as rapid drainage, and 13 as rapid drainage with an area loss above 80%, as detailed in Fig. 41.

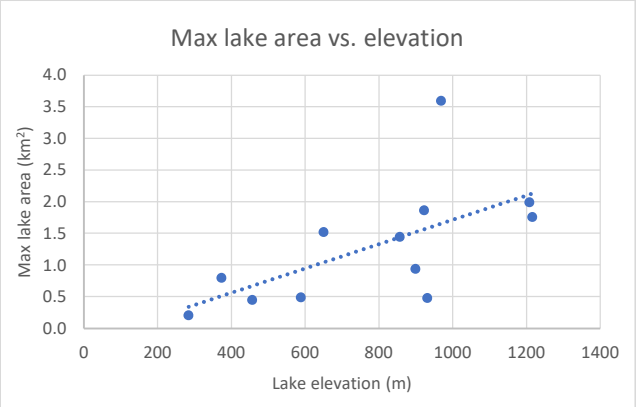

Fig. 36: Maximum lake area detected between 2016 and 2022, and mean elevation above sea level of the lake.

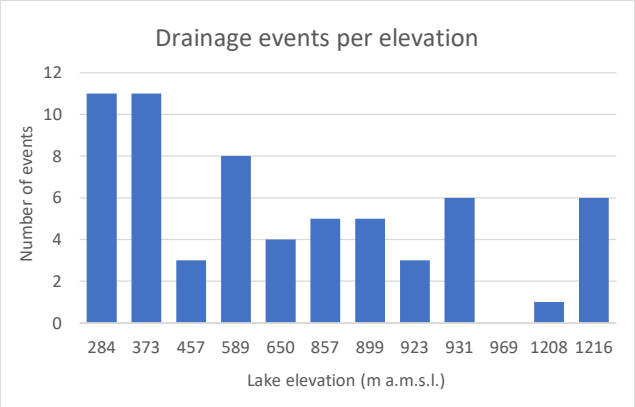

Fig. 37: Number of drainage events detected per lake elevation above mean sea level. Each elevation corresponds to one of the lakes 'lk1' to 'lk12'.

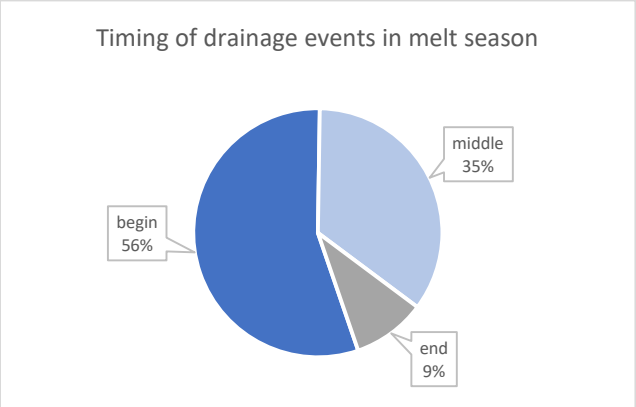

Fig. 38: Percent of detected drainage events per period in the melt season. 'Begin', 'middle', and 'end' refer to the 3 thirds of the melt season as defined by Positive Degree Days (PDD).

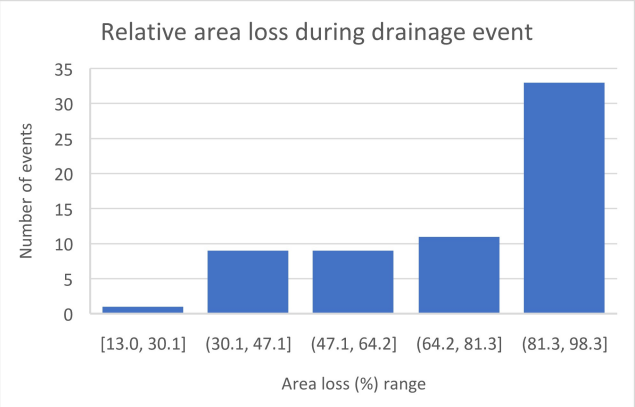

Fig. 39: Number of drainage events for 5 different ranges of relative lake area loss. The minimum area loss is 13%, and the maximum is 98.3%.

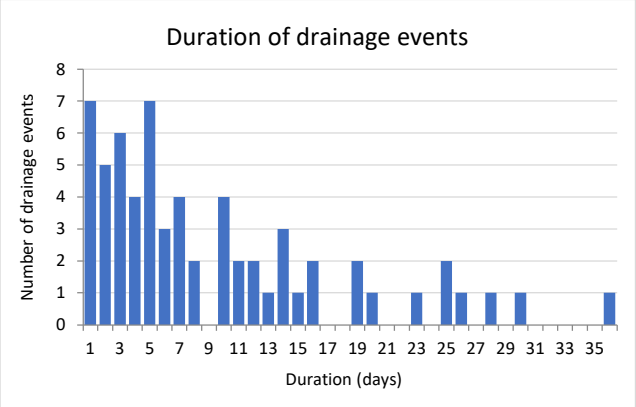

Fig. 40: Histogram of the duration of detected lake drainage events between 2016 and 2022, for the selected 12 lakes.

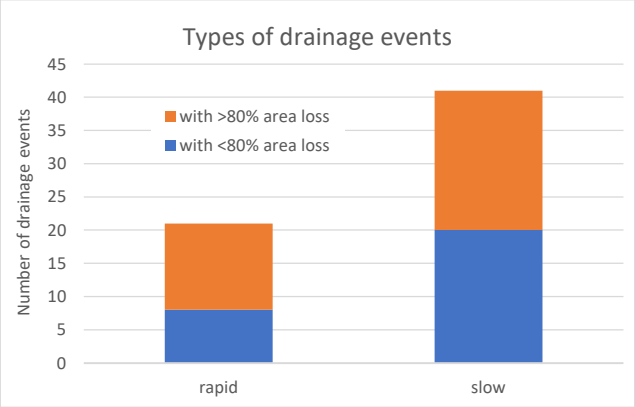

Fig. 41: Types of lake drainage events categorized by duration and relative area loss. Rapid drainage events have a duration of 4 or less days.

Lakes 'lk1', 'lk2', 'lk3', and 'lk11', positioned on the fast-moving ice, exhibit frequent drainage patterns. These drainages predominantly occur slowly, with area losses ranging from 13% to 88.4%. However, instances of rapid drainage are also observed in these lakes, with area reductions varying from 46.9% to 96.6%. These four lakes are situated at lower altitudes, between 284 to 589 meters above mean sea level (a.m.s.l.), and are among the smallest in this study, with their maximum areas ranging from 0.21 square kilometers to 0.49 square kilometers. In contrast, lakes 'lk4' and 'lk5', which have larger areas (1.44 and 1.86 square kilometers respectively), and are located close to each other at similar altitudes (857 and 923 meters a.m.s.l.), display different drainage behavior. These lakes primarily experience large and rapid drainage events, typically not more than once per year. The remaining lakes in the study predominantly drain slowly, occurring between 0 and 1 time per year, with an average area loss of 82.4%. Notably, lake 'lk7' does not exhibit any drainage event

over the seven years, though it frequently gets covered by ice towards the end of the season, a behavior also observed in lakes 'lk8' and 'lk9'. Additionally, lake 'lk6', located in the northern part of the study area, experienced a contamination event in August 2020, detailed in Fig. 55 in Section 3.6. The average values for each of the 12 lakes are summarized in Table 4.

Table 4: Details of lakes 'lk1' to 'lk12', as well as average values for drainage events at each lake. Lakes located on the fast-moving ice are marked with an arrow (→), and lakes for which at least one icing event was detected are marked with a star (*).

Lake	Elevation (m a.m.s.l.)	Max area (km²)	Drainages	Avg area loss %	Avg duration (days)	
lk1	373	0.80	11	74.1	8.5	→
lk2	457	0.44	3	48.5	8.7	→
lk3	589	0.49	8	68.8	7.8	→
lk4	857	1.44	5	94.4	1.6	
lk5	923	1.86	3	96.0	4.3	
lk6	650	1.52	4	79.5	13.5	
lk7	969	3.59	0	-	-	*
lk8	1208	1.99	1	69.5	3.0	*
lk9	1216	1.76	6	90.3	17.2	*
lk10	931	0.48	6	74.4	14.7	
lk11	284	0.21	11	47.5	8.1	→
lk12	899	0.94	5	87.4	9.6	
Average	779.7	1.29	5.25			
Total			63			

Cascading drainage events

To facilitate the analysis of cascading lake drainage events, the positions of the lakes are marked on the image provided by MacKie et al. (2021), which illustrates potential subglacial water flow paths. In Fig. 42, derived from this image, it becomes evident that beneath each of the 12 lakes analyzed, there exists a subglacial water path either leading to another lake or converging towards the main glacier ice stream. The latter is prominently depicted in the center of the image as the primary conduit for subglacial water flow. The least conspicuous and somewhat less apparent of these paths originates from lake 'lk6'. Further verification using the Digital Elevation Model (DEM) indicates that water discharged from lake 'lk6' flows towards the far northern part of the calving front. Consequently, this water does not merge into the main subglacial flow path that underlies the fast-moving ice.

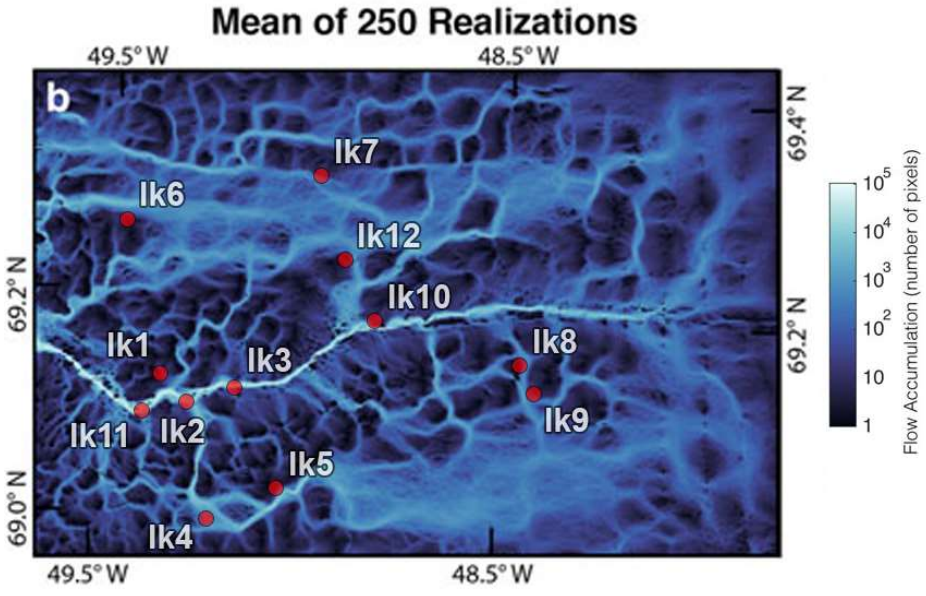

Fig. 42: Mean flow accumulation values across 250 simulations performed by MacKie et al. (2021) to find the subglacial flow paths at the SKK glacier (image modified without altering the shown result). Lake locations are marked by the red dots, labeled with the lake IDs.

Potential cascading drainage events are visually summarized in Fig. 43. This figure features bars that represent the absolute area loss in square kilometers for each lake, with the colors of the bars denoting the dates of the detected drainage events. In total, 8 drainage events are identified that could potentially lead to subsequent drainage events in lower-lying lakes. Among these suspected trigger events, some are rapid drainages, as observed in lakes 'lk4', 'lk5', and 'lk1', while others are categorized as slow drainages. In the majority of these cases, the area of water drained from the higher-elevation lake is larger than the area drained from the subsequently affected lower-elevation lake.

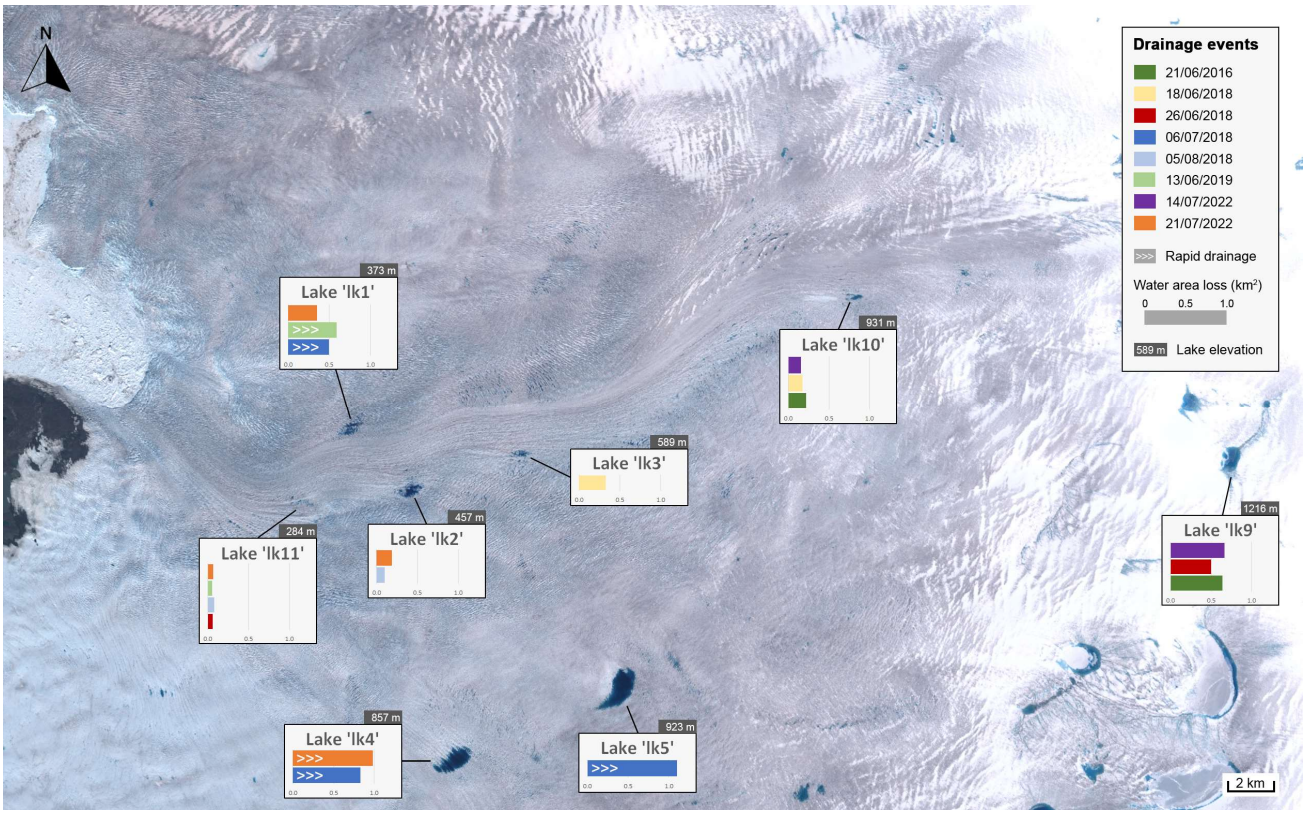

Fig. 43: Potential cascading drainage events with a true-color Sentinel-2 background image from July 17th, 2021, showing lake positions. Bars indicate each lake's absolute area loss in square kilometers, color-coded by the date of the drainage event. The lake elevation above mean sea level is marked in the dark boxes. Rapid drainage events are identified for lakes 'lk1', 'lk4' and 'lk5'.

Algorithm performance evaluation

To evaluate the accuracy of the semi-automatic algorithm used for calculating the lake areas over time, a manual verification process is undertaken using the same Sentinel-2 imagery. The algorithm's performance is evaluated after manually cleansing the dataset of potential inaccuracies in lake area calculations. For this accuracy assessment, two distinct lakes are selected: 'lk1', known for its complex shape and location on the fast-moving ice, and 'lk5', recognized for its more rounded shape and position away from the main glacier artery. For each lake, the area is manually traced on every available image within a single season (2020 for 'lk1' and 2017 for 'lk5'). Polygons are manually drawn directly on the RGB Sentinel-2 images, and subsequently, their areas are calculated and compared to the areas determined by the NDWI-based algorithm. The results of the comparison between the manual and the automatic area calculations are shown in Fig. 44 and Fig. 45. In the case of lake 'lk1', which has a maximum extent of 539'900 square meters in 2020 as determined by the automatic calculation, the Root Mean Square Error (RMSE) is found to be 52'204 square meters. The correlation with the manual method, indicated by Pearson's r, was 0.985, and the average deviation is calculated to be 12.3%. This suggests that the algorithm tends to slightly overestimate the area of this lake. Conversely, for lake 'lk5', which reached its maximum extent of 444'000 square meters in 2017, the RMSE is 23'225 square meters, Pearson's r is 0.992, and the average deviation is -14.5%. This indicates a tendency of the algorithm to underestimate the lake areas for 'lk5'. In this comparison, the automatic approach is considered the reference standard due to its more consistent nature.

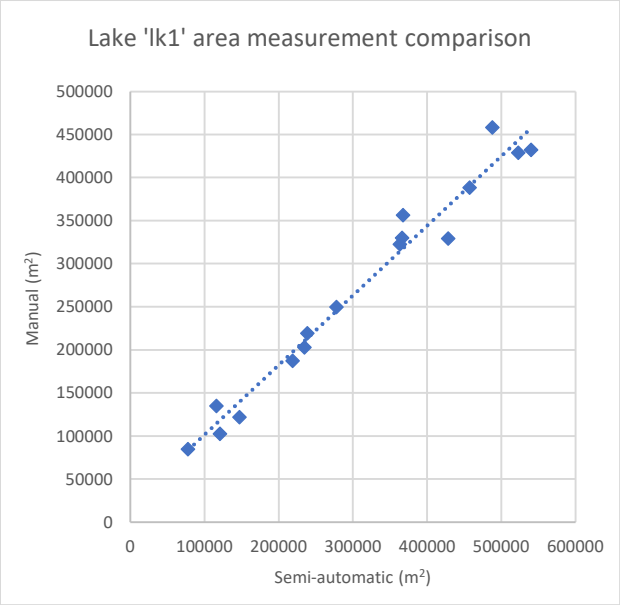

Fig. 44: Comparison of the area calculation using the semi-automatic algorithm versus the manual approach, for a lake with an intricate shape, located on the fast-moving ice. The dotted line shows the fitted linear trend.

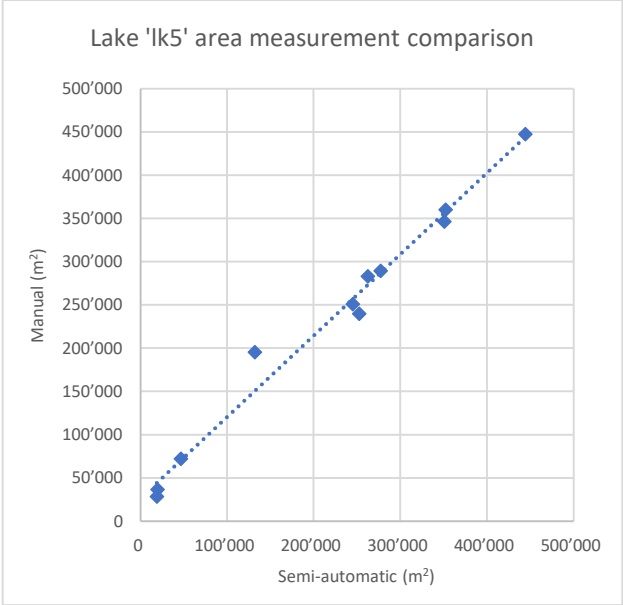

Fig. 45: Comparison of the area calculation using the semi-automatic algorithm versus the manual approach, for a lake with a round shape, located off the main glacier artery. The dotted line shows the fitted linear trend.

3.3 Bed elevation

Longitudinal and lateral transects

The bed elevation of the lower part of the SKK glacier, as well as the location of the three transects across the zone of frequent precursor crevasse appearance, are depicted in Fig. 46. The main fjord in which the glacier lies is about 1 kilometer wide in the deeper part, and reaches a minimum elevation of 1623 meters below sea level. At the same location, the DEM shows an elevation of about 400 meters above sea level, resulting in an ice thickness of about 2 kilometers. In the zone of frequent precursor crevasse appearance, the bed elevation is between 775 and 235 meters below sea level, and the altitude of the glacier surface is about 35 meters above sea level, resulting in an ice thickness between 260 and 810 meters.

Transect 'A', aligned with the ice flow, extends from the southwest to the northeast. The corresponding elevation profile, presented in Fig. 47, delineates a pronounced rise in bed elevation when moving in the direction of the ice. From roughly 700 meters below sea level, it peaks at 462 meters below sea level, before receding to about 650 meters below sea level. Notably, the apex of this elevation is situated centrally within the area where precursor crevasses are predominantly observed, with a gradual slope at the rear and a steeper gradient towards the front, proximate to the calving front.

Transect 'B', oriented perpendicular to the ice flow, stretches from the southwest to the northeast. Illustrated in Fig. 48, this profile exhibits a consistently descending bed slope, starting from about 75 meters above sea level down to 1035 meters below sea level, then ascending to around 250 meters below sea level on the northeastern end. The segment where most precursor crevasses are first detected coincides with the stretch of the glacier bed that demonstrates a continuous, eastern, downward slope.

Transect 'C' is parallel to 'A' and lies outside of the zone of frequent precursor crevasse appearance. The resulting bed elevation profile exhibits a rising profile in the direction of the ice flow, from initially 970 meters below sea level to a maximum of 820 meters below sea level (see Fig. 47). The peak is reached at a later point than for transect one, and is followed by a descent to about 970 meters again.

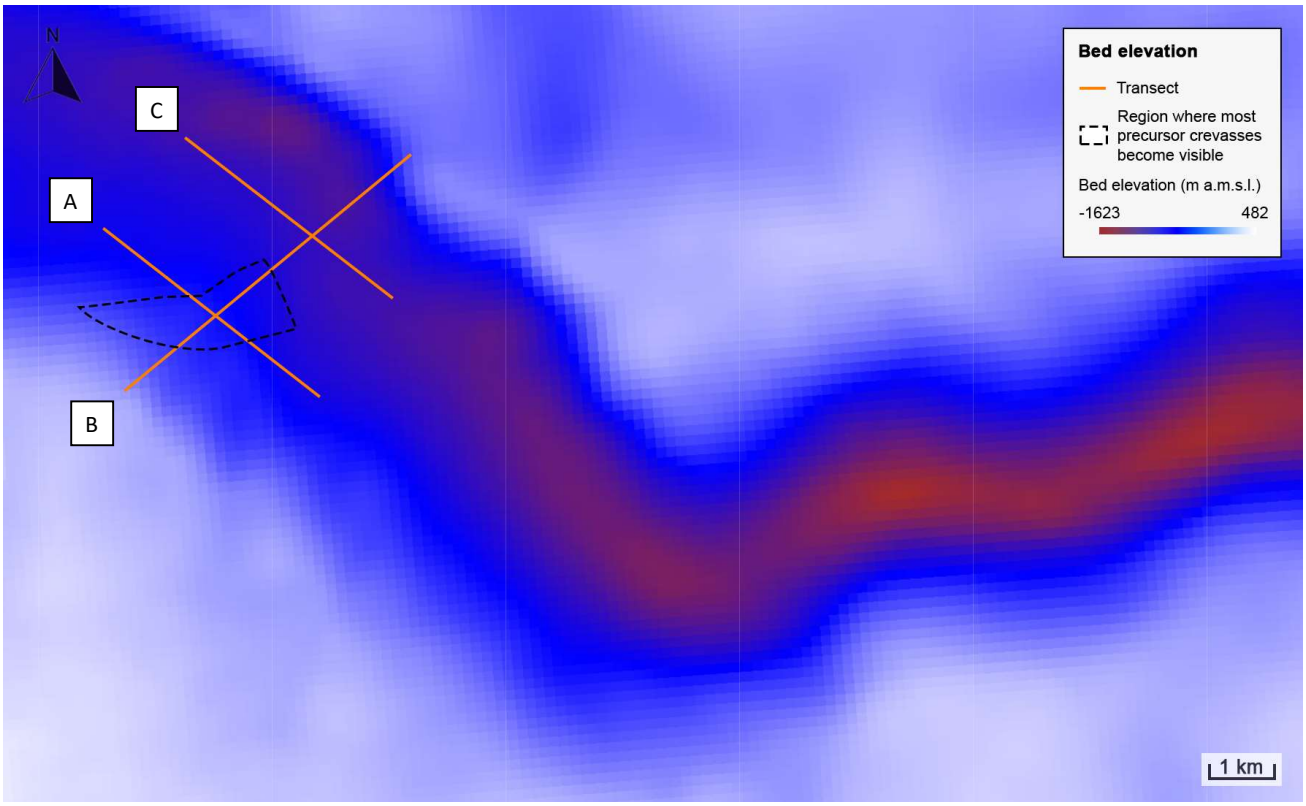

Fig. 46: Lower SKK Glacier Bed Elevation, based on data from An et al. (2017). The glacier's deep flow channel is discernible in reddish hues. The region where most precursor crevasses are initially detected on satellite imagery is outlined with a dashed line, while orange lines indicate the transects utilized to generate bed elevation profiles.

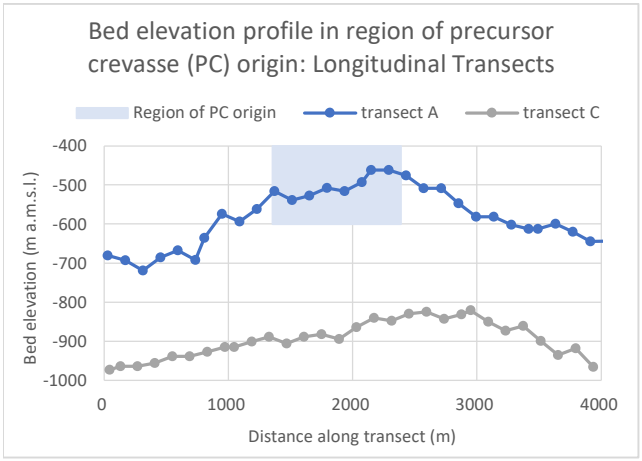

Fig. 47: Bed elevation profile of the SKK glacier in two longitudinal transects- One across the region of frequent precursor crevasse (PC) origin, which is located in the southern part of the glacier terminus, near the calving front. The second is in the northern part of the terminus, outside of this zone. The transects span from the southeast. In the graph, the ice thus flows from left to right.

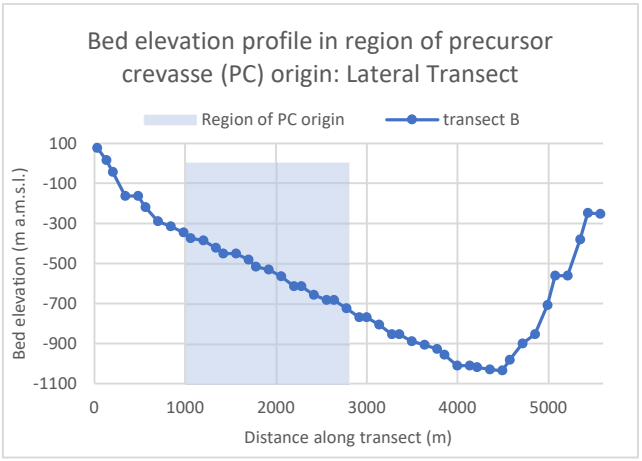

Fig. 48: Bed elevation profile of the SKK glacier in a lateral transect across the region of frequent precursor crevasse (PC) origin, which is located in the southern part of the glacier terminus, near the calving front. The transect spans from the southwest to the northeast, reflecting the glacier bed from left to right when looking in the direction of the ice flow.

3.4 Ice velocity

Evolution of ice velocity at different points

The ice velocity on the SKK glacier varies spatially, primarily as a function of two factors: the distance from the calving front and the distance from the edges of the fjord. Fig. 49 presents an example of the average ice velocities in SKK's terminal zone during the period between May 31st and June 11th, 2019. These velocities are extracted from the MEaSUREs dataset based on an InSAR analysis (Joughin et al. 2021). Additionally, the figure marks three specific fixed points that are chosen for the time series analysis of velocities. The data

reveals that the highest velocities are recorded near the calving front, specifically in the middle of the channel, close to Point 1. Moving upglacier towards Points 2 and 3, there is a consistent decrease in the velocity values.

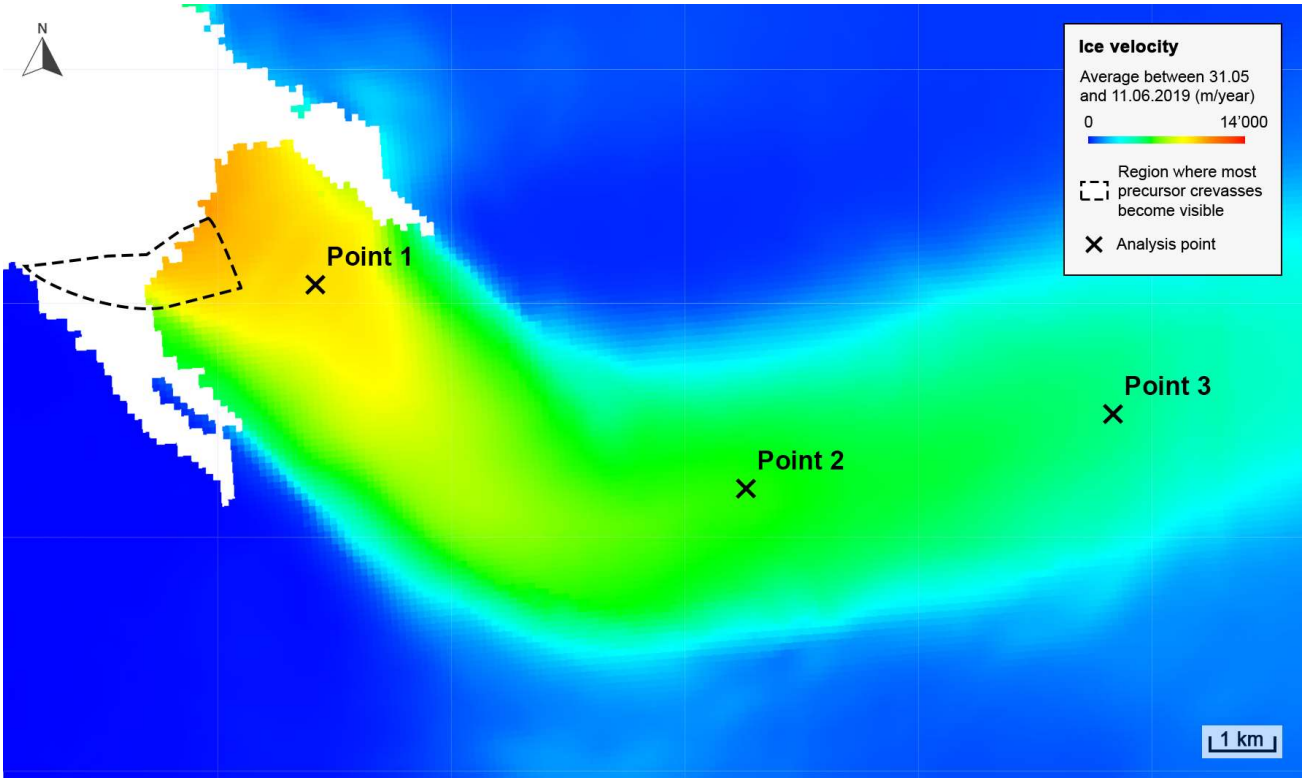

Fig. 49: Ice velocity map of the lower section of the SKK glacier. Values are averages from May 31st to June 11th, 2019, in meters per year, sourced from MEaSUREs data (Joughin et al. 2021). The dotted area represents the zone where most precursor crevasses become discernible, and the crosses mark the three points for the ice velocity time series analysis.

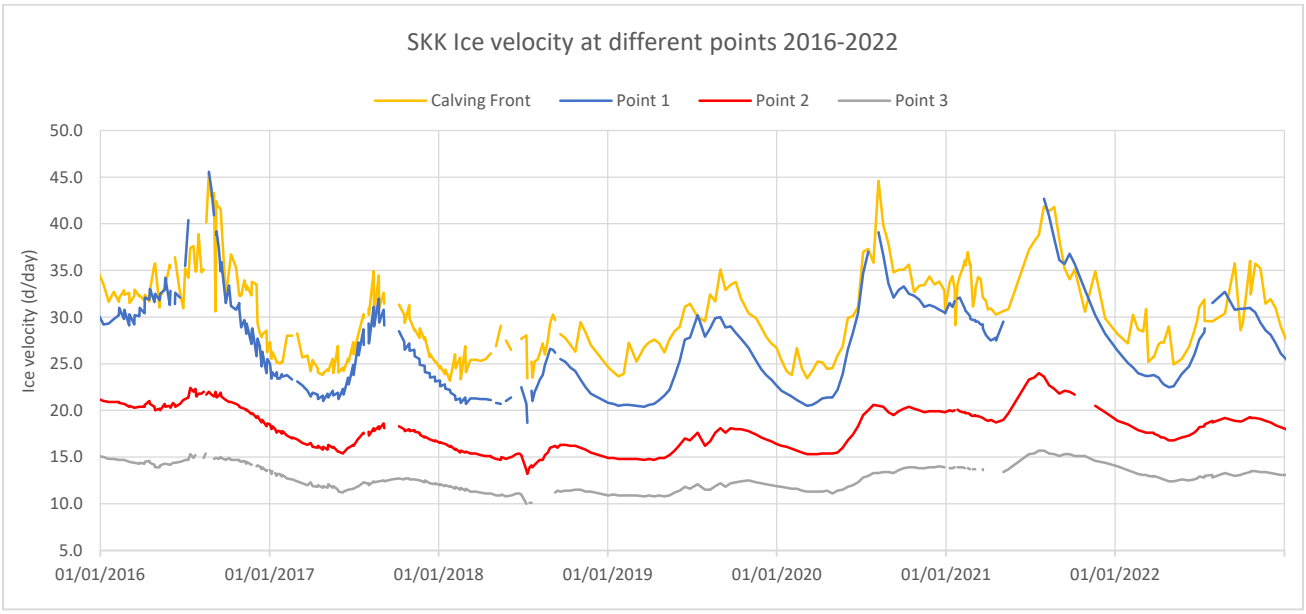

Fig. 50: Ice velocities of the SKK Glacier measured at three different points (1 to 3), as well as just behind the calving front, with data based on MEaSUREs data (Joughin et al. 2021). *Interrupted lines indicate missing data at those locations.*

The ice velocity at a given point on the SKK glacier is not constant, as illustrated in the timeline presented in Fig. 50. This timeline reveals both seasonal and annual trends in velocity, with the degree of fluctuation varying by location. Point 1, located adjacent to the terminus and represented by the blue line in the figure, exhibits the most significant variability and the highest velocities. Velocity peaks in this area surpass 44 meters per day, with marked fluctuations throughout the observed timeframe. At a distance of 8.2 kilometers upglacier, Point 2, indicated by the red line, shows more moderate velocities, typically ranging between 15 and 25 meters

per day. This point also displays less pronounced peaks in comparison to Point 1. Further upglacier by an additional 5.6 kilometers, Point 3, depicted by the grey line, maintains the steadiest and lowest velocities, predominantly remaining below 15 meters per day. The velocity near the calving front, measured between 200 and 300 meters behind the rupture line and shown by the yellow line, is slightly higher than at Point 1 but follows a very similar pattern of fluctuation. However, the velocity just behind the calving front exhibits larger and more frequent short-term fluctuations. The figure shows discontinuities in the lines, indicating periods of missing data. Notably, the blue line representing Point 1 has a significant data gap during the summer of 2021, as evident in the timeline.

Ice velocity and supraglacial lakes

Ice velocity and lake filling on the SKK glacier exhibit different seasonal patterns. The years 2016, 2020, and 2021 feature the highest velocities, yet during these years, few of the lakes reach their largest extents, and no single lake displays a consistent pattern with the ice velocity. Most lakes achieve their maximum yearly extent before the point when the glacier's maximum yearly velocity is recorded, which typically occurs towards the end of the melt season, as indicated by high Positive Degree Days (PDD) values. Fig. 51, which focuses on lake 'lk1', exemplifies this trend. It shows the lake area and the ice velocity at the glacier front, thereby illustrating the differing temporal dynamics between lake filling and ice movement.

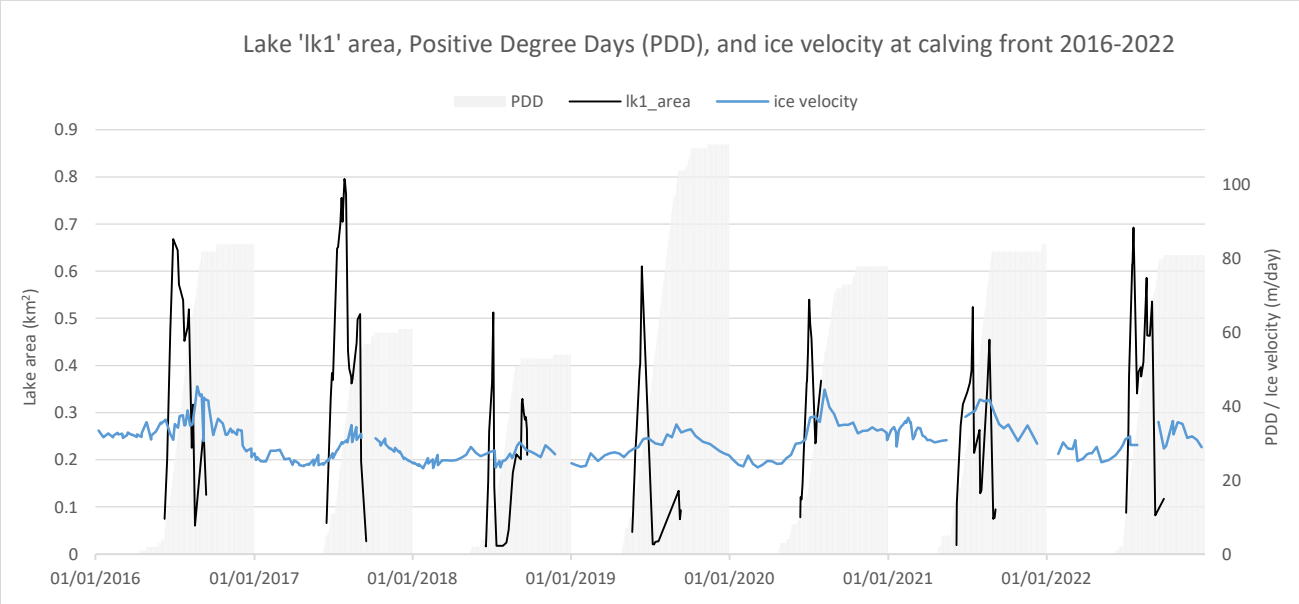

Fig. 51: Evolution of the lake 'lk1' area (black line), the Positive Degree Days (PDD) (shaded grey), as well as the ice velocity at the calving front of the SKK glacier (blue line, from MEaSUREs data by Joughin et al. (2021)), from 2016 to 2022.

Fig. 52 presents a composite view that superimposes the drained lake area, ice velocity near the calving front, and Positive Degree Days (PDD). This comprehensive depiction reveals that the number and magnitude of lake drainage events have a distinct seasonal pattern primarily concentrated in the summer months. Correspondingly, as the melt season commences, marked by increasing PDD values, both the frequency and scale of drainage events escalate. This period also aligns with an increase in ice velocity. Conversely, towards the end of summer, drainage events are more rare and ice velocity diminishes. The data illustrates that, in several instances, the peaks in ice velocity coincide with the onset of major drainage events. However, 2018 emerges as an anomaly, displaying a sudden drop in ice velocity midway through the summer, followed by a rise to the year's maximum velocity. This drop in velocity coincides with a large lake drainage event, involving an area of 2.43 square kilometers. In other instances where a large drainage event is followed by a drop in ice velocity (e.g. in August 2020 and 2021), there is no subsequent increase in velocity. Years with high PDD values (2016, 2019) do not display a significant difference in the amount and magnitude of drainage events. The peak ice flow velocities at the calving front, reaching 42-45 meters per day, are recorded in 2016, 2020, and 2021. These years also correspond to high PDD values (exceeding 75 days). In contrast, the year 2019 has a high PDD value of 111, but a relatively low peak ice velocity of 35 meters/day.

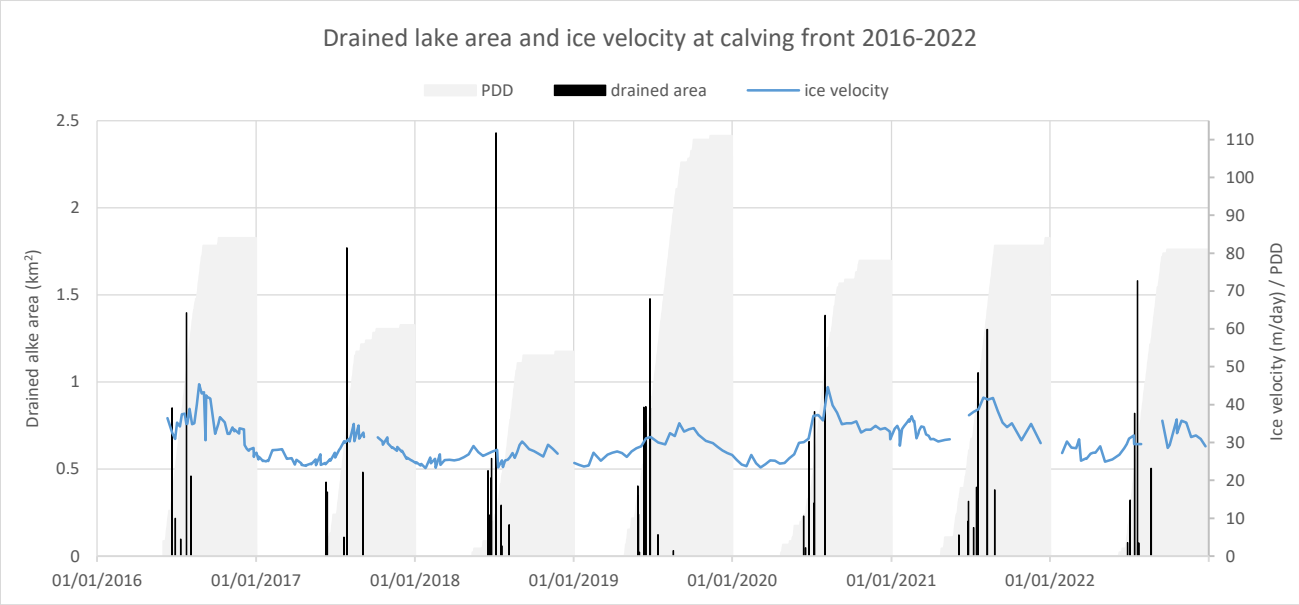

Fig. 52: Drained lake area, represented by black bars sized according to the area loss in km², the ice velocity at the calving front of the SKK glacier (blue line), sourced from MEaSUREs data (Joughin et al. 2021), and the calculated Positive Degree days (PDD) at 780 meters a.m.s.l. based on data from Ilulissat Airport (Drost Jensen 2023). For days with multiple, cascading drainage events, the total drained area is shown on the graph.

3.5 Calving and lake drainage events

Timeline of events

To facilitate a more comprehensive comparison of the timings of calving and drainage events, both are plotted on the same chart, which also includes the ice velocity at the calving front. Periods of cloudiness over the glacier are represented by vertical grey bars in the chart, each indicating a four-day period during which cloud cover remains steadily above 20%. As depicted in Fig. 53, the majority of detected calving and drainage events occur in the first half of the melt season. Both types of events, which vary significantly in size, are typically followed by an increase in seasonal ice velocity.

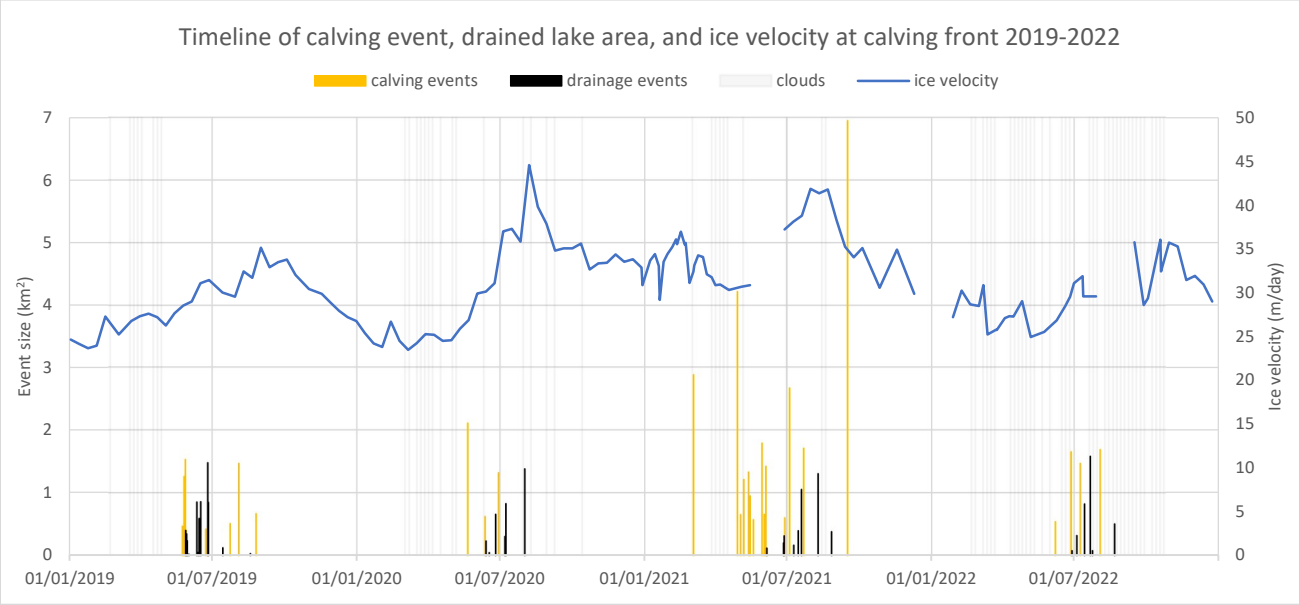

Fig. 53: Timeline of calving events (yellow bars) and lake drainage events (black bars) from 2019 to 2022. The blue line indicates the ice velocity at the calving front, with gaps due to missing data. Grey bars denote periods with over 20% cloud cover for four consecutive days. Event detection is based on Sentinel-2 optical satellite data (ESA 2015), which is missing during the winter months due to the sun's position. Ice velocity is based on SAR data (Joughin et al. 2021).

For drainage events, the range of areas drained from the lakes shows less variation across different seasons, with similar peak values being reached in all years. In contrast, the calving events of the 2021 season are

marked by significantly larger calved areas and a higher frequency of events compared to other seasons. The cloud cover is particularly dense in 2020 and 2022. Notably, the years 2020 and 2021 experienced the highest ice velocities, including unusually elevated velocities even during the winter between these two years.

Concurrent calving and drainage events

In this study, some calving events are observed to occur within a few days of significant lake drainage events. Among the events analyzed, 7 lake drainage occurrences have a plausible association with subsequent calving events. The relevant lakes, namely 'lk3', 'lk4', 'lk6', and 'lk12', are distributed around the glacier, with subglacial water paths leading to the calving front ranging from 10.5 to 35.6 kilometers in length. However, one event pair is excluded from consideration because the estimated subglacial water path leads to the far northern part of the calving front, whereas the associated calving event occurred in the middle region of the terminus. In one instance, a single drainage event is linked to two consecutive calving events. The 7 identified combinations of events feature lake area losses ranging from 0.23 to 1.07 square kilometers and calved areas between 0.4 and 2.79 square kilometers. It is important to note that there is no apparent correlation between the volume of water drained from the lakes and the area of ice calved. These event pairs are detected across all four years analyzed in the study. Additionally, one of these events is also listed in the table of calving events associated with ice velocity speedup (see Table 3). The calculated speeds of subglacial water flow for these events vary from 0.02 to 0.41 meters per second. All plausible combinations of these drainage and calving events are summarized in Table 5.

Table 5: Lake drainage events followed by calving events at a location in proximity to the estimated subglacial water flow path. The column 'PC' indicates at which location on the glacier terminus the precursor crevasse, associated with the calving event, is located (fn = far north, n = north, m = middle, s = south). Drainage and calving dates are estimated, and so is the water flow speed. Positive Degree Days (PDD) are calculated at 780 m a.m.s.l.

Lake	Drainage date	Duration (days)	Area loss (m^2)	PDD	Calving date	Calved area (km^2)	PC	Water speed (m/s)
lk3	28/05/2019	2	402700	16	28/05/2019	2.79	m	n/a
					29/05/2019	0.4	-	0.20
lk12	25/06/2020	2	657800	15	29/06/2020	1.32	m	0.10
lk3	26/06/2021	1	200000	24	28/06/2021	0.6	n	0.10
lk12	27/06/2021	5	314500	20	28/06/2021	0.6	n	0.41
lk4	19/07/2021	1	1052200	43	22/07/2021	1.71	s	0.09
lk12	04/07/2022	10	321300	12	09/07/2022	1.47	fn	0.08
lk6	04/07/2022	5	232200	12	09/07/2022	1.47	fn	0.02

3.6 Additional results

Icing and contamination events

Throughout the period of analysis of supraglacial lake areas, 12 icing events are identified, during the manual verification process of drainage events. Of these, five events are detected for both 'lk7' and 'lk8', and one event each for 'lk9' and 'lk6'. Fig. 54 illustrates one such icing event at lake 'lk9', accompanied by visible snowfall. The lakes involved in these icing events are situated at altitudes ranging from 650 to 1216 meters above sea level. Four of these events take place during the melt season, while the rest coincide with the end of the summer period. Specifically, freezing of lake 'lk7' is observed at the end of the years 2016, 2018, and 2020. Lake 'lk8' experiences freezing events at the end of 2017, 2020, and 2022. Additionally, lake 'lk6' has an icing event at the end of 2020.

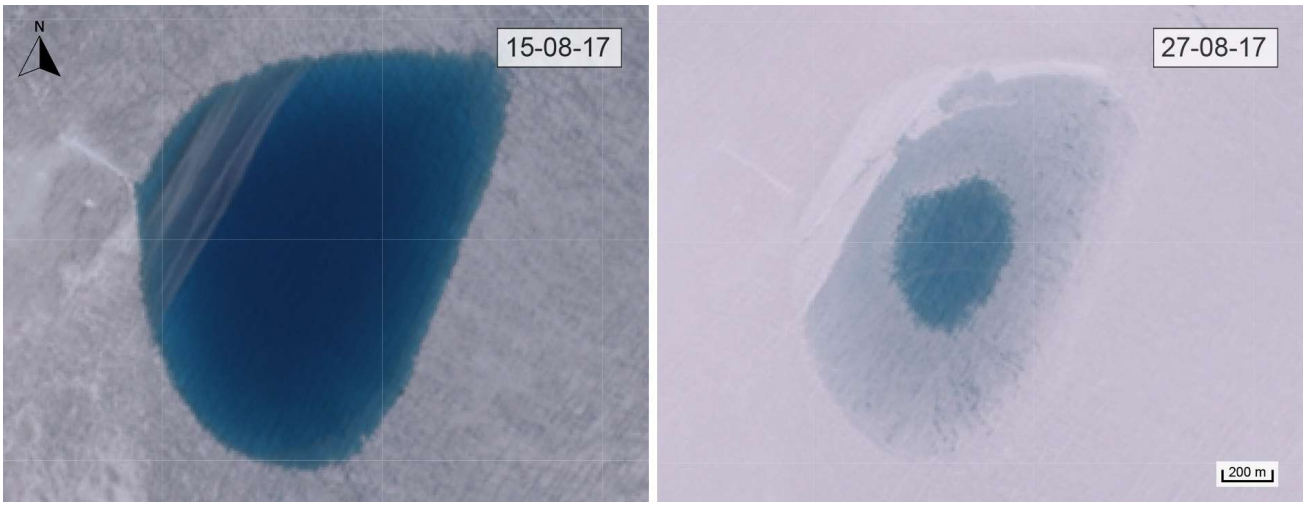

Fig. 54: Icing event at lake 'lk9'. In the left image, taken on August 15th, 2017, the lake is completely free of ice. In the right image, taken 12 days later, the lake's surface is partially frozen and the surroundings are covered with fresh snow.

An unusual phenomenon is observed at lake 'lk6', beginning on August 11th, 2020. A contaminant begins to cover the surface of the lake, starting from the northeast and gradually expanding, mixing through a portion of the lake. This contamination remains visible on the imagery for approximately 10 days before it can no longer be detected. Roughly two weeks after the contaminant dissipates, the surface of the lake begins to freeze, an event that follows a snowfall.

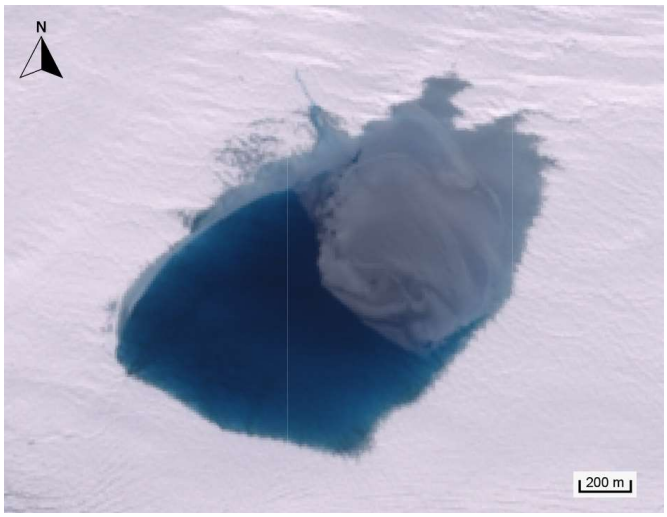

Fig. 55: Lake 'lk6' on August 14th, 2020. The northeastern part of the lake surface is covered by a brighter contaminant.

4 Discussion

4.1 Interpretation of results

Calving events and trends

One main objective of this study is to examine the role of crevasses in calving events, specifically assessing whether ruptures predominantly occur along pre-existing crevasses. Additionally, this research involves a multi-year analysis of the water areas of supraglacial lakes to investigate the potential relationship between lake drainage and accelerated glacier movement. Moreover, the possibility of a connection between accelerated ice flow and subsequent calving events is explored.

As anticipated, this study reveals a dynamic interplay between crevasse development, supraglacial lake formation, and calving events at the Semeq Kujalleq (SKK) glacier. Temperature data, ice flow velocities, and bed elevation measurements are utilized to deepen the understanding of these processes. The analyzed calving events, which vary in size, location, and characteristics of precursor crevasses, as well as their timing within the melt season, form a comprehensive dataset. While the calving front shows a slight recession from 2019 to 2022, other variables do not exhibit any distinct trends during this period. The size of the calved areas indicates a slight upward trend, but this finding is not definitive due to the manual selection of calving events and potential under-detection caused by the limited availability of cloud-free satellite imagery. The increased frequency of detected events in 2019 and 2021 may correlate with the better availability of cloud-free images, yet it remains unclear whether these years actually experienced more calving events.

A significant observation is that most calving events occur at low Positive Degree Day (PDD) values, therefore at the beginning of the melt season. As temperatures rise, melting intensifies, leading to increased surface meltwater production that eventually infiltrates crevasses or enters a moulin, allowing it to reach the glacier bed (Hoffman et al. 2018). Supraglacial water entering the glacier weakens the ice and increases water pressure at the bed, thereby enhancing basal sliding (Lampkin et al. 2020; Williamson et al. 2018). This process not only increases stress and strain within the glacier but also accelerates ice flow (Andrews et al. 2015; Williamson et al. 2018). The combination of these factors significantly heightens the likelihood of calving (Benn et al. 2007). In contrast, fewer calving events later in the melt season could be attributed to the glacier reaching a temporary equilibrium in its structural integrity as it adapts to seasonal changes. Ongoing melting might have a reduced impact on the glacier's overall stress as moulins and a more developed subglacial hydrological system effectively drain the meltwater, thereby decreasing the ice flow velocity and the likelihood of large calving events (Benn et al. 2007; Koziol & Arnold 2018; Lampkin et al. 2020).

The size of calving events shows no clear trend or correlation with PDD, suggesting that factors beyond meltwater, such as lake drainage events, the temperature of the seawater at the calving front, and the presence of ice mélange play more important roles (Amundson et al. 2010; Motyka et al. 2011). The largest analyzed calving event was recorded at the end of the 2021 melt season and likely was a multi-stage event, where an initial ice break-off induces subsequent destabilization through an increase in buoyant forces at the ice-bed interface, triggering a larger calving event (Trevers et al. 2019). The general shape of the newly created calving front is quite consistent across all recorded positions in the fjord, typically presenting a smooth, U-shaped line. This shape is attributed to the higher calving rate in the middle part of the glacier, which is probably a consequence of the higher flow speeds in this area. Only a few events feature calving fronts with sharp edges or small, bite-like missing pieces, contrasting with the more common U-shaped pattern.

Precursor crevasses

In this study, it is observed that many calving events partially ruptured along pre-existing crevasses. This conclusion is drawn with high certainty as the shape of precursor crevasses closely resembles the calving front in images captured immediately after the events. However, in all instances of calving, a significant portion of the ice break-off does not align with previously visible crevasses. This discrepancy might be attributed to rapid fracture propagation shortly before or during the calving event (Benn et al. 2007), which can not be resolved in the satellite imagery due to insufficient temporal resolution, but enables calving of a large area. In such cases, a precursor crevasse is visible along part of the post-event calving front a few days before the event,

while large sections of the rupture line form later and thus remain unresolved on the satellite imagery. Such observations underscore that additional mechanisms and forces are at play in the calving process (Benn et al. 2007). Given the impracticality of observing all calving events in real time, it is hard to conclusively determine the exact behavior of the glacier during these events. For instance, determining which part of the glacier breaks off first and the time elapsed until the formation of the new calving front, as seen in post-event satellite imagery, is challenging. However, it is hypothesized that for events with clearly discernible precursor crevasses, the rupture likely commences along these crevasses and propagates along the calving front until reaching a more stable ice section, which resists further lateral propagation.

The analysis reveals that the majority of detected precursor crevasses associated with significant calving events first appear in satellite imagery in the southern and middle parts of the terminal zone of the SKK glacier (see Fig. 27 and Fig. 29). Moreover, for calving events resulting in a front position between 2550 and 3185 meters, precursor crevasses originate exclusively in this same area, as seen in Fig. 28. These findings are noteworthy, prompting further investigation into potential causes, including the roles of ice velocity and bed elevation.

Ice velocity was initially suspected to be a key factor due to its close relationship with crevasse formation. Typically, faster ice flow heightens stress and strain on the glacier, leading to more intense crevasse formation, particularly in areas where the flow rate changes (Colgan et al. 2016). However, upon analyzing ice flow velocity maps of the SKK glacier's terminal zone (see Fig. 49), this theory is not confirmed. Despite the frequent discovery of precursor crevasses in a high-velocity area near the calving front, the velocities do not significantly differ from those in the northern part of the terminal zone, where fewer precursor crevasses are found. Additionally, within the region where precursor crevasses were frequently discovered, some parts exhibit lower flow velocities compared to others. Therefore, the clustering of precursor crevasses in the southern and middle parts of the terminal zone cannot be solely attributed to increased ice flow velocity.

A more compelling explanation for the increased concentration of precursor crevasses in the southern part of the glacier's lower end lies in the asymmetric topography of the glacier bed. As depicted in Fig. 46, the bed elevation in the zone of frequently originating precursor crevasses is notably higher than that in the northern edge. This asymmetry in the bed topography causes strong shear stresses, which van Dongen et al. (2019) identified as a key factor in the formation of large crevasses. The longitudinal transect across this zone (Fig. 47) shows a distinct bulge peaking within it. It is observed that most precursor crevasses become significant for calving events precisely atop this bulge. This phenomenon could be attributed to the rise in elevation forcing the flowing glacier ice upwards, and as it descends on the other side, the ice fractures due to the change in vertical slope angle (Colgan et al. 2016). Such fractures likely evolve into crevasses deeper than those in earlier sections of the glacier. Given their proximity to the calving front, they serve as ideal precursor crevasses. In contrast, the longitudinal profile taken outside the zone of frequent precursor crevasse appearance, specifically on the glacier's right side at a similar distance from the calving front, exhibits a less pronounced bulge and considerably lower bed elevations. The lateral transect (Fig. 48), reveals a much deeper fjord on the north side of the terminal zone of SKK. This results in thicker ice on the right side of the glacier, which is less influenced by the minor bulge on that side. Where the glacier is thinner, an upward bulge in the bedrock exerts a stronger bending effect, leading to higher tension and thus the formation of deep crevasses in the relatively thin ice. These deeper crevasses are more likely to define the rupture line for a calving event due to the reduced resistance from the ice underneath. Additionally, the bulge is more pronounced on the south side, meaning that slope changes occur more abruptly, resulting in higher strain rates and facilitating the formation of crevasses (Berg & Bassis 2022; Colgan et al. 2016).

The specific concentration of precursor crevasses in the southern and central zones for calving front positions ranging between 2550 and 3185 meters from the zero-point (see Fig. 28), as opposed to the diverse origins of crevasses associated with calving events at other termini locations, raises intriguing questions. A likely factor is the bulge in bed elevation at this specific position, which seems to contribute to an increased number of precursor crevasses, thereby causing calving at the noted position. In contrast, for termini situated at other distances from the zero-point (refer to Appendix I), the bed topography's bulge is either not optimally positioned or extends into the sea, leading to less pronounced clustering of precursor crevasses. Notably, the

distance group '2' exhibits a greater frequency of calving events compared to other locations, which is presumably attributable to the same variation in bed elevation. Moreover, frequent calving events at these distances from the zero point may be partially influenced by retrograde bed elevation, which promotes faster glacier retreat through marine ice sheet instability (An et al. 2017). However, the alignment of the resulting calving fronts with the peak of the bed elevation bulge suggests that increased calving at this location is not predominantly due to the retrograde nature of the glacier bed.

In a further analysis of upglacier conditions, it is noticeable that the zone of frequent precursor crevasse appearance lies in one of the longitudinal bands of the SKK glacier which is heavily crevassed. Tracing back the path of the ice, prior to the location where precursor crevasses become discernible, reveals a potential connection to supraglacial lakes, as shown in Fig. 56. This is exemplified by the behavior of lake 'lk11', which undergoes multiple cycles of drainage and refilling within a single season. The recurrent dynamics of lake 'lk11' suggest that existing smaller crevasses are filled with water, which causes their expansion and deepening (Stevens et al. 2015). Moreover, when the water from the lake drains, conduits through the ice that allow surface meltwater to descend to the bed are formed or reactivated (Lampkin et al. 2020). This process potentially modulates the subglacial water supply, impacting the glacier's basal dynamics (Andrews et al. 2015). Consequently, these alterations in the subglacial hydrological system may influence stress and strain distributions within the ice, fostering crevasse transformation (Colgan et al. 2016). Some of these crevasses, according to the patterns observed, may propagate, increase in size and depth, and lead to calving events (Berg & Bassis 2022; Zarrinderakht et al. 2022). Supporting this hypothesis is the observation that the pattern of crevasses above the lakes differs significantly in form, with the characteristic banded structure becoming particularly pronounced down-glacier of the lakes. This suggests a direct influence of water accumulation in these areas. Supraglacial lakes such as 'lk11', which consist of water-filled crevasses, may thus contribute to the formation of these distinct crevasse bands visible on the SKK glacier's surface.

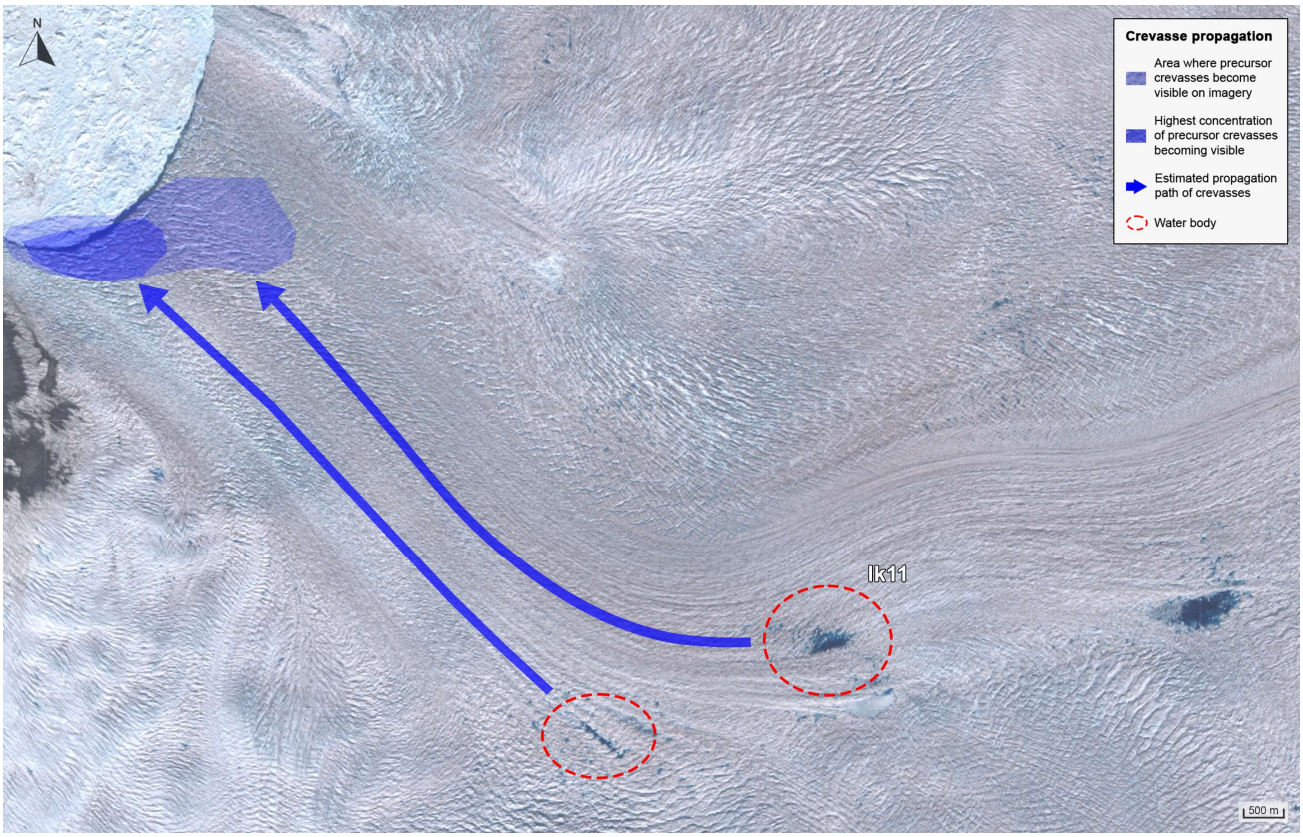

Fig. 56: The main areas where precursor crevasses become visible on optical satellite imagery (blue-shaded areas), and their suspected propagation path before becoming discernable. The origin seems to be located just below an area where water accumulates in the summer months.

The analysis of additional metrics such as average distance from the calving front (see Fig. 30) and propagation speed (see Fig. 31) of precursor crevasses, depending on their geographical location, further differentiates

between those formed in the southern, central, or northern parts of the glacier's terminal zone. The data showing these variations align well with the ice velocity map. In the glacier's central part, where the ice flows fastest, crevasses cover larger distances over a given time. Interestingly, the data indicates that precursor crevasses in the northern part exhibit higher average propagation speeds than those in the middle. This unexpected finding might be explained by limited data availability for this category of precursor crevasses, with some becoming discernible only shortly before reaching the calving front, leading to increased calculation errors due to the short distance and uncertainties in the dating of the calving event.

Another metric, the average appearance time of precursor crevasses (see Fig. 32), requires cautious interpretation as different surface dynamics affect the visibility of crevasses in the imagery. Precursor crevasses in the middle and southern parts of the terminal zone tend to be distinguishable earlier, possibly due to their formation process. It is suspected that these deep crevasses primarily form due to the bulge in the glacier bed elevation and then enlarge with additional meltwater input, in contrast to those in the northern part where the bulge plays a less prominent role. Consequently, the widening and deepening, which enable their recognition on satellite imagery, likely develop later in the northern crevasses.

Regarding the length changes of precursor crevasses during their journey from their initial discernible location to the calving front (see Fig. 33) considerable variation was observed among the events analyzed. Crevasses in the middle of the ice flow tend to increase in length, while those at the edges experienced both shortening and lengthening. This phenomenon might be linked to their differing orientations. Crevasses at the edges, influenced by shear stress from the slower-moving ice, typically have an orientation tilted by 30-45° from the axis normal to the flow direction (see Fig. 56 and Colgan et al. 2016). The tilting of crevasses, combined with the rapid ice flow towards the calving front, can modify their appearance in satellite imagery. This effect is a probable explanation for the noted reductions in crevasse length. Therefore, the recorded changes in crevasse length should be interpreted cautiously.

Evolution of glacier lakes

The analysis of the calculated water surface areas of the studied supraglacial lakes revealed distinct seasonal patterns. The onset of lake filling generally coincides with the start of the melt season, with slight variations among lakes due to differences in altitude and location. However, the yearly maximum size of the lakes does not consistently correlate with the amount of Positive Degree Days (PDD) in a given year. For instance, 2019 was the year with the highest PDD, but only one of the lakes reached its maximum size, while the others exhibited smaller or medium extents. This suggests that lake filling is not solely dependent on the number of melt days. Furthermore, the PDD is calculated at the average altitude of the 12 lakes analyzed in this study. This implies that for lakes situated at higher elevations, there were likely fewer days with melting conditions. Conversely, lakes at lower elevations experience more days with temperatures above freezing and potentially receive more inflow, as they are fed by a larger catchment area, with more melting ice situated above them. However, whether this meltwater accumulates on the surface in a lake or enters the subglacial hydrological system via a moulin remains uncertain. This variability in meltwater pathways underscores the complexity of the hydrological processes at play on the glacier.

Initially in the summer, meltwater begins to fill the lakes up to a certain level. Subsequent drainage events, which open new channels to the subglacial system, alter this process (Morriss et al. 2013). Once these channels form, either through glacier movement creating new cracks, hydrofracture during rapid drainage events, or supraglacial water flow carving new paths and finding connections to the subglacial hydrological system (such as a moulin), the newly melted ice no longer contributes to lake filling in the same manner (Lampkin et al. 2020; Morriss et al. 2013; Williamson et al. 2018). Instead, it drains through the newly formed channels. This leads to the development of a more efficient subglacial drainage system, which can persist for the remainder of the melt season, even with minimal water input (Chandler et al. 2021). The variability of available water flow paths from season to season also plays a significant role in determining where and how much water accumulates (Studinger et al. 2022). It is important to note that this study focuses on a few large lakes on the SKK glacier, yet there are numerous additional water bodies in the vicinity. These surrounding water features potentially influence the overall distribution of water, thereby providing an additional explanation for the observed seasonal differences in lake behavior and extent.

For lakes situated at higher altitudes, which regularly experience icing at the end of the season, the remaining undrained water of one year may affect the size of the following year. The phenomenon was described by Lampkin et al. (2020) as buried lakes and occurs when a fast icing event covers the lake surface, immediately followed by rapid snow accumulation to provide thermal insulation. This process is common for lakes situated at high altitudes, and the amount of liquid water retained depends on the initial volume and the atmospheric conditions during winter. Deeper lakes have larger thermal inertia and are therefore more prone to retain liquid water under the snow and ice cover (Lampkin et al. 2020). In this study, it is observed that several lakes still contain water at the end of the melt season. However, in some instances, the availability of data is hindered by cloud cover, creating uncertainty as to whether the water drained or was covered by ice. In cases where lake icing is visually confirmed through satellite imagery analysis, concurrent snowfall events are often identified as well. It is plausible that lakes at higher altitudes, like lake 'lk7', 'lk8', and 'lk9', were buried under snow while still containing liquid water. Consequently, in the subsequent melt season, these lakes would have an initial advantage with a pre-existing quantity of water remaining from the previous season. Conversely, it is also conceivable that some lakes never fully thaw during the summer months. This scenario might apply to lake 'lk7', which exhibits alternating patterns of large water extent in some years and significantly reduced extent in others. This variation could suggest that in certain years, the lake remains partially frozen throughout the summer, impacting its open water area and contributing to the observed fluctuations in extent. These factors could account for the observed variability in lake surface area and might even explain why some drainage events occur very early in the melt season. Such nuances in the seasonal behavior of supraglacial lakes highlight the intricate interplay between climatic conditions and glacial hydrology.

Moreover, in this study, it was observed that lakes at higher altitudes are generally larger than those at lower altitudes. This result may be influenced by the manual selection of lakes for analysis. The chosen low-altitude lakes are situated on fast-moving ice, where the dynamic nature of the ice flow results in constantly changing lake basins, and newly formed or enlarged crevasses can quickly fill with water, potentially leading to hydrofracture (Lampkin et al. 2013; Stevens et al. 2015). Additionally, lakes at lower altitudes receive meltwater earlier due to their location in the glacier's catchment area. These dynamic conditions result in frequent draining and filling cycles, restricting these lakes from attaining larger sizes. In contrast, lakes not located directly on the fast-moving ice experience less variation in their basins over time, allowing higher filling levels. The reduced glacier dynamics in these areas lead to less frequent draining events. Consequently, these lakes, due to their relative stability and location away from the most dynamic parts of the glacier, can maintain larger water volumes over extended periods. This distinction in lake behavior based on altitude and location relative to ice dynamics is an important consideration in understanding the hydrological processes of the glacier.

Lake drainage events

Irrespective of their altitude, drainage events in supraglacial lakes predominantly occur at the onset of the melt season and are rare in the final weeks leading up to winter. This observed pattern supports the theory that drainage events typically occur once the lakes accumulate a certain threshold of water volume, which can exert a pressure high enough to cause hydrofracture of crevasses underneath, allowing the lake to drain (Stevens et al. 2015). By creating new englacial channels, drainage events thereby promote a transformation of the subglacial hydrological system, making it more efficient (Stevens et al. 2022). Consequently, newly formed moulins and the enhanced efficiency impede the lakes from refilling, supporting the idea that these drainage events are key in altering the glacier's subglacial water dynamics (Morriss et al. 2013). Approximately half of the detected drainage events are characterized by a significant area loss, exceeding 80% of the area at the start of the event, suggesting that most drainage likely originates near the lowest point of the lake basin. One third of the events analyzed are rapid drainages, with 13 instances resulting in an area loss of more than 80% in 4 or fewer days. These events are particularly noteworthy and primarily occurred in lakes 'lk4' and 'lk5'. Located approximately 10 kilometers south of the main artery of the SKK glacier, these lakes are relatively large (1.44 square kilometers and 1.86 square kilometers, respectively) and exhibit clear filling and drainage patterns. A rapid drainage event from such sizable lakes releases a substantial volume of water into the subglacial hydrological system. Consequently, these significant drainage events have the potential to influence

other water bodies at lower altitudes and may contribute to a speed-up in glacier flow due to increased basal gliding (Andrews et al. 2015; Hoffman et al. 2018). This underscores the importance of understanding the impacts of such drainage events on the overall glacier dynamics and its hydrological systems.
According to Hoffman et al. (2018), sequential or grouped lake drainages are common, potentially even typical. Their study illustrates various scenarios of cascading events, including those initiated by slow drainage. To assess the plausibility of drainage sequences among the drainage events found in this study, an evaluation is conducted using the Digital Elevation Model (DEM) and the subglacial water routing map by MacKie et al. (2021). The analysis confirmed the plausibility of the detected events, as the lakes involved in these pairings or groupings are likely connected by subglacial water paths. However, it remains unclear whether the drainage of an upper lake directly triggers the drainage of a lower one in a causal manner. Such downstream events could also result from glacier speedup opening new englacial channels, or significant precipitation promoting hydrofracture (Hoffman et al. 2018). Notably, lake 'lk8' does not exhibit drainage responses to events at the nearby lake 'lk9', despite their proximity suggesting a potential connection. The drainages at lake 'lk9' are consistently slow, possibly diminishing any significant impact on adjacent lakes. This slower process involves less forceful water flow and the creation of new, deep crevasses through hydrofracture is less likely, but still possible (Hoffman et al. 2018; Williamson et al. 2018). Consequently, the forces at play are smaller and less likely to affect neighboring water basins. This differential impact of drainage types on surrounding lakes adds another layer of complexity to understanding the interconnected nature of these hydrological systems.

Lake drainage induced glacier speedup

According to previous research, lake drainage events can have short-term effects on glacier ice flow velocity through increased water pressure at the glacier bed, which in turn increases basal sliding (Morriss et al. 2013; Moussavi et al. 2016; Stevens et al. 2022; Williamson et al. 2018). The long-term effects on glacier dynamics are less clear and more difficult to detect, however, it is known that a moulin opened as a consequence of lake drainage, can remain active for several years, delivering water to the glacier bed (Hoffman et al. 2018; Williamson et al. 2018). In this study, the relationship between lake drainage events and ice velocity at the glacier's calving front is analyzed, revealing a cyclical pattern in ice velocity. Peaks in velocity appear to correlate with spikes in drained lake area, or shortly thereafter, suggesting a potential link between these two variables. The ice velocity tends to increase at the same time as the number of lake drainage events and subsequently decreases, indicating a potential seasonal influence or a direct response to these drainage events. However, the extent to which drainage events contribute to seasonal variations in ice acceleration and deceleration remains uncertain. Meltwater is a key factor driving ice acceleration as it enhances basal sliding (Stevens et al. 2022). While drainage events can induce short-term glacier speed-ups, they also facilitate the development of a more efficient subglacial hydrological system (Stevens et al. 2022). This efficiency reduces water pressure at the glacier bed, which in turn reduces the decoupling effect of the ice from the bedrock, consequently decreasing basal sliding. It is this transition to an efficient subglacial drainage system that leads to a decrease in velocities, even though additional meltwater continues to be produced (Stevens et al. 2022). One interesting and unexpected result is the sudden drop in velocity after a series of cascading drainage events on July 6th, 2018 (see Fig. 52, and Fig. 43). In this instance, there is no visible short-term increase in glacier velocity associated with the lake drainages, but only a decrease, followed by a slight increase in the subsequent weeks. The unusual character of this event coincides with the unusual ice velocity pattern in 2018, which does not display a significant peak towards the end of summer and has generally lower speeds compared to other years, possibly attributed to the low PDD. A possible explanation for this occurrence could lie in the short-term character of lake drainage-induced glacier speedups, making it undetectable to the measurements performed by Joughin et al. (2021), which have a relatively low temporal resolution of 11 days. The glacier speedup in the subsequent weeks might in turn be attributed to newly opened moulins during the drainage events, which enable lubrification of the glacier bed through increased water delivery – without reaching an efficient subglacial drainage system yet (Hoffman et al. 2018; Williamson et al. 2018). These observations suggest a complex interplay between short-term impacts of drainage events, like immediate glacier speed-ups, and their long-term effects, such as the establishment of an efficient subglacial drainage system, which ultimately modulates ice flow dynamics.

Notable within the collected data are instances where lake drainage events are followed by calving events shortly thereafter. Such combinations are identified seven times in various locations, both on the fast-moving central ice and along the sides of the glacier. These associated calving events occurred across different sections of the terminus. Such lake drainage events could potentially be responsible, or at least contribute, to the subsequent calving events. The short-term speedup caused by water reaching the glacier bed may escalate stress at the glacier's calving front, leading to the rapid formation and expansion of crevasses, especially near the interface with the ocean (Benn et al. 2017; Zarrinderakht et al. 2022). The buoyant forces from the ocean water on the ice front further intensify these stresses, increasing the likelihood of calving (Trevers et al. 2019). To assess the plausibility of the lake drainage and calving events occurring in sequence, calculated water flow speeds from the lakes to the calving front were compared with existing literature values (Stevens et al. 2022). These comparisons confirmed that the speeds fall within the realistic range for tidewater glaciers. Therefore, it is plausible that these lake drainage events could have initiated the observed calving events, highlighting the interconnected nature of supraglacial lake drainage and calving processes in glacier dynamics.

Calving events and glacier speedup

The dynamics of glacier flow and calving events are intricately linked through a series of feedback mechanisms that affect the stability and movement of the glacier. Faster glacier flow may lead to increased calving as a greater volume of ice is transported to the terminus, where it encounters warm ocean waters that facilitate calving (Benn et al. 2017; Mercenier et al. 2020). Conversely, calving events can induce a short-term speedup of glacier flow (Cassotto et al. 2019; Rückamp et al. 2019). This relationship is partly due to the back stress exerted by the protruding ice at the glacier terminus (Rückamp et al. 2019). When ice blocks are calved from the glacier's terminal zone, this resistance diminishes, resulting in a more rapid flow of the glacier toward its previous terminus position. It is as though the calving events exert a 'pulling' force, accelerating the glacier's descent. However, the causal relationship between glacier speedup and calving is complex. In the events investigated in this study, an interplay between these processes can be observed. Prior to the calving events, a deceleration of ice velocity near the terminus was noted, followed by a medium-term acceleration post-calving. Although this acceleration was slight, it reversed the preceding trend of velocity decrease, which could potentially be attributed to the significant size of the concurrent calving events. The challenge arises in determining the sequence of these events. Due to the temporal resolution of the available velocity data, which is averaged over 11-day periods, and the precision to which calving events can be dated, typically within a few days' margin, it is challenging to determine whether the increase in velocity is a consequence of calving or vice versa. Nonetheless, the likelihood of a correlation between these events is high. In certain cases, there may also be a positive feedback loop, where calving and acceleration mutually reinforce each other, potentially explaining substantial and rapid glacier speedup events. The intricate interplay of forces and responses underlines the complexity of glacial systems and the need for high-resolution temporal data to unravel the sequence and causality of speedup events and calving.

4.2 Methodological considerations

Limitations of the data

The data employed in this research is freely available online, providing a substantial advantage in accelerating the research timeline. Such easy access eliminates the need for labor-intensive in-field measurements and avoids delays associated with requesting on-demand, commercial satellite data. Furthermore, the global availability of Sentinel data facilitates the application of this study's methodologies to the analysis of other glaciers. Google Earth Engine (GEE) enhances this efficiency by offering an extensive range of pre-processed datasets, thereby simplifying the analytical process. However, the reliance solely on freely available and predominantly satellite-based data does introduce certain challenges.

One significant limitation of this study is sourced in the spatial resolution of the satellite data. A pixel size of 10 meters as found in the Sentinel-2 optical imagery bands permits easy recognition of large calving events and large supraglacial lakes – smaller cracks or water bodies, however, are hardly resolved in the images. Precursor crevasses or smaller sections of supraglacial lakes often feature parts with diameters close to the pixel size, making it very challenging to accurately map their shape. Since both the calving and the ice flow are

suspected to be mainly affected by larger features or events, this limitation does only partly interfere with the aim of the study. Images with a smaller pixel size would permit us to analyze events in more detail and with higher certainty. The utilized Sentinel-1 Synthetic aperture radar (SAR) images provided satisfying spatial resolution when recorded in the Interferometric Wide (IW) mode, which was widely available only since 2018. Spatial resolution was low for the bed elevation dataset and the subglacial water flow paths as well. The latter was only available in the form of low-resolution raster images. This format limited the precision with which these subglacial water flow paths could be analyzed and interpreted within the context of this study. Nevertheless, both these datasets provided very valuable information for supporting the interpretation of the results.

A major challenge in remote sensing studies, such as this one, is the availability of usable images. The potential benefits of the Sentinel-2 satellite pair's low revisit time are often offset by cloud cover, which either obscures the view or skews the results of automatic water detection algorithms. To mitigate this issue, images with substantial cloud cover are excluded from the analysis. This exclusion significantly reduces the number of usable images, leading to an increased likelihood of undetected events. Additionally, the lack of Sentinel-2 images at northern latitudes in the winter months results in a 'dark period', during which activities on the glacier remain undetected. Despite this gap in data, it is generally expected that glaciers exhibit reduced activity in this period, a notion supported by the observed lower ice flow speeds during these colder months (see Fig. 50). The low temporal resolution of the images also presents difficulties in precisely dating events, a crucial factor when establishing a sequence of lake drainages and calving events. SAR imagery, which is not affected by cloud cover, offers some improvement in event dating. However, for smaller and more complex supraglacial lakes, like lake 'lk1' (see Fig. 57), SAR images are less effective. In these lakes, which are located in heavily crevassed areas, the water surface is often interrupted by ice, disrupting the radar's backscatter signal and rendering water detection challenging. Consequently, determining which image depicted a larger water surface is difficult, as changes between the before and after-drainage images are too subtle for clear detection in SAR images. The utility of SAR is further limited when only Extra Wide (EW) images are available due to their low spatial resolution. Moreover, as in this study the detection of both calving and drainage events primarily relies on optical data, SAR imagery does not reduce the number of undetected events. Instead, there is a tendency for calving and drainage events to be detected within similar time frames, likely because of the primary use of optical imagery, which is only available on cloud-free days. This limitation is particularly impactful in years with frequent cloud cover, such as 2022. Temporal resolution issues also affect velocity data analyses. More precise ice flow velocity data would be beneficial in accurately sequencing the events, especially when examining the correlation between glacier speedups and drainage or calving events.

Another aspect that presents limitations in this study is the source of temperature data for calculating Positive Degree Days (PDD), which are used as a proxy for the amount of meltwater. PDD are calculated using temperature data from Ilulissat Airport's weather station, situated 29 meters above sea level and approximately 60 kilometers West of the SKK glacier. To better align this data with the conditions of our study area, an altitude correction is applied. Nonetheless, it's important to recognize that weather patterns within a long, narrow fjord-like SKK can vary significantly from coastal conditions. This presents a limitation, as the weather station data is the only continuous dataset available for the entire study period. A comparative analysis with data from Swiss Camp, located on a nearby glacier and thus probably exposed to more similar conditions, indicates that the onset of the melt season is consistently similar each year in both datasets. However, the annual total PDD does not follow a parallel pattern. Consequently, while the timing of the melt season's onset can be considered reliable, conclusions regarding variations in annual meltwater amounts should be approached with caution, due to potential discrepancies in weather patterns between the two locations.

Manual crevasse tracking

The detection of precursor crevasses is conducted manually, a method deemed more suitable for this study, where specific crevasses are investigated. Automatic algorithms, though useful, are complex and require considerable time for proper training. The manual approach, in contrast, is simpler and more direct. However, this method is time-intensive and susceptible to errors from potential misinterpretation of the satellite

images. When mapping crevasses with diameters close to the pixel size of the images, some level of subjective interpretation is inevitable, as features are not always distinctly visible. Consequently, the mapped lines incorporate a certain degree of inaccuracy. To minimize errors, results are meticulously re-checked, which further extends the time required for data analysis. Time is a contributing factor to the limited number of events analyzed over a limited range of years. A notable limitation in the used methodology is the absence of data on crevasse depth, which could have provided additional insights into the nature of precursor crevasses and their influence on calving (Trevers et al. 2019). However, without continuous ultra-high-resolution aerial imagery, such as that from an Unmanned Aerial Vehicle (UAV), measuring crevasse depth is not feasible. Additionally, the lack of such imagery to verify the mapped crevasse shapes adds to the uncertainty. Therefore, while the numerical values derived from this study are indicative, they should be interpreted with caution. Despite these limitations, the manual approach demonstrates consistency and precision in identifying large-scale trends, affirming its utility in glacier dynamics research.

A trip to the glacier would have eased the understanding of the shapes of the crevasses and provided a solid backbone to verify mapped features. Unfortunately, in the scope of this thesis, an expedition to the SKK glacier was not feasible due to its remote location, accessible only by helicopter. While an in-situ verification would have been invaluable, the decision to base the study on freely accessible and globally available remote sensing data presents the advantage of enabling the application of these methods to the study of other glaciers. This approach, despite its limitations, broadens the study's applicability and relevance in glaciological research.

Lake area and drainage detection

The semi-automatic approach employed for calculating the water area of supraglacial lakes offers numerous advantages. It enables the analysis of hundreds of images within seconds and facilitates the direct export of data into tabular format sheets. However, as shown by the manual verification process, the algorithm revealed is more effective during the summer months when the sun's incidence angle is smaller, thus closer to being perpendicular to the surface. In late summer and early fall, clouds are occasionally misidentified as water by the algorithm, leading to erroneous results (see Fig. 20). Additionally, when ice begins to form on the lake surfaces, the algorithm detects a reduced water area, which could be mistakenly interpreted as a slow drainage event unless manually verified in the imagery.

The algorithm's performance varies slightly between lakes situated on fast-moving ice, like lake 'lk1' (as shown in Fig. 57), and those further from the main glacier artery, such as lake 'lk6' (Fig. 58). Lakes on the fast-moving ice exhibit more variability in the results due to several factors. Firstly, their shapes are irregular, following crevasses rather than standard topography. Secondly, their smaller size, close to the sensor's spatial resolution, leads to numerous mixed pixels, significantly impacting results. Adjusting the NDWI threshold or omitting lake area dilation would substantially influence results for these lakes. However, for consistency in comparison, the same algorithm parameters are applied to all lakes. It should be noted, that precise calculation of lake area is not critical for the objectives of this study, which focuses primarily on identifying patterns of lake filling and draining. Consequently, lakes situated on the fast-moving sections of the glacier, like 'lk1', display less distinct filling and draining patterns than lakes situated on the sides. This is likely due to their unique morphology, with multiple small branches influenced by surrounding crevassed areas, as depicted in Fig. 57. These crevasses often divide the lakes into different segments, with many ice blocks emerging from the water. In contrast, lakes near the glacier margins, exemplified by lake 'lk6' (Fig. 58), show clearer filling and draining patterns (see Appendix II). Their more regular, rounded shape allows for more precise automatic area detection, as they generally have fewer mixed pixels.

For more rounded lakes such as 'lk6', the most significant discrepancies are noted when the lakes are smaller. In these instances, the algorithm tends to underestimate the area, which may be due to mixed pixels on the edges, potentially not being detected as water because of the threshold setting. Another contributing factor is that manual delineation becomes more prone to error for smaller features, as the lake size approaches the satellite imagery's pixel resolution. In contrast, the results for more complexly shaped lakes like 'lk1' exhibit less consistent trends, with both underestimations and overestimations at smaller sizes, and predominantly overestimations when the lakes are larger. This can be attributed to several factors. First, the algorithm excludes areas smaller than 10,000 m² to filter out minor streams or water patches, possibly leading to

underestimations when parts of the lake are connected only by narrow channels. Second, to account for missing pixels at the edges and center, the algorithm expands the detected lake surface by one pixel (about 10 meters) in all directions, potentially causing overestimations, especially for small total areas. Third, manually tracing the perimeter of an intricately shaped lake is inherently challenging, especially when the image's spatial resolution matches the width of the lake's smaller channels.

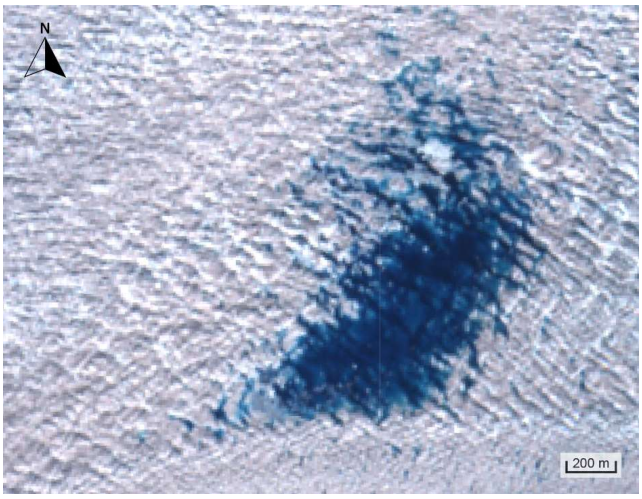

Fig. 57: Lake 'lk1', situated on the main glacier artery within fast-moving, crevassed ice, has an irregular shape with many emerging ice blocks. This complicates automatic lake area detection, as mixed pixels hinder distinguishing water from ice.

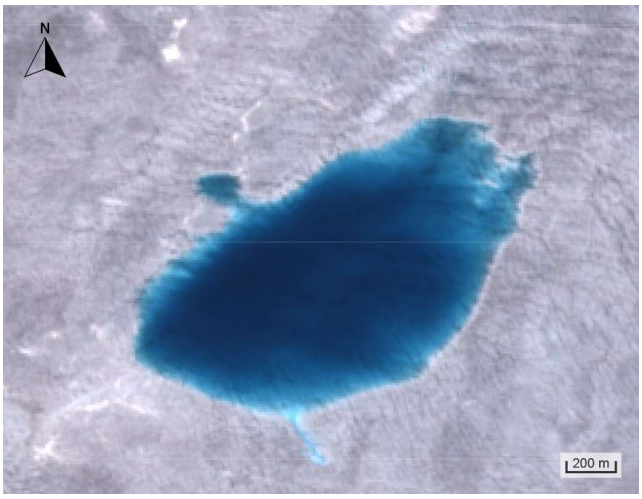

Fig. 58: Lake 'lk6', situated north of the main glacier artery and away from fast-moving ice, has a rounder and more continuous water area, facilitating easier automatic lake area detection.

Another limitation of the method used is the pre-selection of lakes for analysis, excluding other water bodies on and around the glacier. While this approach generates accurate graphs for specific lakes, it does not provide data on the total water body area or a complete overview of filling and draining patterns. Analyzing all lakes in the surrounding area could offer more comprehensive insights into the relationship between meltwater production (measured by PDD) and lake filling. Despite these limitations, the semi-automatic lake area detection method produces satisfactory results, clearly highlighting trends and successfully detecting numerous lake drainage events.

4.3 Climate change context

The findings of this thesis contribute significantly to the understanding of the SKK glacier's dynamics, particularly in the context of climate change. A noteworthy connection between the formation of crevasses and subsequent calving events is established. In a scenario of rising temperatures, it is anticipated that the glacier will flow faster, likely leading to more frequent crevasse formation (Colgan et al. 2016; Thomas et al. 2011). Deep precursor crevasses, especially those that form in areas where the ice is vertically bent by underlying bed topography, are prone to cause calving when filled with meltwater (Van Dongen et al. 2019). Consequently, an increase in deep precursor crevasses, coupled with accelerated glacier flow, intensifies calving activity. This escalation in calving contributes to greater mass loss from the glacier, ultimately contributing to rising sea levels.

Additionally, this research shows a link between the drainage of supraglacial lakes and the acceleration of ice flow. In a warming climate, the expansion of supraglacial hydrological systems inland has varying impacts on ice dynamics. At lower altitudes, enhanced surface strain rates facilitate crevasse and moulin formation, enabling water to infiltrate the ice. This leads to a pattern of accelerated ice flow in the summer, followed by a slowdown in the fall as the subglacial hydrological system becomes more efficient. In contrast, at higher altitudes, lake drainage and meltwater penetration to the glacier bed occur less efficiently, resulting in an acceleration of ice flow in both summer and winter. Understanding these mechanisms is crucial for improving predictions of glacial behavior in response to climate change (Koziol & Arnold 2018; Lampkin et al. 2013).

4.4 Further research

Better data and advanced methods

This study opens up new avenues for future research into the triggers of large calving events. Employing ultra-high-resolution satellite imagery, such as from WorldView, GeoEye, Pléiades, or SuperView satellites (Han et al. 2020; Herzfeld et al. 2022), would enable a more detailed analysis of crevasses. High spatial resolution images can provide precise data on crevasse deformation, opening rates, and potentially their depth (Enderlin & Bartholomaus 2020). Detection of newly forming cracks and surface streams would enhance the understanding of the glacier's hydrological drainage system (Yang & Smith 2013). For smaller lakes where mixed pixels are a common issue in coarse-resolution imagery, these high-resolution images could enable more accurate calculations of water areas and depths.

Supplementing satellite imagery with aerial data from Unmanned Aerial Vehicles (UAV) could provide additional analytical detail. UAV flights at low altitudes and various angles would enable the creation of 3D models of the glacier, aiding in the determination of crevasse depth—a valuable metric for identifying precursor crevasses (Colgan et al. 2016). When combined with in-situ measurements, these methods could offer a comprehensive view of crevasse structures, although this would significantly increase the complexity of the study and may limit the applicability of the methods to other glaciers.

Future research should also consider a better integration of optical imagery and Synthetic Aperture Radar (SAR) data, as demonstrated by Miles et al. (2017). Active remote sensing technologies like SAR can improve temporal resolution and enable a finer detection of changes on the glacier. SAR data could form the basis for detecting supraglacial lake drainage and calving events (Rohner et al. 2019). Additionally, employing Light Detection and Ranging (LiDAR) sensors to monitor the calving front and nearby crevasses could provide detailed insights into the influence of precursor crevasses on calving events. However, the installation of permanent LiDAR equipment such as a Terrestrial Laser Scanner (TLS) on the SKK glacier, given its size and remote location, poses logistical challenges and would require frequent maintenance due to the extreme climate. Moreover, the low-lying topography around the glacier terminus does not allow for optimal viewing angles and might thus necessitate the use of aerial vehicles for optimal LiDAR data acquisition.

Additional valuable data for this research could be obtained from sensors installed directly on or near the glacier, measuring values such as air temperature, horizontal and vertical ice displacement, or meltwater output. Precise data on the number of days with temperatures above zero degrees would refine meltwater calculations, enhancing understanding of its impact on lake filling, glacier velocity, and the efficiency of subglacial drainage systems. Measuring meltwater input to the glacier bed and discharge to the ocean would offer significant insights into the subglacial hydrological system (Bartholomew et al. 2011; Lüthje et al. 2006). Beaird et al. (2017) have shown that it is possible to infer freshwater discharge from the SKK glacier to the ocean by using hydrographic observations of geochemical tracers. Conducting such observations during a lake drainage event could yield new insights into the effects of these events on calving. Additionally, incorporating data from Global Positioning System (GPS) trackers installed on the glacier surface would significantly increase the accuracy of velocity measurements, highlighting the impact of lake drainages on ice flow (Rohner et al. 2019).

Advancements in automatic crevasse tracking and supraglacial lake monitoring could be achieved through machine learning techniques (Bhardwaj et al. 2016; Dirscherl et al. 2020). Developing a model trained to recognize precursor crevasses and track them based on their shape would substantially reduce manual workload and enable the analysis of a larger number of events. Furthermore, a more sophisticated algorithm for lake surface calculation could be developed to automatically identify outliers and detect drainage events, enhancing the study's overall efficiency and accuracy.

In addition to utilizing new data sources and advanced methods, the scope of future research could be significantly enhanced by extending the analysis over a larger timeframe, incorporating a greater number of calving and lake drainage events. A more extensive dataset would facilitate a more robust detection of potential correlations within the data. Detailed examination of cascading lake events, particularly focusing on specific lake pairs, could provide deeper insights into the exact dynamics leading to the drainage of downstream lakes. Moreover, the methodologies developed in this study hold potential for application in the

analysis of other glaciers. Expanding the study to include more sites would add diversity to the dataset, enabling the development of more generalizable conclusions about tidewater glaciers' behavior.
By employing these techniques, researchers can gain insights into the behavior of various glacial systems under changing climatic conditions, further enhancing the ability to predict and prepare for global sea level rise. This study thus not only contributes to the specific understanding of the SKK glacier but also sets a precedent for broader glaciological research in the era of climate change.

Implications

These proposed enhancements to the study of triggers for large calving events would undoubtedly increase both the complexity and the cost of the research, potentially transforming it into a multi-year project. By refining the methodologies for studying precursor crevasses and supraglacial lakes, a more accurate interpretation of the results can be achieved. Specifically, this enhanced approach would allow for the precise identification of zones where precursor crevasses form, along with a deeper understanding of the underlying causes. Furthermore, the impact of supraglacial lake drainage on the speed of glacier ice flow and the resulting calving events could be analyzed more comprehensively. An in-depth analysis with better data and more advanced methods would enable to delineation of the causal relationships with greater clarity. Consequently, the findings of the current thesis could be validated and elaborated upon with increased detail and certainty, thereby amplifying the study's significance. Moreover, adopting an interdisciplinary approach could further elevate the study's value. Integrating insights from glaciology with climatology and oceanography can provide a more holistic understanding of glacier dynamics. This comprehensive perspective is crucial for grasping the complex interactions between glaciers, climate systems, and ocean currents.
The next logical step would be to integrate the findings from such comprehensive studies into glacier models. This integration would refine predictions about calving events, which, in turn, would contribute to more accurate global predictions about sea-level rise. The accuracy of these predictions is vital for informing policymakers, global alliances, and populations, especially considering the projected widespread retreat and melting of glaciers worldwide. Accurate predictions of sea level rise are essential for preparing and adapting to the impacts of climate change. The culmination of these efforts would significantly advance our understanding of glacier dynamics in the face of climate change, providing critical insights for global environmental management and policy-making (Hock & Huss 2021).

5 Conclusion

This study on the Sermeq Kujalleq in Kangia (SKK) advances our understanding of the mechanisms behind large calving events, specifically examining the roles of crevasses and supraglacial lakes. The research shows that many calving events are preceded by visible precursor crevasses, often linked to a specific area in the southern and middle part of the glacier's terminal zone, where the bed topography suddenly changes in elevation, like a bulge. This indicates that crevasse formation, influenced by bed topography, is a key factor in calving events. However, it's also clear that not all crevasses result in calving, pointing to the importance of other contributing factors such as submarine melting, glacier flow speed, meltwater production, and the back force exerted by the ice mélange in the fjord.

The study also reveals a significant relationship between supraglacial lake drainage and glacier flow acceleration. Most lakes reach their maximum size early in the melt season, with subsequent drainage events impacting the glacier's velocity. The research shows that lower-elevation lakes drain more frequently, sometimes involving cascading drainage events. These drainages, particularly the rapid ones involving significant water area losses, correspond with increases in glacier velocity at the beginning of summer. However, as the melt season progresses and the subglacial drainage system becomes more efficient, the glacier's velocity decreases, despite ongoing meltwater production. This effect is attributed to the lower water pressure at the glacier bed, which increases the friction between the ice and the bedrock, reducing basal sliding.

Moreover, an interplay between calving events, glacier speedups, and lake drainages is probable. Some calving events coincide with periods of increased glacier velocity, suggesting a causal interaction between these factors. Glacier speedups, influenced by meltwater lubrication at the bed, which is increased during lake drainage events, might trigger calving events. However, due to the complexity of the glacier dynamics and the low temporal resolution of available data, the precise nature of this interaction remains uncertain.

To enhance the current understanding and enable more precise conclusions, future research would benefit from data with a higher spatial resolution, especially for tracking crevasse depth and deformation, as well as for more accurate monitoring of lakes on the rapidly flowing, heavily crevassed glacier ice. Extending the analysis period and employing fully automatic methods would enable the detection of a larger number of calving and drainage events, thereby enhancing the ability to uncover significant correlations and gain more comprehensive insights. Incorporating these findings into future calving models would benefit broader models predicting glacier mass loss. Such comprehensive research contributes significantly to a holistic understanding of calving and glacier dynamics, particularly crucial in the context of climate change and its implications for glacial stability and sea-level rise.

6 References

Amundson, J. M., Fahnestock, M., Truffer, M., Brown, J., Lüthi, M. P., & Motyka, R. J. (2010): Ice mélange dynamics and implications for terminus stability, Jakobshavn Isbrse, Greenland. *Journal of Geophysical Research: Earth Surface*, vol. *115*(1). https://doi.org/10.1029/2009JF001405

An, L., Rignot, E., Elieff, S., Morlighem, M., Millan, R., Mouginot, J., Holland, D. M., Holland, D., & Paden, J. (2017): Bed elevation of Jakobshavn Isbræ, West Greenland, from high-resolution airborne gravity and other data. *Geophysical Research Letters*, vol. *44*(8), pp. 3728–3736. https://doi.org/10.1002/2017GL073245

Andrews, L. C., Catania, G. A., Hoffman, M. J., Gulley, J. D., Lüthi, M. P., Ryser, C., Hawley, R. L., & Neumann, T. A. (2015): Direct observations of evolving subglacial drainage beneath the Greenland Ice Sheet. *Nature*, vol. *514*(7520), pp. 80–83. https://doi.org/10.1038/nature13796

Bartholomew, I., Nienow, P., Sole, A., Mair, D., Cowton, T., Palmer, S., & Wadham, J. (2011): Supraglacial forcing of subglacial drainage in the ablation zone of the Greenland ice sheet. *Geophysical Research Letters*, vol. *38*(8). https://doi.org/10.1029/2011GL047063

Beaird, N., Straneo, F., & Jenkins, W. (2017): Characteristics of meltwater export from Jakobshavn Isbræ and Ilulissat Icefjord. *Annals of Glaciology*, vol. *58*(74), pp. 107–117. https://doi.org/10.1017/aog.2017.19

Benn, D. I., Cowton, T., Todd, J., & Luckman, A. (2017): Glacier Calving in Greenland. In *Current Climate Change Reports* (Vol. 3, Issue 4, pp. 282–290). Springer. https://doi.org/10.1007/s40641-017-0070-1

Benn, D. I., Warren, C. R., & Mottram, R. H. (2007): Calving processes and the dynamics of calving glaciers. *Earth-Science Reviews*, vol. *82*(3–4), pp. 143–179. https://doi.org/10.1016/j.earscirev.2007.02.002

Berg, B., & Bassis, J. (2022): Crevasse advection increases glacier calving. *Journal of Glaciology*, vol. *68*(271), pp. 977–986. https://doi.org/10.1017/jog.2022.10

Bhardwaj, A., Sam, L., Singh, S., & Kumar, R. (2016): Automated detection and temporal monitoring of crevasses using remote sensing and their implications for glacier dynamics. *Annals of Glaciology*, vol. *57*(71), pp. 81–91. https://doi.org/10.3189/2016AoG71A496

Cassotto, R., Fahnestock, M., Amundson, J. M., Truffer, M., Boettcher, M. S., De La Peña, S., & Howat, I. (2019): Non-linear glacier response to calving events, Jakobshavn Isbræ, Greenland. *Journal of Glaciology*, vol. *65*(249), pp. 39–54. https://doi.org/10.1017/jog.2018.90

Chandler, D. M., Wadham, J. L., Nienow, P. W., Doyle, S. H., Tedstone, A. J., Telling, J., Hawkings, J., Alcock, J. D., Linhoff, B., & Hubbard, A. (2021): Rapid development and persistence of efficient subglacial drainage under 900 m-thick ice in Greenland. *Earth and Planetary Science Letters*, vol. *566*. https://doi.org/10.1016/j.epsl.2021.116982

Chudley, T. R., Christoffersen, P., Doyle, S. H., Dowling, T. P. F., Law, R., Schoonman, C. M., Bougamont, M., & Hubbard, B. (2021): Controls on Water Storage and Drainage in Crevasses on the Greenland Ice Sheet. *Journal of Geophysical Research: Earth Surface*, vol. *126*(9). https://doi.org/10.1029/2021JF006287

Cochran, J. R., & Bell, R. E. (2010): *IceBridge Sander AIRGrav L1B Geolocated Free Air Gravity Anomalies, Version 1*.

Colgan, W., Rajaram, H., Abdalati, W., McCutchan, C., Mottram, R., Moussavi, M. S., & Grigsby, S. (2016): Glacier crevasses: Observations, models, and mass balance implications. In *Reviews of Geophysics* (Vol. 54, Issue 1, pp. 119–161). Blackwell Publishing Ltd. https://doi.org/10.1002/2015RG000504

Condeça, J., Nascimento, J., & Barreiras, N. (2022): Monitoring the Storage Volume of Water Reservoirs Using Google Earth Engine. *Water Resources Research*, vol. *58*(3). https://doi.org/10.1029/2021WR030026

Dirscherl, M., Dietz, A. J., Kneisel, C., & Kuenzer, C. (2020): Automated mapping of antarctic supraglacial lakes using a machine learning approach. *Remote Sensing*, vol. *12*(7). https://doi.org/10.3390/rs12071203

Doyle, S. H., Hubbard, B., Christoffersen, P., Young, T. J., Hofstede, C., Bougamont, M., Box, J. E., & Hubbard, A. (2018): Physical Conditions of Fast Glacier Flow: 1. Measurements From Boreholes Drilled to the Bed of Store Glacier, West Greenland. *Journal of Geophysical Research: Earth Surface*, vol. *123*(2), pp. 324–348. https://doi.org/10.1002/2017JF004529

Drost Jensen, C. (2023): *DMI Report 23-08: Weather Observations from Greenland 1958-2022*.

Enderlin, E. M., & Bartholomaus, T. C. (2020): Sharp contrasts in observed and modeled crevasse patterns at Greenland's marine terminating glaciers. *Cryosphere*, vol. *14*(11), pp. 4121–4133. https://doi.org/10.5194/tc-14-4121-2020

ESA. (2015): *Sentinel-2 User Handbook*. https://sentinel.esa.int/documents/247904/685211/Sentinel-2_User_Handbook

European Space Agency (ESA). (2023): *Sentinel-1 SAR User Guide*. Sentinel Online. https://sentinels.copernicus.eu/web/sentinel/user-guides/sentinel-1-sar

Gorelick, N., Hancher, M., Dixon, M., Ilyushchenko, S., Thau, D., & Moore, R. (2017): Google Earth Engine: Planetary-scale geospatial analysis for everyone. *Remote Sensing of Environment*. https://doi.org/10.1016/j.rse.2017.06.031

Han, Y., Wang, S., Gong, D., Wang, Y., Wang, Y., & Ma, X. (2020): State of the Art in Digital Surface Modelling from Multi-View High-Resolution Satellite Images. *ISPRS Annals of the Photogrammetry, Remote Sensing and Spatial Information Sciences*, vol. *5*(2), pp. 351–356. https://doi.org/10.5194/isprs-annals-V-2-2020-351-2020

Herzfeld, U., Lawson, M., Hayes, A., Hessburg, L., & Trantow, T. (2022): *ICESat-2, SkySat, WorldView and Sentinel: Automated Extraction of High-Resolution Spatial Information for Investigation of Surging and Fast-Moving Glaciers*. https://doi.org/10.1002/essoar.10504882.1

Hock, R., & Huss, M. (2021): Chapter 9 - Glaciers and climate change. In T. M. Letcher (Ed.), *Climate Change (Third Edition)* (Third Edition, pp. 157–176). Elsevier. https://doi.org/https://doi.org/10.1016/B978-0-12-821575-3.00009-8

Hoffman, M. J., Perego, M., Andrews, L. C., Price, S. F., Neumann, T. A., Johnson, J. V., Catania, G., & Lüthi, M. P. (2018): Widespread Moulin Formation During Supraglacial Lake Drainages in Greenland. *Geophysical Research Letters*, vol. *45*(2), pp. 778–788. https://doi.org/10.1002/2017GL075659

Hogg, A., Shepherd, A., & Gourmelen, N. (2015): A first look at the performance of Sentinel-1 over the West Antarctic Ice Sheet. In *Fringe 2015*.

Jiang, D., Li, X., Zhang, K., Marinsek, S., Hong, W., & Wu, Y. (2022): Automatic Supraglacial Lake Extraction in Greenland Using Sentinel-1 SAR Images and Attention-Based U-Net. *Remote Sensing*, vol. *14*(19). https://doi.org/10.3390/rs14194998

Joseph, C. A., & Lampkin, D. J. (2017): Spatial and temporal variability of water-filled crevasse hydrologic states along the shear margins of Jakobshavn Isbrae, Greenland. *The Cryosphere Discussions*. https://doi.org/10.5194/tc-2017-86

Joughin, I., Howat, I., Smith, B., & Scambos, T. (2021): *MEaSUREs Greenland Ice Velocity: Selected Glacier Site Velocity Maps from InSAR, Version 4. W69.10N*.

Joughin, I., Smith, B. E., Howat, I. M., Scambos, T., & Moon, T. (2010): Greenland flow variability from ice-sheet-wide velocity mapping. *Journal of Glaciology*, vol. *56*(197), pp. 415–430. https://doi.org/10.3189/002214310792447734

Koziol, C. P., & Arnold, N. (2018): Modelling seasonal meltwater forcing of the velocity of land-terminating margins of the Greenland Ice Sheet. *Cryosphere*, vol. *12*(3), pp. 971–991. https://doi.org/10.5194/tc-12-971-2018

Kulessa, B., Hubbard, A. L., Booth, A. D., Bougamont, † Marion, Dow, C. F., Samuel, †, Doyle, H., Christoffersen, P., Lindbäck, K., Pettersson, R., Fitzpatrick, A. A. W., & Jones, G. A. (2017): Seismic evidence for complex sedimentary control of Greenland Ice Sheet flow. *Science Advances*, vol. *3*. https://www.science.org

Lampkin, D. J., Amador, N., Parizek, B. R., Farness, K., & Jezek, K. (2013): Drainage from water-filled crevasses along the margins of Jakobshavn Isbræ: A potential catalyst for catchment expansion. *Journal of Geophysical Research: Earth Surface*, vol. *118*(2), pp. 795–813. https://doi.org/10.1002/jgrf.20039

Lampkin, D. J., Koenig, L., Joseph, C., & Box, J. E. (2020): Investigating Controls on the Formation and Distribution of Wintertime Storage of Water in Supraglacial Lakes. *Frontiers in Earth Science*, vol. *8*. https://doi.org/10.3389/feart.2020.00370

Lampkin, D. J., Parizek, B., Larour, E. Y., Seroussi, H., Joseph, C., & Cavanagh, J. P. (2018): Toward improved understanding of changes in Greenland outlet glacier shear margin dynamics in a warming climate. *Frontiers in Earth Science*, vol. *6*. https://doi.org/10.3389/feart.2018.00156

Lemos, A., Shepherd, A., McMillan, M., Hogg, A. E., Hatton, E., & Joughin, I. (2018): Ice velocity of Jakobshavn Isbræ, Petermann Glacier, Nioghalvfjerdsfjorden, and Zachariæ Isstrøm, 2015-2017, from Sentinel 1-a/b SAR imagery. In *Cryosphere* (Vol. 12, Issue 6, pp. 2087–2097). Copernicus GmbH. https://doi.org/10.5194/tc-12-2087-2018

Liang, Y. L., Colgan, W., Lv, Q., Steffen, K., Abdalati, W., Stroeve, J., Gallaher, D., & Bayou, N. (2012): A decadal investigation of supraglacial lakes in West Greenland using a fully automatic detection and tracking algorithm. *Remote Sensing of Environment*, vol. *123*, pp. 127–138. https://doi.org/10.1016/j.rse.2012.03.020

Lüthi, M. P., Ryser, C., Andrews, L. C., Catania, G. A., Funk, M., Hawley, R. L., Hoffman, M. J., & Neumann, T. A. (2015): Heat sources within the Greenland Ice Sheet: Dissipation, temperate paleo-firn and cryo-hydrologic warming. *Cryosphere*, vol. *9*(1), pp. 245–253. https://doi.org/10.5194/tc-9-245-2015

Lüthje, M., Pedersen, L. T., Reeh, N., & Greuell, W. (2006): Modelling the evolution of supraglacial lakes on the west Greenland ice-sheet margin. *Journal of Glaciology*, vol. *52*(179), pp. 608–618. https://doi.org/10.3189/172756506781828386

MacGregor, J., & Harbeck, J. (2023): *NASA Operation IceBridge*. https://icebridge.gsfc.nasa.gov/

MacKie, E. J., Schroeder, D. M., Zuo, C., Yin, Z., & Caers, J. (2021): Stochastic modeling of subglacial topography exposes uncertainty in water routing at Jakobshavn Glacier. *Journal of Glaciology*, vol. *67*(261), pp. 75–83. https://doi.org/10.1017/jog.2020.84

Mayer, H., & Herzfeld, U. C. (2000): Structural glaciology of the fast-moving Jakobshavn Isbrae, Greenland, compared to the surging Bering Glacier, Alaska, U.S.A. *Annals of Glaciology*, vol. *30*, pp. 243–249. https://doi.org/10.3189/172756400781820543

McFeeters, S. K. (1996): The use of the Normalized Difference Water Index (NDWI) in the delineation of open water features. *International Journal of Remote Sensing*, vol. *17*(7), pp. 1425–1432. https://doi.org/10.1080/01431169608948714

Meier, M. F. (2024): *Glacier*. Britannica Academic. https://academic.eb.com/levels/collegiate/article/glacier/108438#65697.toc

Mercenier, R., Lüthi, M. P., & Vieli, A. (2020): How Oceanic Melt Controls Tidewater Glacier Evolution. *Geophysical Research Letters*, vol. *47*(8). https://doi.org/10.1029/2019GL086769

Miles, K. E., Willis, I. C., Benedek, C. L., Williamson, A. G., & Tedesco, M. (2017): Toward monitoring surface and subsurface lakes on the Greenland ice sheet using sentinel-1 SAR and landsat-8 OLI imagery. *Frontiers in Earth Science*, vol. *5*. https://doi.org/10.3389/feart.2017.00058

Moon, T., Joughin, I., Smith, B., & Howat, I. (2012): 21st-Century Evolution of Greenland Outlet Glacier Velocities. *Science*, vol. *336*(6081), pp. 576–578. https://doi.org/10.1126/science.1219985

Morlighem, M., Williams, C. N., Rignot, E., An, L., Arndt, J. E., Bamber, J. L., Catania, G., Chauché, N., Dowdeswell, J. A., Dorschel, B., Fenty, I., Hogan, K., Howat, I., Hubbard, A., Jakobsson, M., Jordan, T. M., Kjeldsen, K. K., Millan, R., Mayer, L., … Zinglersen, K. B. (2017): BedMachine v3: Complete Bed Topography and Ocean Bathymetry Mapping of Greenland From Multibeam Echo Sounding Combined With Mass Conservation. *Geophysical Research Letters*, vol. *44*(21), pp. 11,051-11,061. https://doi.org/10.1002/2017GL074954

Morriss, B. F., Hawley, R. L., Chipman, J. W., Andrews, L. C., Catania, G. A., Hoffman, M. J., Lüthi, M. P., & Neumann, T. A. (2013): A ten-year record of supraglacial lake evolution and rapid drainage in West Greenland using an automated processing algorithm for multispectral imagery. *Cryosphere*, vol. *7*(6), pp. 1869–1877. https://doi.org/10.5194/tc-7-1869-2013

Motyka, R. J., Truffer, M., Fahnestock, M., Mortensen, J., Rysgaard, S., & Howat, I. (2011): Submarine melting of the 1985 Jakobshavn Isbræ floating tongue and the triggering of the current retreat. *Journal of Geophysical Research: Earth Surface*, vol. *116*(1). https://doi.org/10.1029/2009JF001632

Moussavi, M. S., Abdalati, W., Pope, A., Scambos, T., Tedesco, M., MacFerrin, M., & Grigsby, S. (2016): Derivation and validation of supraglacial lake volumes on the Greenland Ice Sheet from high-resolution satellite imagery. *Remote Sensing of Environment*, vol. *183*, pp. 294–303. https://doi.org/10.1016/j.rse.2016.05.024

NASA/METI/AIST/Japan Spacesystems, & U.S./Japan ASTER Science Team. (2019): ASTER Global Digital Elevation Model V003. *NASA EOSDIS Land Processes Distributed Active Archive Center*.

Nick, F. M., Vieli, A., Howat, I. M., & Joughin, I. (2009): Large-scale changes in Greenland outlet glacier dynamics triggered at the terminus. *Nature Geoscience*, vol. *2*(2), pp. 110–114. https://doi.org/10.1038/ngeo394

Poinar, K., & Andrews, L. C. (2020): Challenges in predicting Greenland supraglacial lake drainages at the regional scale. *The Cryosphere Discussions*. https://doi.org/10.5194/tc-2020-251

Porter, C., Morin, P., Howat, I., Noh, M.-J., Bates, B., Peterman, K., Keesey, S., Schlenk, M., Gardiner, J., Tomko, K., Willis, M., Kelleher, C., Cloutier, M., Husby, E., Foga, S., Nakamura, H., Platson, M., Wethington, M. Jr., Williamson, C., … Bojesen, M. (2018): ArcticDEM Mosaic. In *DEM(s) created by the Polar Geospatial Center from DigitalGlobe, Inc. imagery* (Vol. 1). Harvard Dataverse.

Raikar, S. Pai. (2023): Greenland Ice Sheet. In *Encyclopedia Britannica*. https://www.britannica.com/place/Greenland-Ice-Sheet

Rignot, E., Velicogna, I., Van Den Broeke, M. R., Monaghan, A., & Lenaerts, J. (2011): Acceleration of the contribution of the Greenland and Antarctic ice sheets to sea level rise. *Geophysical Research Letters*, vol. *38*(5). https://doi.org/10.1029/2011GL046583

Rohner, C., Small, D., Henke, D., Lüthi, M. P., & Vieli, A. (2019): Multisensor validation of tidewater glacier flow fields derived from synthetic aperture radar (SAR) intensity tracking. *Cryosphere*, vol. *13*(11), pp. 2953–2975. https://doi.org/10.5194/tc-13-2953-2019

Rückamp, M., Neckel, N., Berger, S., Humbert, A., & Helm, V. (2019): Calving Induced Speedup of Petermann Glacier. *Journal of Geophysical Research: Earth Surface*, vol. *124*(1), pp. 216–228. https://doi.org/10.1029/2018JF004775

Shepherd, A., Ivins, E. R., A, G., Barletta, V. R., Bentley, M. J., Bettadpur, S., Briggs, K. H., Bromwich, D. H., Forsberg, R., Galin, N., Horwath, M., Jacobs, S., Joughin, I., King, M. A., Lenaerts, J. T. M., Li, J., Ligtenberg, S. R. M., Luckman, A., Luthcke, S. B., … Zwally, H. J. (2012): A Reconciled Estimate of Ice-Sheet Mass Balance. *Science*, vol. *338*(6111), pp. 1183–1189. https://doi.org/10.1126/science.1228102

Singh, D. K., Thakur, P. K., Naithani, B. P., & Kaushik, S. (2021): Quantifying the sensitivity of band ratio methods for clean glacier ice mapping. *Spatial Information Research*, vol. *29*(3), pp. 281–295. https://doi.org/10.1007/s41324-020-00352-8

Steiger, N., Nisancioglu, K. H., Åkesson, H., De Fleurian, B., & Nick, F. M. (2018): Simulated retreat of Jakobshavn Isbræ since the Little Ice Age controlled by geometry. *Cryosphere*, vol. *12*(7), pp. 2249–2266. https://doi.org/10.5194/tc-12-2249-2018

Stevens, L. A., Behn, M. D., McGuire, J. J., Das, S. B., Joughin, I., Herring, T., Shean, D. E., & King, M. A. (2015): Greenland supraglacial lake drainages triggered by hydrologically induced basal slip. *Nature*, vol. *522*(7554), pp. 73–76. https://doi.org/10.1038/nature14480

Stevens, L. A., Nettles, M., Davis, J. L., Creyts, T. T., Kingslake, J., Hewitt, I. J., & Stubblefield, A. (2022): Tidewater-glacier response to supraglacial lake drainage. *Nature Communications*, vol. *13*(1). https://doi.org/10.1038/s41467-022-33763-2

Straneo, F., & Heimbach, P. (2013): North Atlantic warming and the retreat of Greenland's outlet glaciers. In *Nature* (Vol. 504, Issue 7478, pp. 36–43). https://doi.org/10.1038/nature12854

Studinger, M., Manizade, S. S., Linkswiler, M. A., & Yungel, J. K. (2022): High-resolution imaging of supraglacial hydrological features on the Greenland Ice Sheet with NASA's Airborne Topographic Mapper (ATM) instrument suite. *Cryosphere*, vol. *16*(9), pp. 3649–3668. https://doi.org/10.5194/tc-16-3649-2022

Tedesco, M., Lthje, M., Steffen, K., Steiner, N., Fettweis, X., Willis, I., Bayou, N., & Banwell, A. (2012): Measurement and modeling of ablation of the bottom of supraglacial lakes in western Greenland. *Geophysical Research Letters*, vol. *39*(2). https://doi.org/10.1029/2011GL049882

Thomas, R., Frederick, E., Li, J., Krabill, W., Manizade, S., Paden, J., Sonntag, J., Swift, R., & Yungel, J. (2011): Accelerating ice loss from the fastest Greenland and Antarctic glaciers. *Geophysical Research Letters*, vol. *38*(10). https://doi.org/10.1029/2011GL047304

Trevers, M., Payne, A. J., Cornford, S. L., & Moon, T. (2019): Buoyant forces promote tidewater glacier iceberg calving through large basal stress concentrations. *Cryosphere*, vol. *13*(7), pp. 1877–1887. https://doi.org/10.5194/tc-13-1877-2019

Van Dongen, E., Jouvet, G., Walter, A., Todd, J., Zwinger, T., Asaji, I., Sugiyama, S., Walter, F., & Funk, M. (2019): Tides modulate crevasse opening prior to a major calving event at Bowdoin Glacier, Northwest Greenland. *Journal of Glaciology*, vol. *66*(255), pp. 113–123. https://doi.org/10.1017/jog.2019.89

Vandecrux, B., Box, J. E., Ahlstrøm, A. P., Andersen, S. B., Bayou, N., Colgan, W. T., Cullen, N. J., Fausto, R. S., Haas-Artho, D., Heilig, A., Houtz, D. A., How, P., Iosifescu Enescu, I., Karlsson, N. B., Kurup Buchholz, R., Mankoff, K. D., McGrath, D., Molotch, N. P., Perren, B., … Steffen, K. (2023): The historical Greenland Climate Network (GC-Net) curated and augmented Level 1 dataset. *Earth System Science Data Discussions*, vol. *2023*, pp. 1–35. https://doi.org/10.5194/essd-2023-147

Weidick, A., & Bennike, O. (2007): Quaternary glaciation history and glaciology of Jakobshavn Isbræ and the Disko Bugt region, West Greenland: A review. In *Geological Survey of Denmark and Greenland Bulletin* (Issue 14, pp. 1–78). GEUS - Geological Survey of Denmark and Greenland. https://doi.org/10.34194/geusb.v14.4985

Williamson, A. G., Banwell, A. F., Willis, I. C., & Arnold, N. S. (2018): Dual-satellite (Sentinel-2 and Landsat 8) remote sensing of supraglacial lakes in Greenland. *Cryosphere*, vol. *12*(9), pp. 3045–3065. https://doi.org/10.5194/tc-12-3045-2018

Yang, K., & Smith, L. C. (2013): Supraglacial streams on the greenland ice sheet delineated from combined spectral-shape information in high-resolution satellite imagery. *IEEE Geoscience and Remote Sensing Letters*, vol. *10*(4), pp. 801–805. https://doi.org/10.1109/LGRS.2012.2224316

Zarrinderakht, M., Schoof, C., & Peirce, A. (2022): The effect of hydrology and crevasse wall contact on calving. *Cryosphere*, vol. *16*(10), pp. 4491–4512. https://doi.org/10.5194/tc-16-4491-2022

Appendix

I Calving events and precursor crevasses

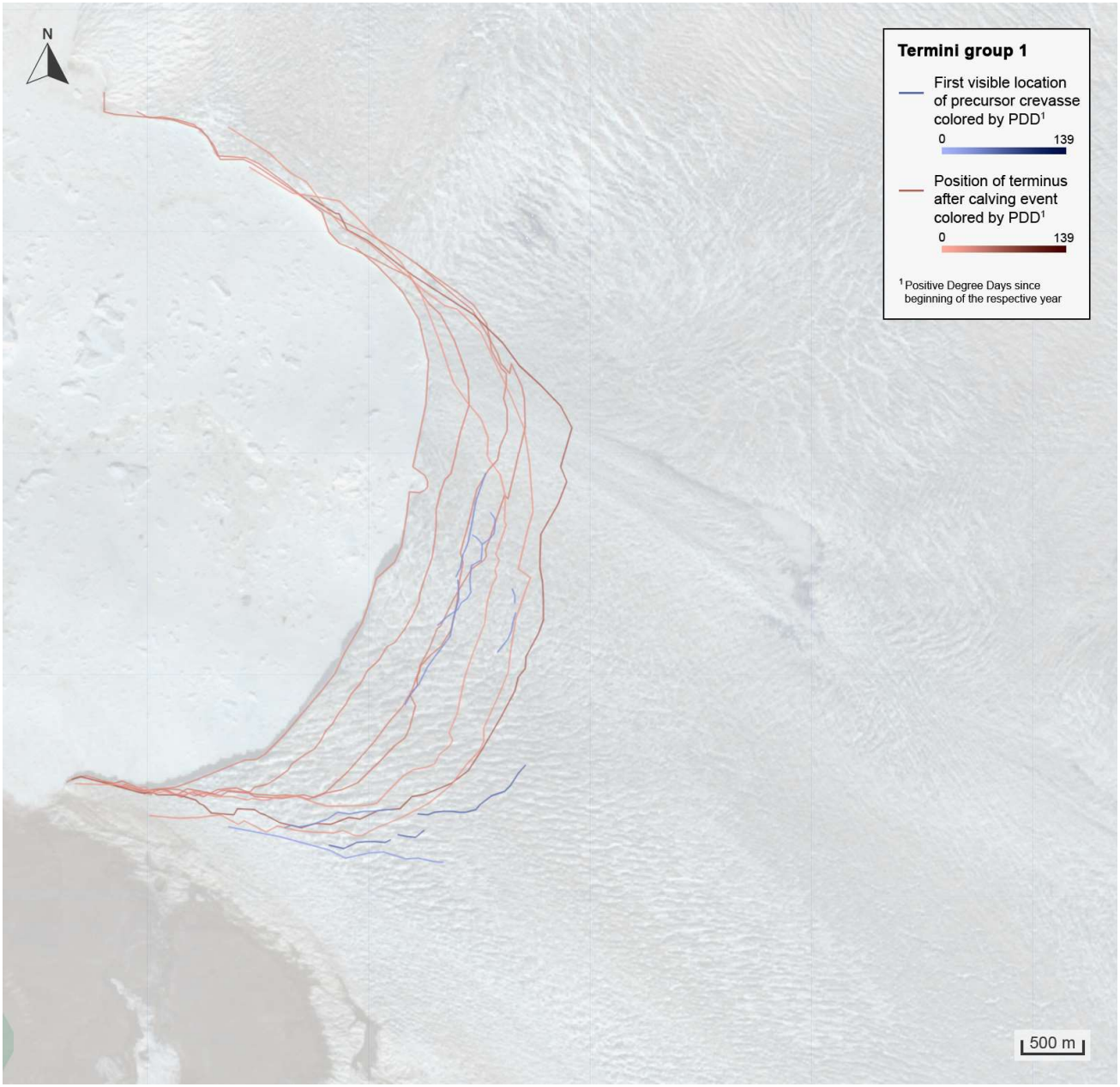

Fig. 59: Calving events situated between distances of 699 m and 2061 m from the zero point. The lines in red tones delineate the calving fronts, while the lines in blue tones represent the associated main precursor crevasses at their first appearance on optical imagery. Both are color-graded by Positive Degree Days (PDD) since January 1st. In the background is a Sentinel-2 RGB image with 20% opacity, recorded on May 25th, 2019.

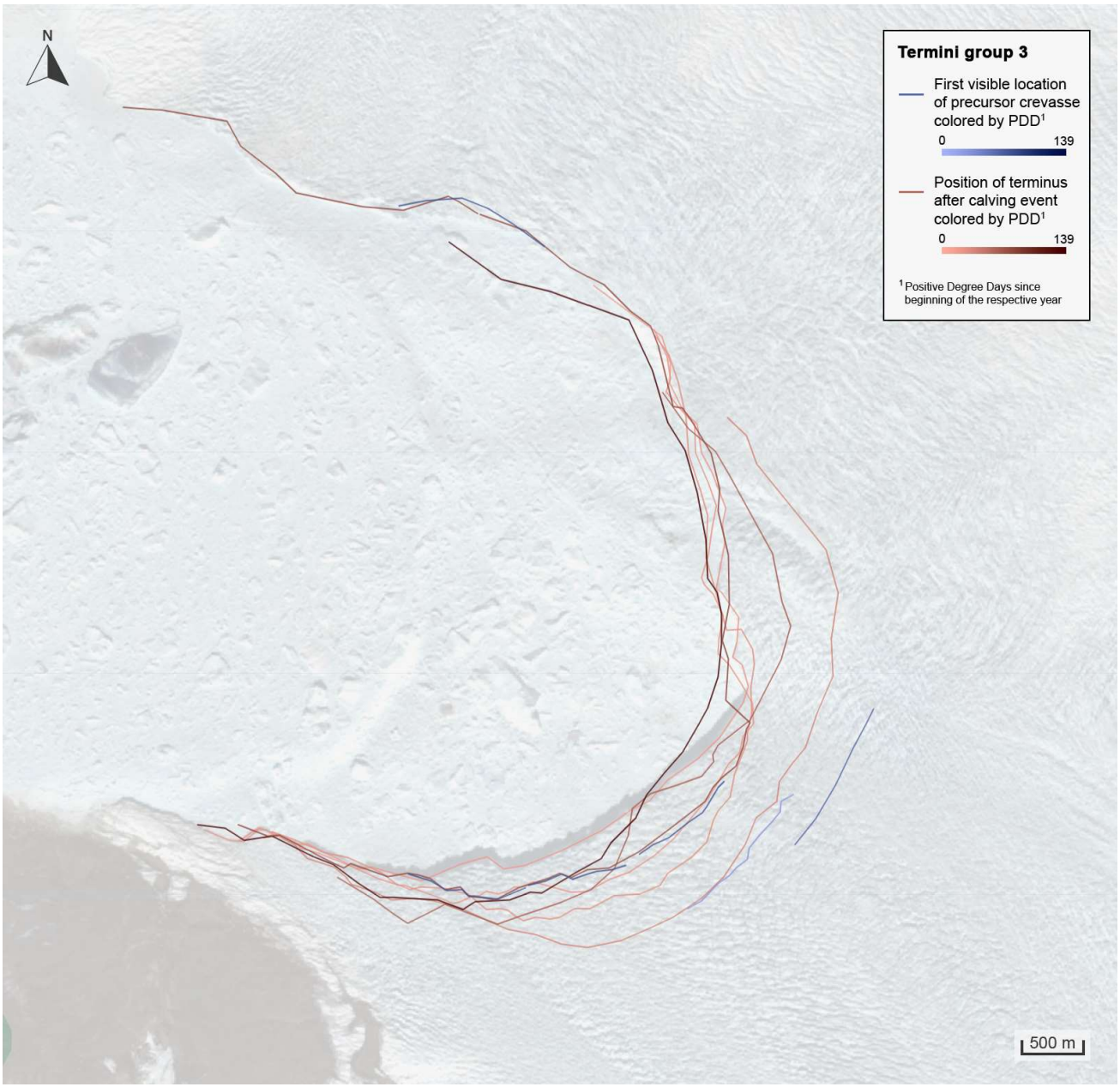

Fig. 60: Calving events situated between distances of 3405 m and 3950 m from the zero point. The lines in red tones delineate the calving fronts, while the lines in blue tones represent the associated main precursor crevasses at their first appearance on optical imagery. Both are color-graded by Positive Degree Days (PDD) since January 1st. In the background is a Sentinel-2 RGB image with 20% opacity, recorded on May 14th, 2021.

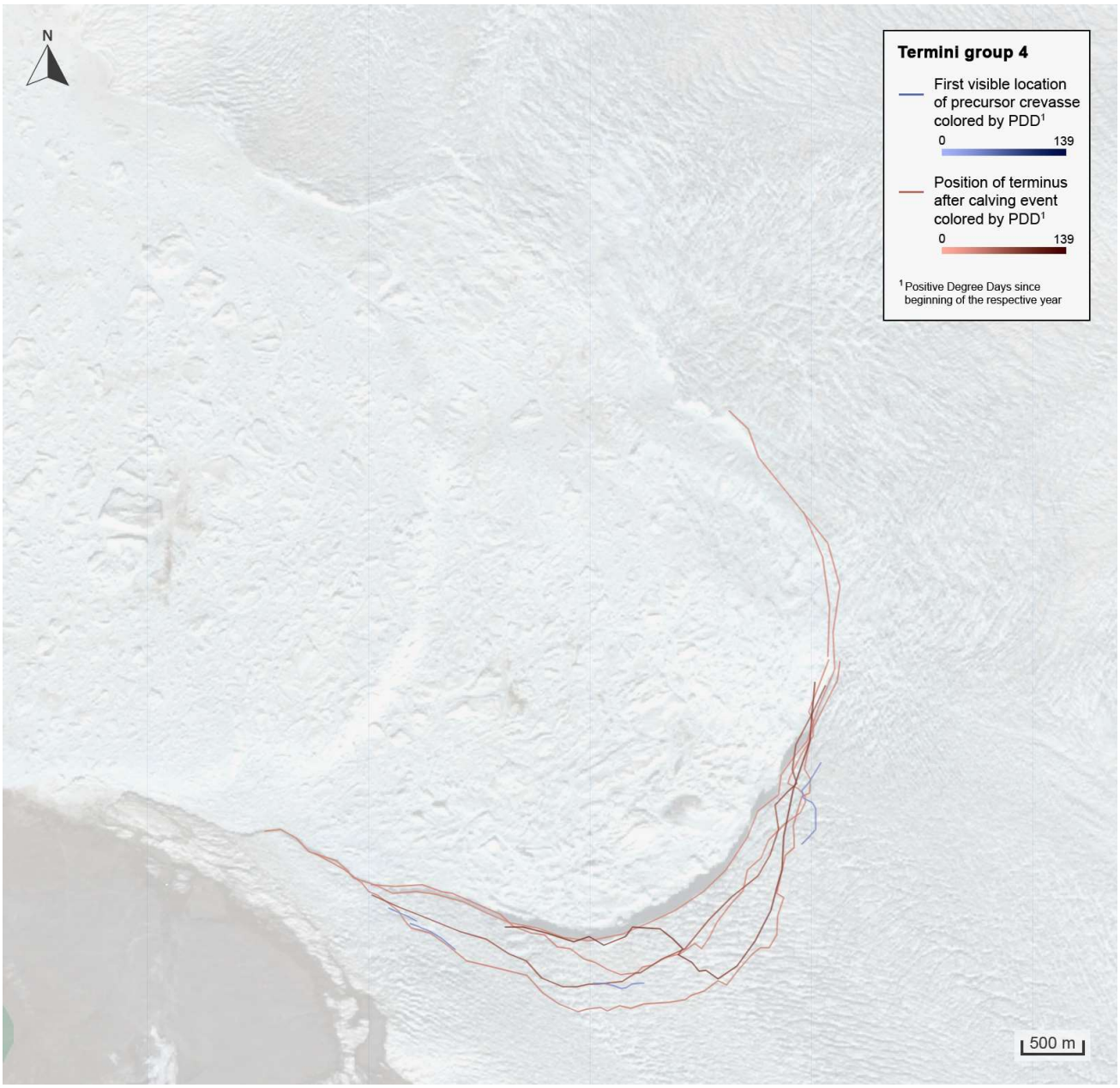

Fig. 61: Calving events situated between distances of 4260 m and 4609 m from the zero point. The lines in red tones delineate the calving fronts, while the lines in blue tones represent the associated main precursor crevasses at their first appearance on optical imagery. Both are color-graded by Positive Degree Days (PDD) since January 1st. In the background is a Sentinel-2 RGB image with 20% opacity, recorded on June 2nd, 2021.

II Lake areas 2016-2022

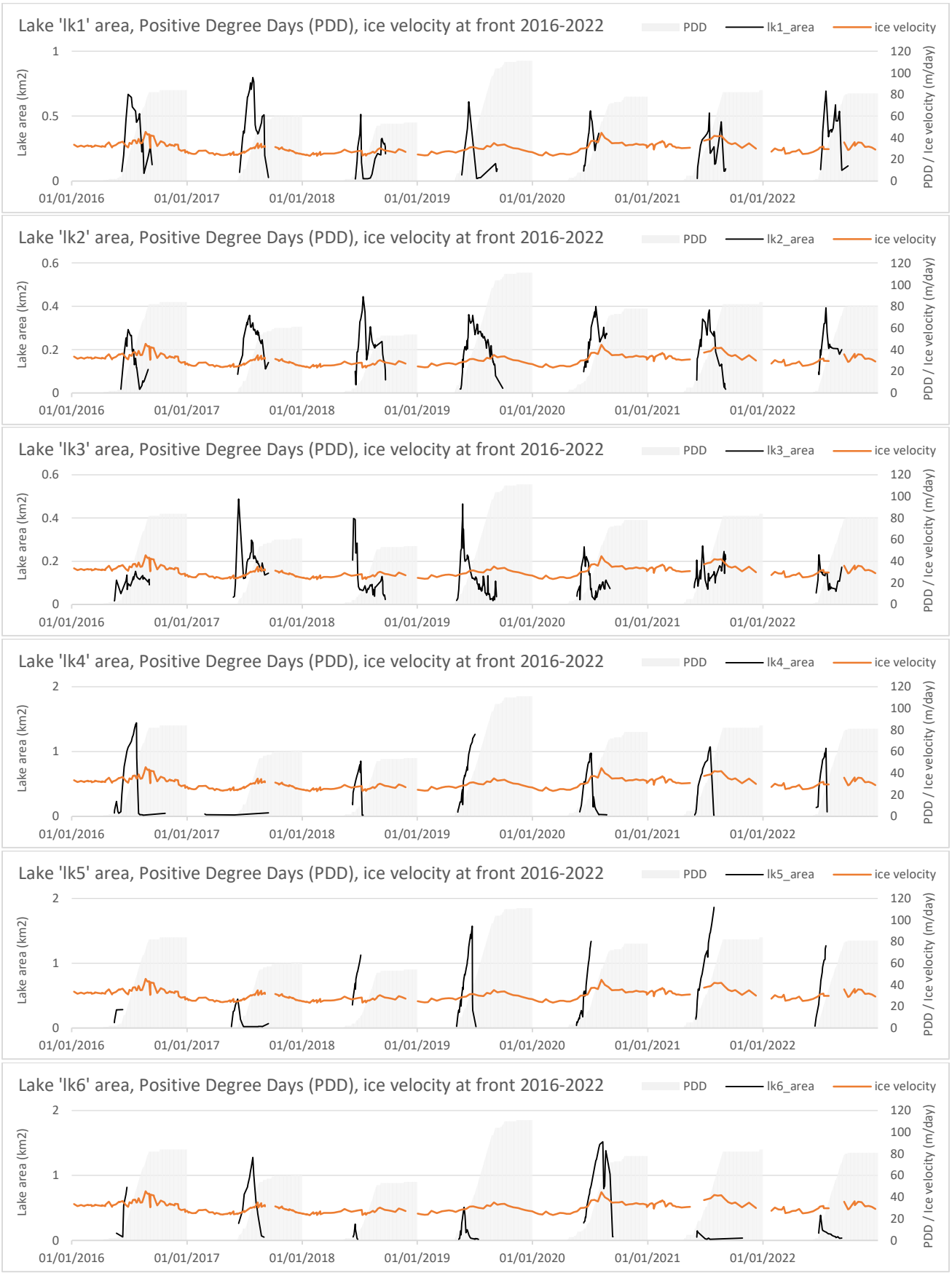

Fig. 62: Detected lake areas for supraglacial lakes 'lk1' to 'lk6' (black lines), Positive Degree Days (PDD) at Ilulissat airport (Drost Jensen 2023), and ice velocity at the calving front from 2016 to 2022 by MEaSUREs (Joughin et al. 2021).

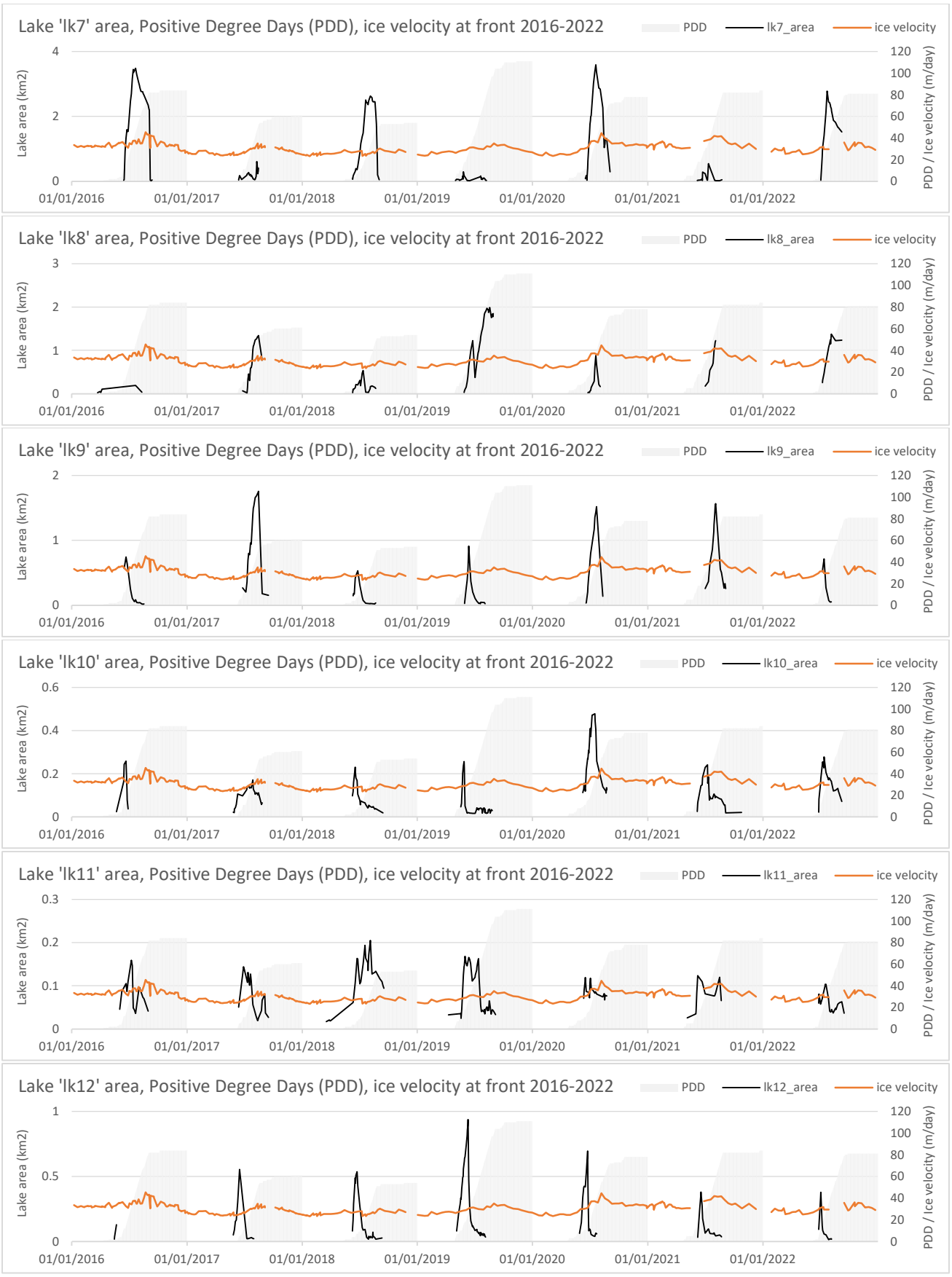

Fig. 63: Detected lake areas for supraglacial lakes 'lk7' to 'lk12' (black lines), Positive Degree Days (PDD) at Ilulissat airport (Drost Jensen 2023), and ice velocity at the calving front from 2016 to 2022 by MEaSUREs (Joughin et al. 2021).

Data Repository

The main results of this study as well as the source code used to calculate the results in Google Earth Engine (GEE) can be found in the repository under the following link: https://github.com/dorius23/ma_skk.

Declaration of Authenticity

Zurich, 30.01.2024

Personal declaration: I hereby declare that the submitted Thesis is the result of my own, independent work. All external sources are explicitly acknowledged in the Thesis.

Doriano Hautle